Ein kolloidchemischer Ansatz zur Darstellung nanostrukturierter Thermoelektrika mit verbesserter Gütezahl

(A colloidal chemistry approach to nanostructured thermoelectric materials with enhanced figure of merit)

Dissertation

Zur Erlangung des Doktorgrades der Naturwissenschaften an der
Fakultät für Mathematik, Informatik und Naturwissenschaften der
Universität Hamburg

vorgelegt von
Marcus Scheele
aus Duisburg

Hamburg
Januar 2011

1. Gutachter: Prof. Dr. Horst Weller
2. Gutachter: Prof. Dr. Alf Mews

Disputation: 25. März 2011

Preface

The experimental work in this dissertation has been carried out between May 2008 and December 2010 in the Institute of Physical Chemistry at the University of Hamburg in the group of Prof. Dr. Horst Weller. The majority of the physical measurements have been performed at the Max Planck Institute of Chemical Physics of Solids in Dresden in the group of Dr. Niels Oeschler.

The theory section contains excerpts from (1) Mark Lundstrom, *Fundamentals of Carrier Transport*, 2nd Ed., Cambridge University Press **2009;** (2) Robert J. Hunter, *Foundations of Colloid Science*, 2nd Ed., Oxford University Press **2009;** and (3) D. Fennell Evans and Håkan Wennerström, *The colloidal domain*, 2nd Ed., WILEY-VCH **1999**.

Funding has been provided by a PhD grant of the *Studienstiftung des Deutschen Volkes*.

The work is structured in 5 chapters:

In **Chapter A**, an introduction to the subject is given as well as a derivation of suitable models to describe the physical processes treated by this dissertation. At the end of **chapter A**, short summaries of the results of the three publications and the manuscript are given.

Chapter B is a copy of a manuscript by M. Scheele, N. Oeschler, K. Meier, A. Kornowski, C. Klinke and H. Weller titled "**Synthesis and Thermoelectric Characterization of Bi_2Te_3 nanoparticles**" published in *Advanced Functional Materials* **2009**, 19, 3476-3483.

Chapter C is a copy of a manuscript by M. Scheele, N. Oeschler, K. Meier, A. Kornowski, C. Klinke and H. Weller titled "**Colloidal nanostructures as building blocks for macroscopic thermoelectric materials with electron-crystal phonon-glass properties**" published in *Thermoelectric Materials - Growth, Properties, Novel Characterization Methods, and Applications*; Tuller, H. L., Baniecki, J. D., Snyder, G. J., Malen, J. A., Eds.; Mater. Res. Soc. Symp. Proc. 1267, Warrendale, PA, **2010**, DD-08-12.

Chapter D is a copy of a manuscript by M. Scheele, N. Oeschler, I. Veremchuk, K.-G. Reinsberg, A.-M. Kreuziger, A. Kornowski, J. A. Broekaert, C. Klinke and H. Weller titled "**ZT enhancement in solution-grown $Sb_{(2-x)}Bi_xTe_3$ nanoplatelets**" published in *ACS Nano* **2010**, 4, 4283-4291.

Chapter E describes an experimental approach to test the concept of energy filtering and its effect on the thermopower by lead chalcogenide core-shell nanostructures.

Where the results of each chapter are summarized in **chapter A**, a detailed discussion and description of experimental procedures as well as the accompanying references are to be found in each individual chapter alone.

Summary

This cumulative dissertation is based on three publications. It is investigated how colloidal chemistry can be applied to improve the thermoelectric figure of merit (zT) of common bulk materials for thermoelectric applications. Materials of choice are bismuth telluride, antimony bismuth telluride, lead telluride and lead selenide. Solution-based synthetic procedures are described to control size, size-distribution and shape of all four materials and to obtain well-separated nanoparticles on the gram-scale per batch.

A ligand removal procedure is developed which, followed by compaction with spark plasma sintering, gives access to macroscopic samples of nanostructured, polycrystalline materials with grains of size and shape comparable to those of the individual nanoparticles.

The macroscopic nanostructured samples are characterized in terms of their chemical composition, crystalline phase, microstructure, electric and thermal conductivity, thermopower, specific heat and thermoelectric figure of merit.

From a chemist's point of view, particular emphasize is put on identifying mechanistic details for controlling size and shape of the nanoparticles.

It is shown that colloidal chemistry is capable of giving access to an unprecedented control over the grains of a macroscopic nanostructured sample in terms of their size, size-distribution and shape which allows testing the effect of these parameters onto thermoelectric properties.

From a physicist's perspective, theoretical concepts for improved thermoelectric materials' performance are tested. Amongst them are grain boundary scattering, the phonon-glass electric-crystal effect and potential barrier energy filtering.

It is demonstrated how nanostructures allow to discriminate between charge-carrier and phonon transport on benefiting from their different mean-free-paths. This culminates in a pronounced phonon-glass electron-crystal effect resulting in enhanced thermoelectric figures of merit. Potential barrier energy filtering is realized with suitable core-shell structures verifying the potential for multi-fold increases in thermopower. For the investigated structures, the effect is explicitly found to be dependent on the height of the potential barrier and not on the limited dimensions of the nanograins.

The results of this work are intended to stimulate the application of the advantages of colloidal chemistry for thermoelectric research. This includes the control of grain size, size-distribution and shape as well as the access to heterostructured materials with complex band edge alignments like core-shell nanoparticles.

Zusammenfassung

Der vorliegenden kumulativen Dissertation liegen drei Veröffentlichungen zu Grunde. Es wird untersucht, wie Kolloidchemie dazu genutzt werden kann, die thermoelektrische Gütezahl (zT) bekannter thermoelektrischer *bulk* Materialien zu erhöhen. Materialien der Wahl sind Bismuttellurid, Antimonbismuttellurid, Bleitellurid und Bleiselenid. Es werden nasschemische Synthesewege beschrieben, mit denen sich die Größe, Größenverteilung und Form der Kristalle aller vier Materialien einstellen lassen und Ausbeuten im Grammmaßstab erhältlich sind.

Eine Anleitung zur Entfernung der koordinierenden Liganden von den erhaltenen Nanokristallen wird entwickelt. Durch Kompaktierung der so gereinigten Nanokristalle mittels *spark plasma sintering* werden makroskopische Proben nanostrukturierter, polykristalliner Festkörper dargestellt, deren kristallinen Domänen dieselben Eigenschaften in Bezug auf Größe und Form haben wie die verwendeten Nanopartikel.

Diese makroskopischen, nanostrukturierten Proben werden hinsichtlich chemischer Zusammensetzung, kristalliner Phase, Mikrostruktur, elektrischer und thermischer Leitfähigkeit, Thermokraft, spezifischer Wärmekapazität und thermoelektrischer Gütezahl charakterisiert.

Aus chemischer Sicht wird ein Schwerpunkt auf mechanistische Details bezüglich der Kontrolle von Größe und Form der Nanopartikel gelegt.

Es wird deutlich, dass Kolloidchemie eine unerreichte Kontrolle über Mikrostruktur der dargestellten makroskopischen, nanostrukturierten Proben im Hinblick auf ihre Korngrößen sowie deren Größenverteilung und Formen bietet.

In physikalischer Hinsicht werden theoretische Konzepte zur Verbesserung der thermoelektrischen Gütezahl einem Praxistest unterzogen. Dies beinhaltet die Streuung an Korngrenzen, den Phononen-Glas Elektronen-Kristall Effekt und Energiefiltration durch Potentialbarrieren.

Es wird erarbeitet, wie sich mittels Nanostrukturen zwischen Ladungsträger- und Phononentransport unterscheiden lässt, indem man sich die Unterschiede in den mittleren freien Weglängen zu Nutze macht. Als Ergebnis ist ein ausgeprägter Phononen-Glas Elektronen-Kristall Effekt und eine dadurch bedingte Erhöhung der thermoelektrischen Gütezahl festzustellen.

Für die in dieser Arbeit untersuchten Kern-Schale-Strukturen kann der Effekt der Energiefiltration durch Potentialbarrieren und eine Vervielfachung der Thermokraft beobachtet werden. Der Effekt beruht ausdrücklich auf der Höhe der Potentialbarriere und nicht auf der Nanostruktur der Proben.

Die Ergebnisse dieser Arbeit sollen die Aufmerksamkeit der thermoelektrischen Forschungsaktivitäten auf die Nutzung der Vorteile der Kolloidchemie lenken. Hierbei sind sowohl die hervorragende Kontrolle über Größe, Größenverteilung und Form der kristallinen Domänen zu nennen, als auch der Zugriff auf heterogene Materialien mit komplexen Bandkantenarrangements wie Kern-Schale Nanospartikel.

Index

Register of abbreviations

σ	**Electric conductivity**
ρ	**Resistivity**
κ	**Total thermal conductivity**
κ_l	**Lattice thermal conductivity**
κ_e	**electronic thermal conductivity**
S	**Thermopower or Seebeck coefficient**
zT	**Thermoelectric figure of merit**
C_p	**Specific heat capacity**
(HR-)TEM	**(High resolution) Transmission electron microscopy**
SEM	**Scanning electron microscopy**
EDXS	**Energy dispersive X-ray spectroscopy**
SPS	**Spark plasma sintering**
XRPD	**X-ray powder diffraction**
SAED	**Selected area electron diffraction**
TOP	**Trioctylphosphine**
DDT	**1-dodecanethiol**
FFT	**Fast Fourier transformed**
ICP-OES	**Inductively coupled plasma optical emission spectroscopy**
PGEC	**Phonon-glass electron-crystal**
η	**Carnot efficieny**
BTE	**Boltzmann transport equation**
m^*	**Effective mass**
m_0	**Mass of the free electron**
RTA	**Relaxation time approximation**
L	**Lorenz number**
s	**Scattering parameter**
n	**Carrier density**
N_C	**Effective density of states**
Θ_D	**Debye temperature**
τ	**Relaxation time**
μ	**mobility**
E_F	**Fermi level**
d_t	**Thermal diffusivity**

Chapter A

Theory

Introduction

In the light of rapidly vanishing fossil energy resources, the search for alternative power generation has turned into one of the most important fields for scientific research. Thermoelectric power generation is based on the “Seebeck effect”, discovered by Lord Thomas Seebeck 1821, who measured a significant potential difference alongside a bismuth single crystal upon applying a temperature gradient between the two ends of the crystal. After more than a century of mainly academic interest, the Seebeck effect received widespread attention by engineers for potential industrial applications with the discovery of a pronounced Seebeck effect in bismuth telluride, Bi_2Te_3. By the end of the 1950s thermoelectric devices based on Bi_2Te_3 were standardly fabricated combining unprecedented reliability with a Carnot efficiency of 7%. With these characteristics thermoelectric devices quickly became part of the dynamic activities of US and Sowjet researchers in their attempts to build reliable space crafts and satellites even for outer-solar missions. Until today, the preferred energy source for long range satellite missions (for example Voyager 1&2, Pioneer 10&11, Cassini, Apollo 11, Mars Pathfinder, etc.) is an onboard radioactive material whose released heat during decay is converted into electricity by a thermoelectric device. Thus equipped satellites are independent of solar radiation in their energy supply and run reliably over several decades which is crucial for deep space missions.

Despite extensive research activities, thermoelectric devices have not yet led to widespread market applications where reliability does not have top-priority such as terrestrial power generation. This is solely due to the relatively small Carnot efficiency in combination with a need for expensive materials like tellurium. I emphasize that thermoelectric power generation is a complementary source of energy which purely functions with the lowest grade of all energy forms: waste heat. In principle, it can be combined with any electrical device since heat dissipation is an unavoidable consequence of Joule heating encountered in every electric circuit. Due to the second law of thermodynamics and the fundamental Carnot equation for energy conversion derived from it, practically all processes of power generation are prone to release most of their total energy as waste heat. It is estimated that over 95 % of all electrical energy consumed on earth is lost in this way. Every fraction of it reconverted into high grade electric energy by thermoelectric devices reduces the total energy demand, conserves non-regenerative energy resources and decreases the release of greenhouse gases. However, at the current efficiency-to-expense-ratio this technology is economically unattractive.

Another closely related phenomenon to the Seebeck effect is the “Peltier effect”, discovered by Jean Peltier 1834. Here, applying a potential gradient to a crystal generates a heat flow and thus a cooling effect alongside the potential gradient. This effect combines good cooling rates with small and light devices. Where this has already led to applications for mobile cooling devices (eg. Camping coolers), advances in computer technologies create a rapidly growing demand for Peltier elements. Modern transistor microchips are so small that adequate heat dissipation away from the sensitive devices is a critical issue. Semiconductor diodes can only work reliably within a narrow temperature window and fan-based cooling is pushed to its limits as state-of-the-art transistor units enter the sub-micrometer regime. The search for ever-smaller electronic devices like laptops, mobile phones and mp3-players is also a search for more punctual and highly localized cooling. Thermoelectric materials will play an important role in this respect. Again, the extend of this participation crucially relies on cooling efficiencies of these materials.

Before taking a detailed look at the fundamental principles of thermoelectrics and the physical phenomena involved to create strategies for building more efficient materials, a few general facts should be considered:

It is estimated that a threefold increase over state-of-the-art devices would lift thermoelectric power generation to economical competitiveness with conventional processes. Due to lacking alternatives such an increase is not even necessary for selling Peltier devices although it would certainly accelerate its widespread use and the development of ultra-small electronic equipment.

Tellurium is rarely abundant on earth and its price has seen a substantial increase over the last decades. This development is likely to continue. It would be a great advantage to find a material with an equally good thermoelectric performance at room temperature like that of Bi_2Te_3 which does not contain tellurium.

Development of thermoelectric materials has been predominantly a field for researchers from US, Russia or the Far East. Contributions of European research groups in this respect have been fairly limited. In the light of a worldwide market volume of € 500 Mio. per year and an estimated ten-fold increase in case of just doubling thermoelectric efficiencies, several European countries have launched initiatives to participate in the on-going development. Specifically, Germany has set up the Priority Program 1386 on “Nanostructured Thermoelectrics” with a total funding period of six years until 2015. Whether wide-spread interest in thermoelectric research will persist after this period crucially relies on whether or not new strategies can be found to substantially increase thermoelectric efficiencies and raise efficiency-to-expense-ratios towards economically attractive levels.

Thermoelectric devices

A fully operative thermoelectric device consists of a p- and an n-type material connected in series in a loop arrangement. The term “x-type” is a relative expression meaning a material in which there is an excess of one type of charge carrier (electrons or holes) over the total amount of this type of charge carrier in the other material. Thus, the two materials are not limited to semiconductors but could be any material from insulator to metal.

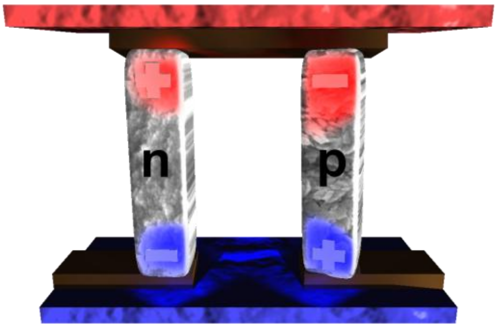

Figure A-1: Basic set-up for thermoelectric power generation. An n-type and a p-type material are connected electrically in series in a looped arrangement. Applying a temperature gradient between the upper and lower side leads to a charge separation due to differences in the charge-carriers kinetic energies at the two sides. This creates a potential difference in the device which may be used to power an external electric circuit.

In Seebeck power generation, one side of the device is heated by an external source so as to establish a temperature gradient alongside the two materials. This leads to an excess of kinetic energy of charge carriers on the hot side in each of the two materials. The result is a net flow of the predominant type of charge carrier towards the cold side of the device. In the n-type material, this generates a flow of electrons and thus a negative charge at the cold side whereas in the p-type material holes flow to the cold side generating a positive charge (**Figure 1**). Under open-circuit conditions this leads to a flow of charge carriers from one side of the device to the other which can be used to power an electric consumer load. In other words, the input of a certain amount of heat has led to an output of a certain amount of electricity, so heat was converted into electric energy.

In Peltier cooling, this concept is practically reversed. Applying a potential difference between both ends of the device leads to a flow of the predominant charge carrier in each of the two materials towards the same side. As this side accumulates more and more charge carriers, the probability for collisions rises resulting in this end of the material to heat up. Simultaneously, the other end of the material will cool down. In other words, a potential difference has triggered a heat flow across the device which can be applied to cool an external consumer load.

Qualitatively, it is straight forward to speculate about the physical parameters affecting the efficiency of this device. Since each charge carrier contributes to the conversion process, a large flow of carriers per unit time will improve the device performance. Hence, the efficiency will positively depend on electric conductivity (σ).

The ability to maintain a large temperature gradient across the device is either a precondition to run the device (Seebeck power generation) or the purpose of the device itself (Peltier cooling). This can only be achieved if thermal conductivity (κ) across the device is poor. Hence, the efficiency will be inversely proportional to the thermal conductivity.

Despite the total amount of charge carriers, the energy per charge carrier will also play an important role. A large energy-to-charge-carrier-ratio in Peltier cooling means that a relatively small potential gradient is sufficient to transfer a large amount of heat. This ratio is expressed in the so-called Seebeck coefficient or thermopower (S). Hence, the efficiency will positively depend on S.

As will be shown later, a convenient measure for the quality of a thermoelectric material (not device!) is the so-called thermoelectric figure of merit (zT):

(1) $$zT = \frac{\sigma S^2}{\kappa} T,$$

with T being the average temperature of the material in Kelvin.

S can be positive (holes) or negative (electrons) depending on the type of predominant charge carrier in the material. If all constituting parameters in the two combined materials had the same absolute value (which is actually unrealistic), the figure of merit of the complete device (ZT) would be the same as that of the individual materials (zT).

Then, the mathematical relation between ZT and the Carnot efficiency (η) is given by:

(2) $$\eta = \frac{\Delta T}{T_h} \cdot \frac{\sqrt{1+ZT}-1}{\sqrt{1+ZT}+\frac{T_c}{T_h}},$$

with ΔT being the temperature gradient across the device and T_c and T_h the hot-side and cold-side temperature, respectively. In reality, ZT is always smaller than zT since it is almost impossible to find a p-type material which exactly matches the physical properties of the n-type equivalent. In such a case, ZT must be derived iteratively from individual zTs which is especially true for large ΔTs.

For convenience, thermoelectric materials are mostly classified in terms of their zT, and not ZT (let alone η) but it is important to stress the difference in between the two terms and to underline that two materials with high zT do not necessarily combine to a device with high ZT or η. For the rest of this work, only individual zTs will be considered.

For a quantitative understanding of zT, it is mandatory to derive its constituting parameters σ, κ and S from fundamental physics. Classically, this may be done by solving the Boltzmann transport equation.

The Boltzmann transport equation

The distribution function

To quantitatively describe a system with a finite number of allowed states, the Boltzmann transport equation (BTE) assigns each carrier in the system a probability to occupy a certain state. At the heart of this description lies the distribution function which is a number between zero and one. From Newton's fundamental laws of mechanics we know that the state of a carrier can be described as a function of its momentum **p** and position **r** (both of which are vectors, denoted by bold notation) at a certain time t (which is a scalar). Consequently, the Boltzmann distribution function depends on these three variables and will be denoted in the following as $f\,(\mathbf{r},\mathbf{p},t)$. In equilibrium, this function is identical to the Maxwell-, Fermi-Dirac- or Bose-Einstein-distribution function depending on the nature of the carriers. If a system is in equilibrium, this will be denoted by expressing its distribution function as $f_0\,(\mathbf{r},\mathbf{p},t)$.

If a system is moved out of equilibrium by a scattering event, $f\,(\mathbf{r},\mathbf{p},t)$ will be different from $f_0\,(\mathbf{r},\mathbf{p},t)$ forcing a change in **p** and/or **r** with time until equilibrium is reached. The purpose of the BTE is to find $f\,(\mathbf{r},\mathbf{p},t)$. Once the non-equilibrium $f\,(\mathbf{r},\mathbf{p},t)$ has been found, it can be used to derive a large number of physical properties of interest. For instance, one may ask for the average density of carriers ($n(\mathbf{r},t)$) centered about **r** at time t in a volume Ω by summing over all carriers in each momentum state:

$$\textbf{(3)} \qquad n(\boldsymbol{r},t)=\frac{1}{\Omega}\sum_{\boldsymbol{p}} f\,(\boldsymbol{r},\boldsymbol{p},t)$$

Similarly, on assuming spherical, parabolic bands one may obtain the average kinetic energy density of the carriers with an effective mass m* within a volume Ω as:

$$\textbf{(4)} \qquad E_{kin}(\boldsymbol{r},t)=\frac{1}{\Omega}\sum_{\boldsymbol{p}}\frac{\boldsymbol{p}^{2}}{\boldsymbol{2m}^{*}} f\,(\boldsymbol{r},\boldsymbol{p},t,)$$

As we will see shortly, the parameters σ, κ and S can be derived in a similar fashion.

Hence, the question for the transport properties of a system is a question for its non-equilibrium distribution function which can be answered by solving the BTE. If we represent all scattering events moving a system out of equilibrium by a general collision integral $\left.\frac{\partial f}{\partial t}\right|_{Coll}$, then this term must be equal to the change in position ($\nabla_r f$), the change in momentum ($\nabla_p f$) and the actual distribution function. Following Newton's mechanics, a change in position is due to the velocity vector **v** and a change in momentum due to the force vector **F**. The BTE of this system becomes:

$$\frac{\partial f}{\partial t} + \mathbf{v} \cdot \nabla_{\mathrm{r}} f + \mathbf{F} \cdot \nabla_{p} f = \left.\frac{\partial f}{\partial t}\right|_{coll} . \qquad \textbf{(5)}$$

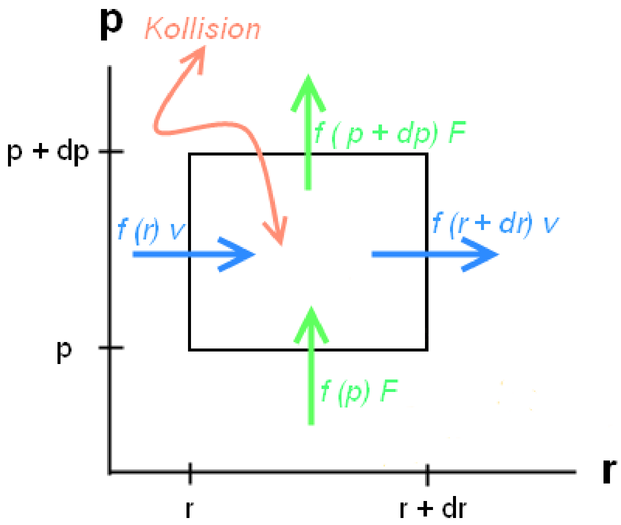

Figure A-2: 2D-description of the Boltzmann transport equation in position-momentum space. The selected area represents a distribution function ***f*** (r,p) and its change within a time t. Any in- or out-scattering of a particle will have to be answered by a change in position and/or momentum to restore the initial area (which is equivalent to a specific ***f*** (r,p))

To understand this equation, consider a two-dimensional position-momentum space. Any selected area in this space represents an *f* (**r**,**p**) within a time element t. If carriers are scattered into the selected area, the system will have to respond to this event by changing its average momentum and/or velocity in order to compensate for the gain in **p** or **r**. If the in-flow exceeds the out-flow within time t, then *f* (**r**,**p**) must change and the physical characteristics of the system will change as well. If we expand this picture into three-dimensional space, the BTE becomes a six-dimensional equation in position-momentum (or phase) space.

Solving this equation can be complicated and often asks for the applicability of certain assumptions. One popular assumption is that of the constant relaxation time approximation (RTA). Briefly, it assumes that the time needed for *f* (**r**,**p**,t) to relax to f_0 (**r**,**p**,t) is independent of *f* (**r**,**p**,t) and can be expressed by a system specific constant relaxation time τ_f. One often finds that this greatly practical assumption holds true if the displacement of *f* (**r**,**p**,t) from equilibrium is small, that is, in the case of low-field transport and if scattering events are either isotropic or elastic.

Another important question is that of the validity of the BTE itself. Since it is derived from classical physics, the dimensions of the system studied are important. If the mean free path of a carrier is not significantly greater than its wavelength, the limits of classical physics are reached and quantum mechanical expressions are needed. This may very well be the case for the nanostructured materials studied in this work. However, to derive the fundamental physics of thermoelectric phenomena, we shall assume macroscopic systems and the validity of the RTA in order to arrive at analytical solutions.

Solutions to the Boltzmann transport equation

For Fermions, the equilibrium distribution function f_0 (**r**,**p**,t) is of the nature

$$f_0 = \frac{1}{\exp[\Theta]+1}, \tag{6}$$

where Θ contains the total energy of the carrier in units of $k_B T$. This total energy is the sum of the carriers potential ($E_{c0}(\mathbf{r},t)$ and kinetic energy ($E(\mathbf{p})$ minus the energy of the Fermi level (E_F). The potential is independent of momentum, whereas the kinetic energy is independent of position.

If f (**r**,**p**,t) is moved away from equilibrium, it is instructive to think of the perturbed distribution function as the sum of a symmetric and an antisymmetric distribution function:

$$f = f_S + f_A \tag{7}$$

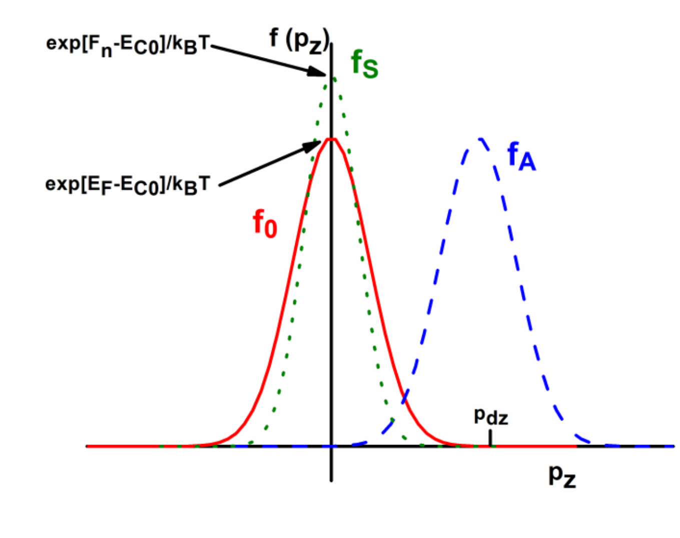

Figure A-3: Equilibrium, symmetric and antisymmetric distribution functions in momentum space. The equilibrium and symmetric distribution function are symmetric around **p** = 0 and carry no total momentum. f_S evolves from f_0 by replacing E_F with a position-dependent quasi-Fermi level F_n. f_A is non-zero in momentum and accounts for all dynamic processes. Adding f_S and f_A yields the non-equilibrium distribution function f(**r**,**p**) of interest.

The meaning of these two functions is illustrated in **Figure A-3**. The equilibrium distribution function f_0 is centred about **p = 0** with its maximum depending on the position of the Fermi level. Any symmetric alteration of f_0 leads to a non-equilibrium distribution function f_S shifted along the y-axis. Integrating over all occupied states of momentum yields zero average velocity and no current flows. It follows that f_S cannot be the correct perturbed distribution function by itself. The advantage of f_S is that we can easily deduce it from f_0 by replacing the Fermi level with the quasi-Fermi level ($F_n(\mathbf{r},t)$) which plays the role that E_F did in equilibrium but is now dependent on the carriers' position.

Hence, we have

$$\textbf{(8)} \qquad \Theta = \frac{E_{C0}(\mathbf{r},t) + E(\mathbf{p}) - F_n(\mathbf{r},t)}{k_B T_L(\mathbf{r},t)},$$

with $T_L(\mathbf{r},t)$ being the temperature of the system's lattice which may vary with position in case of a temperature gradient.

In contrast, f_A is a distribution function which is shifted from f_0 alongside the x-axis. Integrating over all occupied states of momentum yields a non-zero result and thus, f_A is responsible for any current flow in the device. This distribution function will have to be derived by solving the BTE. To do so, we will have to substitute $f = f_S + f_A$ into **(5)**. An important assumption which greatly simplifies this substitution is that $f_S >> f_A$. Further, we assume the same for the first derivatives: $\nabla_p f_S >> \nabla_P f_A$ and $\nabla_r f_S >> \nabla_r f_A$. Where this may be difficult to justify, it often leads to meaningful and self-consistent results. In the case of $\frac{\partial f_S}{\partial t}$ and $\frac{\partial f_A}{\partial t}$ one should consider that the former is symmetric in momentum and carries zero average velocity. Hence, it must be invariant in time and the differential vanishes. In contrast, the antisymmetric term carries non-zero average velocity and its differential is non-zero, too. If we recall the RTA, then we may substitute $\frac{\partial f_A}{\partial t} = \frac{f_A}{\tau_f}$.

On applying these assumptions and steady-state conditions ($\left.\frac{\partial f}{\partial t}\right|_{Coll} = 0$), **(5)** becomes

$$\textbf{(9)} \qquad \mathbf{v} \cdot \nabla_{\mathbf{r}} f_S + \mathbf{F} \cdot \nabla_p f_S = -\frac{f_A}{\tau_f}$$

Applying the chain rule to **(9)** and partial differentiation with respect to **r** and **p**, we find:

$$\textbf{(10)} \qquad \mathbf{v} \cdot \frac{\partial f_S}{\partial \Theta} \nabla_r \Theta + \mathbf{F} \cdot \frac{\partial f_S}{\partial \Theta} \nabla_p \Theta = -\frac{f_A}{\tau_f}$$

with

$$\textbf{(11)} \qquad \nabla_r \Theta = \frac{\nabla_r E_{C0}(\mathbf{r}) - \nabla_r F_n(\mathbf{r})}{k_B T_L(\mathbf{r})} + [E_{C0}(\mathbf{r}) + E(\mathbf{p}) - F_n(\mathbf{r})] \nabla_r \left(\frac{1}{k_B T_L(\mathbf{r})} \right)$$

and

$$\textbf{(12)} \qquad \nabla_p \Theta = \frac{\nabla_p E(\mathbf{p})}{k_B T_L} = \frac{\nabla_p \mathbf{p}^2}{2m^* k_B T_L} = \frac{\mathbf{p}}{m^* k_B T_L} = \frac{\mathbf{v}}{k_B T_L}$$

if spherical, parabolic bands are assumed. Inserting **(11)** and (**12)** into **(10)** yields

$$\textbf{(13)} \qquad f_A(\mathbf{r}, \mathbf{p}, t) = \frac{\tau_f}{k_B T_L} \left(\frac{-\partial f_S}{\partial \Theta} \right) \mathbf{v} \cdot \mathbf{F},$$

with

$$\textbf{(14)} \qquad \mathbf{F} = -\nabla_r F_n(\mathbf{r}) + T_L [E_{C0}(\mathbf{r}) + E(\mathbf{p}) - F_n(\mathbf{r})] \nabla_r \left(\frac{1}{T_L} \right)$$

being a generalized force. For convenience, we assume that the system is in zero magnetic field. Otherwise, the magnetic force field would have to be added to **F**.

When comparing **(13)** with **(5),** we have arrived at an expression for the actual distribution function of interest (the one responsible for system inherent dynamic processes) characterized by a certain relaxation time τ_f. With this function, we can derive the fundamental physical parameters of the system as demonstrated in **(3)** and (**4)**. It should be stressed that the assumptions made to arrive at **(13)** hold true only in the low-field case when perturbations are small, when the RTA applies and if spherical, parabolic bands are present.

Since we are interested in carrier transport, we need to evaluate the antisymmetric distribution function in terms of its electric current density (for electric transport) and kinetic energy current (for thermal transport). In a volume Ω, the former is given by $J = \frac{-q\mathbf{v}}{\Omega}$ and the latter by $J_Q = \frac{[E_{C0}(\mathbf{r}) + E(\mathbf{p}) - F_n(\mathbf{r})]\mathbf{v}}{\Omega}$. Applying these equations to f_A, summing over all states of momentum and substituting into **(13)** yields:

$$\textbf{(15)} \qquad J = \frac{-q}{\Omega k_B T_L} \sum_{\mathbf{P}} \boldsymbol{\upsilon}(\boldsymbol{\upsilon} \cdot \mathbf{F}) \tau_f \left(\frac{-\partial f_S}{\partial \Theta} \right)$$

and

$$\textbf{(16)} \qquad J_Q = \frac{-q}{\Omega k_B T_L} \sum_{\mathbf{P}} \boldsymbol{\upsilon}(\boldsymbol{\upsilon} \cdot \mathbf{F}) \tau_f \left(\frac{-\partial f_S}{\partial \Theta} \right) [E_{C0} + E(\mathbf{p}) - F_n].$$

When comparing **(14)** with **(15),** one can write

$$\textbf{(17)} \qquad J = \sigma \cdot \nabla_r \left(\frac{F_n}{q} \right) + B \cdot \nabla r \left(\frac{1}{T_L} \right)$$

with

$$\textbf{(18)} \qquad \sigma = \frac{q^2}{\Omega k_B T_L} \sum_{\mathbf{P}} \nu \nu \tau_f \left(\frac{-\partial f_S}{\partial \Theta} \right)$$

and

$$\textbf{(19)} \qquad B = \frac{-q}{\Omega k_B T_L} \sum_{\mathbf{P}} \nu \nu \tau_f T_L [E_{C0}(\mathbf{r}) + E(\mathbf{p}) - F_n] \left(\frac{-\partial f_S}{\partial \Theta} \right).$$

It shows that the driving forces for an electric current to flow are gradients in the quasi-Fermi level and inverse temperature. Similarly, on comparing **(14)** with **(16)**, we obtain

$$\textbf{(20)} \qquad J_Q = p \cdot \nabla_r \left(\frac{F_n}{q} \right) + K \cdot \nabla r \left(\frac{1}{T_L} \right)$$

with

$$\textbf{(21)} \qquad p = \frac{-q}{\Omega k_B T_L} \sum_{\mathbf{P}} \nu \nu \tau_f [E_{C0}(\mathbf{r}) + E(\mathbf{p}) - F_n] \left(\frac{-\partial f_S}{\partial \Theta} \right)$$

and

$$\textbf{(22)} \qquad K = \frac{1}{\Omega k_B} \sum_{\mathbf{P}} \nu \nu \tau_f [E_{C0}(\mathbf{r}) + E(\mathbf{p}) - F_n]^2 \left(\frac{-\partial f_S}{\partial \Theta} \right).$$

Thus, the driving forces for electric and heat current are identical. Note that these equations only apply to cubic semiconductors. For anisotropic materials, the four transport coefficients σ, B, p and K need to be expressed as tensors.

(17) and (**20)** are called *coupled current equations* and form the basis for every device analysis. If we assume constant carrier density in the device, $\nabla_r\left(\frac{F_n}{q}\right)$ can be replaced by the electric field (ε). From an experimental point of view, one would prefer to apply a certain current and temperature gradient to a sample to generate an electric field rather than the other way around. Thus, **(17)** should be rearranged with respect to ε to find

$$\varepsilon = \rho J + S\nabla_r T_L \tag{23}$$

with

$$\rho = \frac{1}{\sigma} \tag{24}$$

and

$$S = \frac{\rho B}{T_L^2}. \tag{25}$$

Finally, we may write **(20)** in terms of the expression for ε denoted in **(23)** to obtain

$$J_Q = \pi J - \kappa\nabla_r T_L \tag{26}$$

with

$$\pi = p\rho \tag{27}$$

and

$$\kappa_e = \frac{1}{T_L^2}(K - p\rho B). \tag{28}$$

From **(26)** we learn that heat current flow occurs due to a gradient in temperature or due to an electric current. The latter may be interpreted as Joule heating.

The transport coefficients in **(24), (25), (27)** and **(28),** ρ, S, π and κ_e are well known and termed resistivity, thermopower, peltier coefficient and (electronic) thermal conductivity, respectively. We have derived the constituting physical parameters of **(1)** by applying Newton's laws of motion to the Fermi-Dirac distribution function.

In the current form, the transport coefficients are of little practical use as each of them contains a sum over all states of momentum which yet has to be evaluated.

The mathematics involved has been described elsewhere and will not be reproduced here.[1] The goal of this evaluation is an expression of the transport coefficients in terms of the carriers' effective mass m^* and a relaxation time τ_f characteristic for the scattering event that caused the perturbation from equilibrium. The solutions for the four transport coefficients are:

$$\textbf{(29)} \qquad \rho = \frac{1}{nq\mu_n}$$

where

$$\textbf{(30)} \qquad \mu_n = \frac{q\langle\langle\tau_f\rangle\rangle}{m^*}$$

with

$$\textbf{(31)} \qquad \langle\langle\tau_f\rangle\rangle = \frac{\langle E\tau_f(E)\rangle}{\langle E\rangle} = \tau_0 \frac{\Gamma(s+5/2)}{\Gamma(5/2)}.$$

μ_n is the carrier mobility which according to **(30)** is a function of an average, energy weighted relaxation time. This average relaxation time carries information about the process specific, constant relaxation time τ_0 and its energy dependence. For nondegenerate semiconductors ($n << N_C$), it has the nature

$$\textbf{(32)} \qquad \tau_f(E) = \tau_0 \left(\frac{E(\mathbf{p})}{k_B T_L}\right)^s$$

where "s" a characteristic exponent for a specific scattering mechanism. The Γ-function occurs on evaluating the integral in **(31)** and is defined as

$$\textbf{(33)} \qquad \Gamma(p) = \int_0^\infty y^{p-1} e^{-y} dy.$$

In continuation, we have

$$\textbf{(34)} \qquad S = \frac{k_B}{(-q)}\left[\ln\left(\frac{N_C}{n}\right) + (s+5/2)\right]$$

with the effective density of states $N_C = 2\left(\frac{2\pi m^* k_B T_L}{h^2}\right)^{3/2}$ and the carrier density *n*. The important result is that S depends on the mechanism of carrier scattering. However, since $\left(\ln \frac{N_C}{n}\right)$ can be quite large for nondegenerate semiconductors, the effect is relatively weak.

Further, it is

$$\textbf{(35)} \qquad \pi = T_L S$$

and

$$\textbf{(36)} \qquad \kappa_e = T_L \left(\frac{k_B}{q}\right)^2 \frac{(s+5/2)}{\rho}.$$

(35) is known as the *Kelvin relation* where **(36)** is the Wiedemann-Franz law with $\frac{k_B{}^2(s+5/2)}{q^2}$ being the scattering parameter dependent Lorenz number (L).

It must be stressed that a variety of assumptions had to be made to arrive at these expressions. In particular, we have assumed spherical and parabolic bands for the kinetic energy term, the validity of the RTA to solve the BTE, nondegenerate semiconductors ($n < N_C$) to apply a simple scattering power law and cubic crystal structures to exclude effects of anisotropic conduction. Nonetheless, these expressions are of high practical use as they are easily accessible by experiment and provide useful estimates even for systems where the assumptions cannot be justified.

For example, we may substitute **(29)**, (**34)** and (**36)** into **(1)** to predict the influence of the density of states, the carrier concentration and the scattering parameter onto the thermoelectric figure of merit.

A particular emphasis should be put onto the fact that these results apply solely to nondegenerate semiconductors. If we set s = -1/2 in **(36)** (which, despite being a reasonable estimate, will be justified at a later point) we obtain $L = 1.49 * 10^{-8}\ V^2K^{-2}$ which differs considerably from the Wiedemann-Franz result for metals of $L = 2.44 * 10^{-8}\ V^2K^{-2}$. The reason for this is the assumption of $n < N_C$ we have made to evaluate **(31)** and describe the case of nondegenerate semiconductors. For metals or degenerate semiconductors, this does not apply and **(32)** does not hold true. In this case, the integral in **(31)** has to be evaluated by a rapidly converging series until a nonzero result is obtained.

It can be shown that **(36)** is turned into

$$\textbf{(37)} \qquad \kappa_e = T_L \left(\frac{k_B}{q} \right)^2 \frac{\pi^2}{3} \frac{1}{\rho}$$

which is the Wiedemann-Franz result for metals.[2] It shows that the electronic contribution to thermal transport is greater for degenerate than for nondegenerate semiconductors whereas in the latter case there is an additional dependence on the scattering mechanism.

Further, **(34)** changes to

$$\textbf{(38)} \qquad S = \frac{\pi^2}{3} \frac{k_B}{(-q)} \left[\ln\left(\frac{N_C}{n} \right) + (s + 3/2) \right].$$

Since $n \approx N_C$ in degenerate semiconductors, the magnitude of S depends critically on the value of the scattering parameter s. The constant prefactor in **(38)** is roughly 280 µVK^{-1}. Even in the case of the small but commonly observed value of s = -1/2, one could expect extraordinary large thermopowers of 500 µVK^{-1}. In reality, this is practically never observed since highly doped materials usually show multiband conduction of charge carriers with opposite sign (electrons and holes) in which case their contributions to the total thermopower counteract and partially cancel each other.

Before concluding this chapter, it must be stressed that **(36)** merely states the electronic contribution to thermal conductivity. Especially in the case of non-metallic conductors a significant fraction of heat is transferred via lattice vibrations and adds to the total thermal conductivity. Indeed, most of the recent advances in thermoelectric research have been made my manipulating this vibrational or *phononic* contribution. Thus, we need to derive an expression for the lattice thermal conductivity (κ_L), too.

The Debye-Callaway model

Since phonons belong to the particle class of Bosons, the correct f_0 on which the BTE has to be applied is the Bose-Einstein distribution function:

$$\textbf{(39)} \qquad f_0 = \frac{1}{\exp[\Theta] - 1}$$

with

$$\textbf{(40)} \qquad \Theta = \frac{\hbar\omega}{k_B T_L}$$

where ω is the angular frequency mode of the phonon.

Applying **(9)** to this distribution function and assuming the absence of potential fields *relevant for phonons*, we obtain

$$\textbf{(41)} \qquad \mathbf{v} \cdot \nabla_{\mathbf{r}} T \frac{\partial f_s}{\partial T} = -\frac{f_A}{\tau_f}$$

within the limits of applicability of the RTA. Similar to the case of charge carriers, we may imagine f_s as a displaced Bose-Einstein function, disturbed from equilibrium in the direction of ∇T by a constant vector **l**. This displacement plays the same role as the introduction of the quasi-Fermi level in **(8)** and yields

$$\textbf{(42)} \qquad f_s = \frac{1}{\exp\left[\Theta - \dfrac{\mathbf{l} \cdot \mathbf{q}}{k_B T_L}\right] - 1}$$

with **q** being the wave vector which was displaced by **l**. Again, f_s is symmetric and zero in momentum. It is instructive to think of this displacement as the result of an elastic collision of two individual phonons within the first Brillouin zone on which their wave vectors combine to a new resultant phonon. Since this 3-phonon-process is required to conserve momentum, the resultant phonon must be located in the first Brillouin zone itself. Such a phonon scattering event is called a “normal process” (*N*-process) (**Fig. 4a**) and is non-resistive to heat transport.

In contrast, f_A is antisymmetric and hence all phonon scattering events characterized by this part of the distribution function are non-conserving in momentum. The resultant phonon should be visualized as the combination of two phonon wave vectors K1 and K2 which on collision combine to a K3 located outside the first Brillouin zone (**Fig. 4b**). Due to the periodicity of the Brillouin zone, this vector effectively enters the zone in k-space from behind the position of K1 and K2 which means that momentum has been lost. The process is resistive to heat transport. Such a scattering event is called an “Umklapp process” (*U*-process).

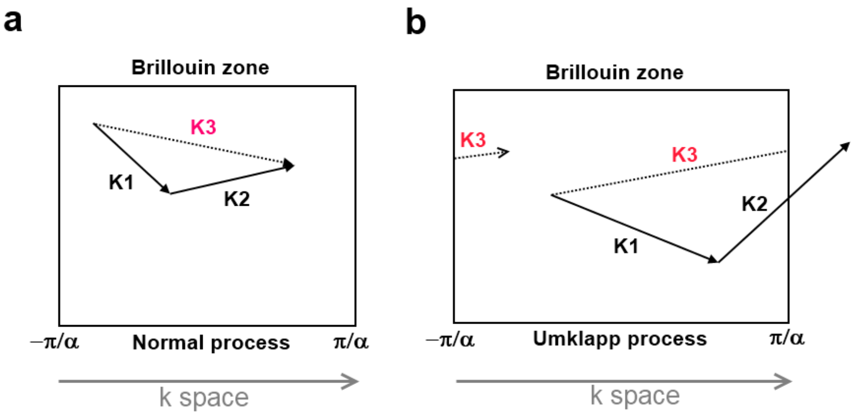

Figure A-4: *N*- and *U*-processes in the first Brillouin zone of a one-dimensional crystal. (**a**) Two phonons K1 and K2 combine on elastic collision to a new phonon K3. Since K3 carries the combined direction and magnitude of K1 and K2 *and* resides within the first Brillouin zone, the process fully conserves momentum. (**b**) Here, K3 resides outside the first Brillouin zone which is not allowed. By definition, K3 may be translated into the zone by subtracting a multiple of the width of the Brillouin zone. Since K3 has a lower magnitude than K1 and/or K2, the process is non-conserving in momentum.

The idea of the Debye-Callaway-model is to express f_S and f_A in terms of their characteristic relaxation time τ just as it has been demonstrated for charge carrier transport. The mathematical evaluation can be found elsewhere.[3] The solution expressed with respect to a characteristic transport coefficient κ_L is

$$\textbf{(43)} \qquad \kappa_L = \frac{k_B}{2\pi^2 v_S}\left(\frac{k_B\theta_D}{\hbar}\right)^3 (I_1 + \beta I_2)$$

with the speed of sound υ_S and the Debye temperature θ_D. I_1 and I_2 are the Debye-Callaway-Integrals given by

$$\textbf{(44)} \qquad I_1 = \int_0^{\theta_D/T_L} \tau_C(\Theta)\frac{\Theta^4 \exp[\Theta]}{(\exp[\Theta]-1)^2}\,d\Theta$$

$$\textbf{(45)} \qquad I_2 = \int_0^{\theta_D/T_L} \frac{\tau_C(\Theta)}{\tau_N(\Theta)}\frac{\Theta^4 \exp[\Theta]}{(\exp[\Theta]-1)^2}\,d\Theta$$

where Θ has been defined by **(40)**, τ_N is the characteristic relaxation time for *N*-processes and τ_c is the relaxation time for all combined scattering events.

The I_2-term is applied to correct for wrongfully treating *N*-processes as if they were resistive as part of τ_c. In reality, it is practically always $I_2<<I_1$ so that I_2 is often neglected. However, if samples are very pure, resistive scattering may be weak and I_2 becomes important.

In this context, the parameter β as the ratio of resistive processes to the total number of all combined processes is used as a weighing factor in the Debye-Callaway model[4]:

$$\textbf{(46)} \qquad \beta = \frac{\displaystyle\int_0^{\vartheta_D/T_L} \frac{\tau_c(\Theta)}{\tau_N(\Theta)} \frac{\Theta^4 \exp[\Theta]}{(\exp[\Theta]-1)^2} d\Theta}{\displaystyle\int_0^{\vartheta_D/T_L} \frac{\tau_C(\Theta)}{\tau_N(\Theta)\tau_r(\Theta)} \frac{\Theta^4 \exp[\Theta]}{(\exp[\Theta]-1)^2} d\Theta}$$

with τ_r being the characteristic relaxation time for all resistive processes in the system. In macroscopic and ultra-pure single crystals, τ_r is practically identical to τ_u, the relaxation time of *U*-processes. In polycrystalline and/or doped crystals however, there is a significant contribution of grain boundary and/or impurity scattering to τ_r. In the presence of an electric field, phonon-electron scattering will have to be considered, too.[5] Lastly, for elements with at least two frequently abundant isotopes, scattering by isotopes can have an important contribution as well.[6]

Although they may appear somewhat trivial, the importance of *N*-processes for total thermal conductivity must not be underestimated. *N*-processes occur frequently and help forming broad phonon dispersions by elastically scattering a wave package of phonons over a large number of different wave vectors. These wave vectors are in turn scattered by the resistive processes mentioned above which leads to a finite thermal conductivity. As indicated in **(44)** to (**46)**, all relaxation times depend on the phonons' wave vector through Θ. As we will see now, certain resistive processes are highly effective in scattering phonons of a narrow range of wave vectors whereas their influence may be almost negligible for phonons from a different part of the dispersion spectrum. Without phonon dispersion induced by *N*-processes, many resistive processes would be ineffective and the total thermal conductivity of the system significantly higher although there is no *direct* contribution of *N*-processes to thermal resistance.

To calculate τ_r and τ_c we need a formula to combine the individual relaxation times. In this respect, *Matthiesen's* rule is of great practical use which states that two scattering processes *i* and *j* combine in terms of their relaxation times as

$$\frac{1}{\tau_{ij}} = \frac{1}{\tau_i} + \frac{1}{\tau_j}. \tag{47}$$

Thus, we have

$$\frac{1}{\tau_c} = \frac{1}{\tau_N} + \frac{1}{\tau_r} \tag{48}$$

and on assuming only Umklapp, grain boundary and impurity scattering

$$\frac{1}{\tau_r} = \frac{1}{\tau_U} + \frac{1}{\tau_{GB}} + \frac{1}{\tau_I}. \tag{49}$$

It must be stressed that **(47)** is a rule and not a law which only applies if the characteristic scattering parameters s_i and s_j as introduced in **(32)** are identical. Although this is far from certain for realistic systems, this fact is mostly ignored in many present treatments of lattice thermal conductivities and **(47)** is widely applied like a fundamental law. This should be viewed with scepticism.

Returning to the initial quest for an analytical expression of the lattice thermal conductivity, κ_L, the Debye-Callaway integrals in **(43)** must be evaluated. For this, expressions of the angular dependence of the individual relaxation times τ_U, τ_N, τ_{GB} and τ_I are required. It can be shown that it is:[7,8,9]

$$\tau_U^{-1} = B_1 \omega^2 T^3, \tag{50}$$

$$\tau_N^{-1} = B_2 \omega^2 T^3, \tag{51}$$

$$\tau_{GB}^{-1} = \frac{v_S}{L}, \tag{52}$$

with the dimension of the crystal L,

$$\tau_I^{-1} = A\omega^4. \tag{53}$$

For simplicity, the constants A, B_1 and B_2 are not evaluated here in greater detail. Their exact nature is always a matter of debate and requires considerable experimental data to accurately treat specific cases. Briefly, they require knowledge of the Debye temperature, different behaviour of longitudinal versus transverse phonon modes, crystal symmetries, mass differences of atoms and many more.[10]

What we can immediately see from **(50)** to (**53)** is the different angular and temperature dependence of specific resistive scattering events. Impurity scattering is most effective in scattering high frequency modes where Umklapp scattering scales strongly with temperature. The former can be understood if we consider the scale of typical phonon modes. They are typically located in the THz regime which in combination with typical sound velocities v_S in solids of 3000-4000 ms^{-1} result in wavelengths of several Å to a few nm. Occasional impurities in macroscopic systems occur on the scale of Å and can only interact with phonons of short wavelengths. Thus, impurity scattering is only effective for high frequency phonons.

The temperature dependence of *U*-processes becomes obvious as we recall **Figure 4b**. For *U*-processes to occur the phonon wave vectors need to be sufficiently large to result in a phonon outside the Brillioun zone. At temperatures significantly below the Debye temperature θ_D only phononic states of small wave vectors are populated and the probability for *U*-processes is small. At $T \geq \theta_D$, there will be a suitable phonon for every imaginable phonon mode to result in a *U*-process upon collision, and thus, the probability for *U*-type scattering is large. The additional dependence on the angular frequency stems from the fact that high frequency phonons can undergo a *U*-process with a second phonon of a broad range of frequencies whereas low-frequency phonons necessarily require a phonon of elevated frequency in order to result in a non-momentum-conserving collision.

An interesting case is **(52)** which appears to depend neither on frequency nor temperature. As the dimension of a crystal is reduced into the nanometer regime, it becomes comparable to the wavelengths of phonons low in energy. Such phonons will be scattered strongly by the surface. The same mechanism is operative in macroscopic polycrystals with nanometer crystalline domains. High frequency phonons usually possess short mean-free-paths l_{Ph} as they are scattered quickly by impurities for instance. Thus, they rarely reach the surface or a new domain of a crystal which renders them independent of grain boundary scattering. Therefore in most systems, grain boundary scattering is limited to phonons of low frequencies although there is no natural limitation. In ultra-pure single crystals at $T << \theta_D$, grain boundary scattering is the dominant resistive process for all phonon modes. In this particular case, **(43)** simplifies to

$$\textbf{(54)} \qquad \kappa_L = \frac{1}{3} C_V v_S L$$

with the specific heat capacity C_V.

In all other cases, we still need to evaluate the integrals in **(43)** which often asks for iterative methods. To do so, **(50)** to (**53)** are substituted into **(44)** to (**46)** on which **(43)** is evaluated for separate temperature regimes. Due to the large temperature dependence, some of the terms become close to zero in specific temperature regimes on which they can be neglected to simplify the integration.

The most obvious case is the low temperature regime of only a few Kelvin. Since T is low and only low frequency phonons may be excited, we can readily apply **(54)** regardless of the purity of the crystal. The temperature dependence of κ_L will be that of C_V which according to Debye's theory goes as T^3. The maximum is expected roughly at 1/20 θ_D.[11] The magnitude of the maximum (but not the shape of the curve) depends on the purity of the crystal.

In the case of high temperatures ($T >> \theta_D$), it is $\Theta << 1$ and $\frac{\Theta^4 \exp[\Theta]}{(\exp[\Theta]-1)^2} \approx 1$.This is the regime where *U*-processes are dominant and it can be shown on using this approximation that κ_L goes as T^{-1} unless crystals are ultra-pure. In the latter case, the maximum at roughly 1/20 θ_D is located much higher and the decrease in κ_L is steeper following a T^{-2}-dependence.

The intermediate range with 1/20 $\theta_D < T < \theta_D$ is governed by the superposition of different scattering mechanisms with similar importance which makes it very hard to obtain reliable predictions. One often finds a curve following $T^{-3/2}$. A typical $\kappa_L(T)$ behaviour based on the predictions of the Debye-Callaway-model is depicted in **Figure 5**.

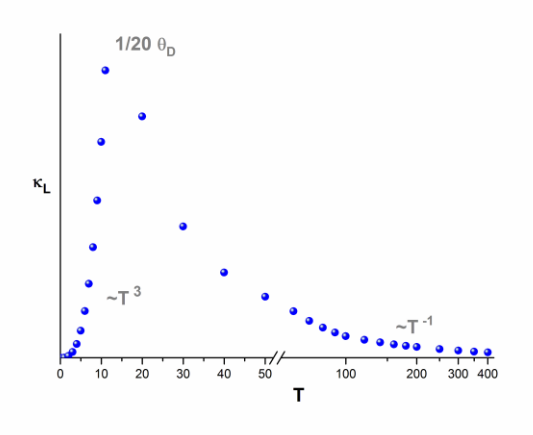

Figure A-5: Temperature dependence of the lattice thermal conductivity (κ_L) as predicted by the Debye-Callaway model. At low T, κ_L increases as T^3 towards a maximum at roughly 5 % of the Debye temperature θ_D. Beyond the maximum, κ_L decreases as $T^{-3/2}$ until the slope resembles T^{-1} near room temperature.

On recalling that the primary purpose at the beginning of this chapter has been the expression of zT by fundamental physical parameters, one may ask if such a complex and hardly practical expression for κ_L is really necessary. The answer depends strongly on the nature of the conductor or precisely on the ratio of electronic thermal conductivity as defined by **(36)** to lattice thermal conductivity (κ_e) as defined by **(43)**. The sum of the two is the total κ as it appears in **(1)**. For metals, ρ is small and κ_e will be much greater than κ_l so the latter can be neglected. For insulators, this situation is reversed.

Since most thermoelectrically interesting systems are small-bandgap semiconductors, κ_L and κ_e are of comparable magnitude and both expressions have to be considered.

Indeed, most of the great improvements in thermoelectric material design in the recent years have been due to manipulations of κ_L so knowledge of the Debye-Callaway-model is important.

Strategies to improve zT

General considerations

The expressions for the transport coefficients derived from fundamental principles enable us to systematically tailor novel thermoelectric materials with improved zT. One intriguing practical approach to manipulate the individual parameters in zT is using nanostructured materials. I stress that the quest for better thermoelectric materials is certainly not limited to the advances in nanotechnology. Many fascinating bulk materials have been developed since the 1950s which have substantially deepened our understanding of thermoelectric processes. However, in terms of chemical composition and crystal structure these bulk materials become increasingly complex. Simple and thus cost-effective materials have been tested to a great extend many decades ago. Chances are small that a relatively simple compound like Bi_2Te_3 with outstanding thermoelectric properties is yet to be discovered.

On the other hand, introducing nanostructures into a well-known material can entirely change the physical properties of the system. Atoms on the surface behave significantly different from their counterparts deep inside the crystal. In large crystals, the ratio of surface atoms to the crystal's volume is so small that their contribution to the physics of the system may be neglected. As the size of the crystal decreases, the volume shrinks quickly whereas the surface area is only slowly depleted. Thus, the special properties of the surface atoms contribute significantly to the physics of the crystal. In crystals of only a few nanometers in diameter, almost every second atom is located at the surface. The physics of such crystals is dominated by the surface chemistry of the material. This may include dangling bonds, adsorbates, defects and others.

A dramatic physical effect occurs when at least one dimension of the crystal is on the order of the wavelength of a particle inside the crystal. In such a case, the particle is said to be confined by the limited dimensions of the crystal and the laws of classical physics may no longer be applicable. Instead, a quantum mechanical treatment following the basic conceptions of Schroedinger's *particle-in-a-box* will be required. The term "particle" may be everything from phonons over electrons and holes to electron-hole-pairs, the so-called excitons. Especially the last type of particles can possess wavelengths of up to 100 nm so that confinement effects are straightforward to achieve. An important consequence of quantum confinement is a dramatic alteration in the density of states from a continuous distribution in 3D- to discrete levels with large spikes in 0D-systems.[12] From **(34)** we know that thermopower depends on the density of states so it is easy to see that reducing the dimensions of a system will force a change in zT. It was exactly this idea by Hicks and Dresselhaus in 1993 which revived the interest in thermoelectrics and let many researchers turn towards nanostructures.[13,14] Ironically, not a single one of the novel nanostructured thermoelectric materials with improved zT gained its superior properties from quantum confinement effects. Although we know today that the idea of the authors (regardless of its brilliance) might never go to plan, the true achievement of Hicks and Dresselhaus is the great recognition of the thermoelectric society for nanostructured research and the numerous discoveries evolving from combining these formerly separated fields. Present thermoelectric research is dominated by nanotechnology. On using the expressions for the transport coefficients derived from the BTE, we shall now see how and why.

I stress once again that the validity of the BTE for nanostructured systems is at least questionable since we are effectively applying Newton's classical laws of motion onto systems where quantum confinement effects may well be present. Hence, quantitative results should be treated with care.

Reducing the lattice thermal conductivity (κ_L) by nanostructures

From **(50)** to (**53)** we know that resistance to heat transport of a crystal's lattice is mainly due to *U*-processes, impurity scattering and grain boundary scattering. If we consider thermoelectric materials for applications under ambient conditions (T = 300 K), we can expect that *U*-processes occur frequently and provide a natural upper limit for thermal conductivity. From the introduction on the material requirements for thermoelectric device building we learnt that doped semiconductors are preferable since two materials with great excess of either holes or electrons are required. Thus, in a common thermoelectric material we can expect a large concentration of impurities. Recall that impurity scattering is very effective for high frequency phonons but poorly scatters phonons from the low energy regime of the dispersion spectrum. In contrast, this is the domain of grain boundary scattering. Since the probability of grain boundary scattering in a crystal scales with its surface-to-volume ratio, nanostructures are highly effective in scattering low-frequency phonons. In heavily doped nanostructures at 300 K we encounter an effective scattering mechanism for every phonon mode due to the superposition of the individual effects.

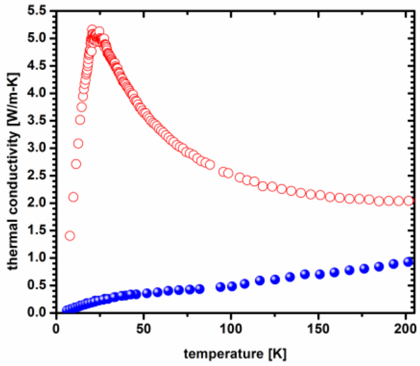

Figure A-6: Comparison of the temperature dependence of the total thermal conductivities of bulk (**open circles**) and nanostructured materials (**closed circles**).

Figure 6 displays the effect on κ by nanostructuring an otherwise identical material. The shape of the macroscopic bulk sample resembles the curve predicted by the Debye-Callaway-model as depicted in **Figure 5**. Recall that the maximum is due to the onset of *U*-processes which counteract the T^3 power law of the specific heat of phonons at low temperatures. In contrast, the nanostructured sample with 10 nm grain sizes does not show a maximum at all. κ is seen to increase monotonously but on a very low level. This is the result of effective phonon scattering over the entire dispersion spectrum but with an emphasis on the low-frequency region relevant at low temperatures where the effect of nanostructuring is most prominent. Further we see that, although less dominant, the effect is still significantly present at higher temperatures. This is because materials bearing considerable amounts of impurities transmit most of their heat by low-frequency phonons.

To be precise, not every phonon scattering at grain boundaries is necessarily resistive to heat transport. It is important to distinguish between diffusive and specular scattering. The former is non-conserving in momentum whereas the latter may be compared to the perfect reflection of light by a mirror and conserves momentum. Only if scattering at grain boundaries is entirely diffusive, **(52)** applies and the relaxation time approaches the so-called *Casimir limit*.[15] Where the experimental determination of the diffusive-to-specular-scattering-rate is difficult, there is evidence that increasing the surface roughness of a material increases the probability for diffusive grain boundary scattering.[16] This may be achieved by introducing nanometer small features on the surface of a sample or grain.

Another additional but rarely explored mechanism of reducing κ_l by nanostructuring is lowering the Debye temperature. This way, *U*-processes have higher probability at low temperatures and the phonon frequencies with high *U*-process probability are excited more quickly. There is a recent theoretical prediction that materials with large surface-to-volume ratios should possess reduced Debye temperatures.[17] This is experimentally confirmed in this work in **Chapter E**. One would expect the maximum in κ_l to shift to lower temperatures as the Debye temperature is reduced and *U*-processes counteract the T^3 law at lower temperatures.

In summary and on remembering **(1)** with $\kappa = \kappa_e + \kappa_l$ and $\kappa_e \approx \kappa_l$ for small band gap semiconductors, due to a reduction in κ_l of 50 % as in **Figure 6** we can expect an improvement in zT to amount to roughly 25 % around room temperature. This has been confirmed by experiment.[18]

It is difficult to imagine how reductions of κ_l alone should lead to enhancements in zT of 300 % as required for broad market applications. This is especially true as most of the thermoelectric materials successful in the bulk state already show relatively low lattice thermal conductivities. Another problem is the magnitude of the electronic thermal conductivity. As long as κ_e is equal or even greater than κ_l, every reduction in κ_l will have only modest effects on zT. This brings us to the discussion of possible reductions in κ_e.

Reducing the electronic thermal conductivity (κ_e) by nanostructures

From **(36)** we know that there is a direct interdependence between κ_e and the electric conductivity σ, called the Wiedemann-Franz law. According to this, any reduction in κ_e should force an equal reduction in σ in which case no gain in zT is to be expected. However, what is often underestimated is the flexible nature of the Lorenz number L in the Wiedemann-Franz law. As discussed in **(36)** it is far from being a constant. What we have already seen numerically has been confirmed by experiment: L increases with increasing carrier concentration.[19] To gauge the magnitude of L for nondegenerate semiconductors, we need to justify a value for the scattering parameter *s*. **Table 1** lists common scattering mechanisms and their contribution to power law scattering (**32)** in terms of *s*:

Scattering mechanism	Exponent *s*
Acoustic phonon	- 1/2
Ionized Impurity (weakly screened)	+ 3/2
Ionized Impurity (strongly screened)	-1/2
Neutral impurity	0
Piezoelectric	+ 1/2

Table A-1

It is evident that for nondegenerate semiconductors where **(32)** applies, L can be 0.6 to 1.2 L_0 if L_0 is the original Lorenz number for metals 2.45 * 10^{-8} V^2K^{-2} as it appears in **(37)**. To maximize zT, one would want L and hence *s* to be as small as possible to minimize electronic heat conduction whilst maintaining high electric conductivity. Unfortunately, *s* usually increases on introducing nanostructures which will have a negative effect on zT.[20]

Nonetheless, the idea of reducing L to increase zT is receiving growing attention. Mahan and Sofo worked out that materials with a Dirac delta function like density of states should have values for L and κ_e close to zero.[21] As mentioned earlier, such a situation is found in 0D-systems, where quantization of carrier energy forces the formation of discrete energy levels and hence abrupt changes in the density of states in energy space. This idea has obvious similarities to Hicks and Dresselhaus's work only that they aimed at increasing S rather than decreasing κ_e. I have considerable doubts concerning the overall effect of the Mahan-Sofo approach. If we consider 0D-systems characterized by the *particle-in-a-box* formalism, it is essential to assume potential walls of infinite height. Only then, the energy levels are entirely discrete and the density of states distribution in energy is described by the Dirac delta function. Provided one of these delta functions is located close to E_F, we should expect a κ_e close to zero on following Mahan and Sofo. However, a system with infinite potential walls is a perfect insulator to its environment, so σ would be zero and κ_e should be zero regardless of the magnitude of L. If we lower the potential barriers to some finite height and/or allow tunneling transport, σ should increase above zero and the magnitude of L becomes important for zT. However, as part of the electron wave function is allowed to spread out over the limits of the box, the pure *particle-in-the-box* model does not apply anymore and the former delta function describing the distribution of density of states will broaden. According to Mahan and Sofo, this will increase L. Whether these effects precisely cancel each other or if there is an optimum for which we may expect a substantial increase in zT remains to be shown.

The discussion about electric transport inevitably brings us to the manipulation of the electric conductivity by nanostructures.

Increasing the electric conductivity (σ) by nanostructures

The surprising result of **(29)** and (**30)** is that on increasing the scattering parameter *s*, the mobility (μ) and hence σ is seen to increase. Thus, one might expect nanostructured materials to show better electric transport than their bulk equivalents. In reality, this is practically never the case. Mainly, this is due to the fact that electric transport in nanostructures is dominated by scattering of charge carriers at grain boundaries.[22] Seto has developed a mathematical description to model the effective mobility due to grain boundary scattering.[23] According to him, it is

$$\textbf{(55)} \qquad \mu_{GB} = Le \cdot \left(\frac{1}{2\pi m^* k_B T_L} \right)^{1/2} \exp\left[-\frac{E_b}{k_B T_L} \right]$$

with L being the length of the grain and E_b a potential barrier associated with an activation energy required to lift the electron over the grain boundary. To gauge the magnitude of a typical μ_{GB}, let L = 100 nm, m^* = m_0, T_L = 300 K and E_B = 2 k_BT_L which yields μ_{GB} = 100 cm^{2}V^{-1}s^{-1}. If the mobilities associated with other carrier scattering mechanisms (acoustic phonon and/or ionized impurity scattering, for instance) are much greater than μ_{GB}, the total mobility will be approximately equal to μ_{GB}. For typical thermoelectric materials like PbTe (μ_{el} = ~ 1000 cm^{2}V^{-1}s^{-1})[24] and Bi_2Te_3 (μ_{el} = ~ 500 cm^{2}V^{-1}s^{-1})[25] this is the case. If their magnitudes are comparable we need to apply Matthiessen's rule (**(47)**) but should bear in mind that it only applies if all scattering parameters are equal.

Thus, depending on the magnitude of the individual mobilities associated with the scattering mechanisms in a system, the nanostructured σ may be much less, equal or even greater than in the bulk material. For materials with high bulk mobilities, we should expect a significant drop in σ on introducing a nanostructure. Since most thermoelectric materials are highly doped, there is usually a large degree of ionized impurity scattering which leads to low mobilities. For such materials we can hope for a barely noticeable effect on σ by nanostructuring.

Some groups even reported a slight increase in σ as they compared nanostructured with bulk samples.[18,26] Where this can in principal be justified by the BTE based expression in **(30)**, at least in one case the increase was so drastic that an additional mechanism must have been operative which has not yet been described in sufficient detail.

If any, we can conclude that the impact of nanostructuring on σ is so complex that even semi-quantitative predictions are currently out of reach. In this respect, I would like to stress once again the limits of applicability of the BTE. For a fully quantitative description of electron transport in nanostructures, the derivation of quantum mechanical equivalents of the transport **(17)** and (**20)** and the transport coefficients therein is required. This is not only mathematically challenging but also requires detailed knowledge of the chemical environment of each grain boundary. Both tasks remain to be solved.

Increasing the thermopower (S) by nanostructures

According to **(34)** and (**38)**, S depends on the effective density of states (N_C), the charge carrier concentration (n) and the scattering parameter (*s*). As discussed earlier, the dependence on *s* is almost negligible for nondegenerate semiconductors but can be of high importance if n $\approx N_C$ which is the case for degenerate semiconductors. Since nanostructures are seen to increase *s* one can expect a substantial improvement in S. Again, typical values for *s* may be found in **Table 1**. Heremans *et al.* showed that introducing nanostructures into PbTe raised *s* from 0.5 to 1.0 which in the case of nondegenerate semiconductors should result in a 25 % increase in S.[20] Since zT scales as S^2 this is an important result.

The significance of N_C for the magnitude of S has been stressed earlier. What we are interested in is a high density of states *in the vicinity of* E_F (thus the term "effective"). For individual 0-D quantum dots this can be achieved by applying an appropriate gate voltage to the quantum dot to tune E_F towards an energy where a discrete energy level of the system is located. Due to the Dirac delta function like density of states, N_C would be infinite at this point. Similar to the comment in the section on the electronic thermal conductivity, this situation is purely theoretical because it prohibits any electric interaction of the quantum dot with the environment. As soon as a measurement is taken, the potential walls must be finite (or we would measure no current) and the distribution function broadens.

Despite this unrealistic scenario, the general concept remains intact: a good thermoelectric material must possess a large effective density of states. Weak electric coupling of quantum dots allows for some electric transport through the array of quantum dots but retains a narrow distribution of the density of states. Wang *et al.* applied this concept to enhance S in PbSe by more than 50 %.[27] It must be emphasized that all attempts to increase N_C and hence S by electron confinement effects are accompanied by a decrease in σ which is mainly due to a reduced mobility. This decrease usually outweighs the increase in S so that arrays of weakly coupled quantum dot arrays have not shown enhanced zT values. Nonetheless, they provided an important proof of principle.

The reciprocal dependence of S on *n* forms the basis for one of the greatest challenges in every thermoelectric material design. Because of **(29)**, decreasing *n* not only increases S but simultaneously increases ρ which counteracts the beneficial effect on zT. The fact that zT scales as $S^2\sigma$ can only partially compensate this effect since σ is directly proportional to *n* whereas S scales as ln(1/*n*). It is this unbreakable interdependence which, despite great alterations in either S or σ, often leads to very similar values of $S^2\sigma$ (also referred to as *the* *power factor*) and thus zT. Increasing either S or σ and keeping the other just constant is therefore a huge (yet rewarding) challenge in terms of enhancing zT. In the previous passage, the emphasis was put on maximizing the mobility rather than *n*. To find a similar parameter for maximizing S without decreasing *n* greatly, let us consider a somewhat more phenomenological description of S:

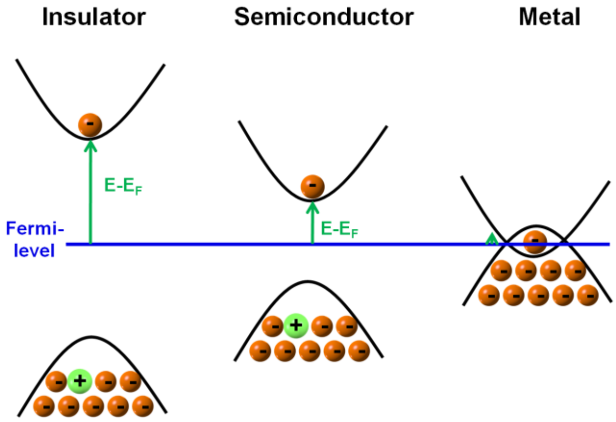

Figure A-7: Simplified band structures and positions of the Fermi level in insulators, semiconductors and metals. The energy E-E$_F$ of a carrier in the upper band (the conduction band) can be understood as the kinetic energy of the carrier.

Figure 7 represents the simplified bandstructures of the three main classes of materials: Insulators, semiconductors and metals. In the case of pure and non-doped materials, the Fermi-level is located at equal distance to the two band edges, that is, above the populated valence band and below the empty conduction band. In the special case of metals, the two bands overlap and E_F is located inside the bands. On exciting an electron from the valence band with an appropriate quantum of energy, one can lift this electron into the empty conduction band where it can contribute to the total current in the conductor. From **(26)** we know that an electric current J will lead to a heat current J_Q scaled by the Peltier coefficient π of the material. How much heat is carried by the single charge carrier populating the conduction band in **(7)**? On recalling **(8)**, we have defined the total energy of a carrier by the sum of its potential $E_{C0}(\mathbf{r})$ and kinetic energy $E(\mathbf{p})$ minus the quasi-Fermi level $F_n(\mathbf{r})$. Since E_{C0} and F_n are independent of momentum, the difference in total energy due to this excitation must be due to a change in kinetic energy $E(\mathbf{p})$ of the carrier which, according to **(16)**, is associated with heat flow. From **(7)** it is apparent that the heat carried by the excited electron scales with the distance of the conduction band edge from the position of the Fermi level. Thus, a lot of heat is carried by individual excited electrons in insulators where the heat content of individual carriers in metals is low. It follows that insulators possess large Peltier coefficients, and, due to the Kelvin relation (**(35)**), large thermopower values, where these coefficients are small for metals.

In ordinary materials we are likely to deal with a large number of charge carriers which are prone to distribution in momentum. Therefore, rather than asking for the kinetic energy of an individual charge carrier, we must consider the *average* kinetic energy per charge carrier of the system. From the discussion above, we saw that this is equivalent to the average total energy of charge carriers *with respect to the Fermi level*. We have arrived at an important definition of thermopower:

"*Thermopower is the average total energy with respect to the Fermi level per charge carrier*."

or

$$S \propto \frac{E - E_F}{n} \tag{56}$$

The term "per charge carrier" simply includes the reciprocal dependence on *n* as, with a given total energy of the system, thermopower decreases with increasing *n* which we already knew from **(34)**. On recalling the initial quest to identify a quantity other than *n* with which one can manipulate the thermopower, we now know that we must aim at increasing the average energy per charge carrier in the system to increase S and thus zT. A trivial way to do this is by increasing the band gap of a conductor. Of course, this will strongly decrease *n* and is not desired.

We may then think about altering the position of the Fermi level by doping. Introducing an n-type (p-type) dopant lifts the Fermi level towards the conduction band (valence band), respectively. Where this increases $E\text{-}E_F$ with respect to one band edge, it simultaneously decreases the average energy with respect to the other band edge. If the band gap and doping level are sufficiently large, the $E\text{-}E_F$ values with respect to the two band edges are so dissimilar that the type of conductance will be purely n- or p-type depending on which band edge is closer to E_F. This will lead to the generation of a lot of electrons (holes) in the conduction band (valence band), respectively, which increases *n* strongly. In the extreme case, we have $n \approx N_C$ and thus a degenerate semiconductor. In such a case, we may expect E_F to be positioned *at* or *inside* the band responsible for conduction so that the conductor is almost metallic. This leads to a situation as depicted in **Figure 8**. Of course, S cannot be large since $E\text{-}E_F$ is small.

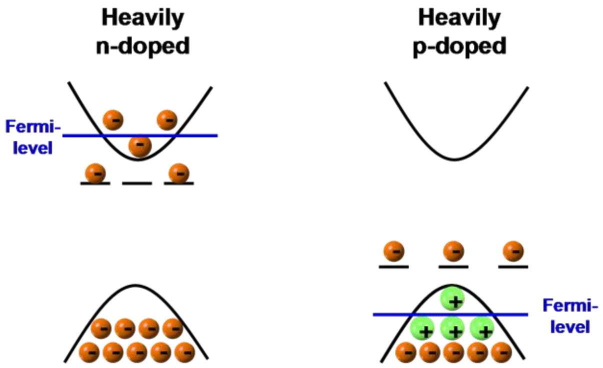

Figure A-8: Simplified band structures of heavily n- and p-doped semiconductors. The Fermi level resides at or even inside the conduction band (for n-type materials) or the valence band (for p-type materials).

Since E_F is positioned in an area with a large N_C, at non-zero temperatures there will always be a significant amount of charge carriers with $E < E_F$ and $E > E_F$ which all contribute to the total current in the conductor. Because of **(56)**, these two classes of charge carriers possess thermopower values of opposite sign. Summing over all charge carriers to yield the total thermopower of the system will result in partial cancellation of S as the charge carriers from below E_F counteract those from above. I conclude that in the special case of degenerate semiconductors, the total thermopower of the system would be greater if the carriers from one side of E_F would be immobilized. Then, only charge carriers of equal sign in thermopower will conduct and their contribution to the total thermopower is purely constructive. This idea forms the basis for the concept of *potential barrier energy filtering* developed by Nolas and co-workers as a novel concept to increase S and hopefully zT.[28]

The concept of potential barrier energy filtering

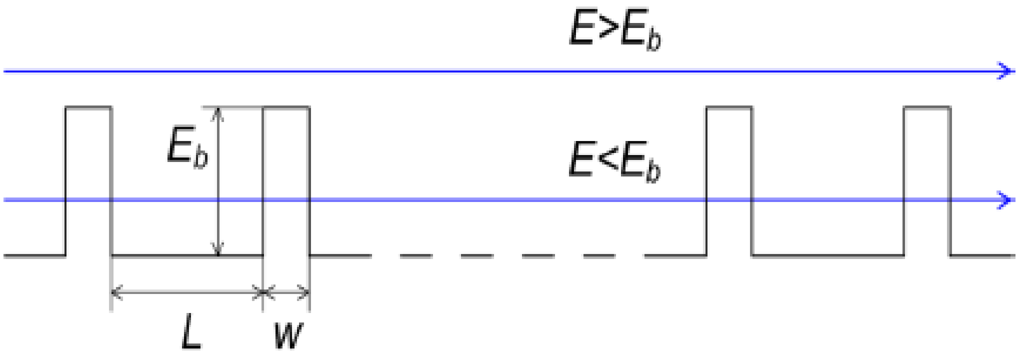

Figure A-9: Simplified energy-position diagram of two periodically reoccurring materials with different potentials for charge-carrier transport. The material with low potential in region L acts as a potential well. The material with large potential in region w acts as a barrier of height E_b to the well. A charge-carrier with $E>E_b$ is unaffected in its transport behaviour by the barrier whereas carriers with $E<E_b$ are trapped inside the well if tunnelling can be ignored.

Consider a material with an energy-space profile as depicted in **Figure 9**. We can distinguish two different plateaus in energy, namely E and ($E+E_b$), where E_b is the energetic height of a potential barrier. In terms of space, we have two different regions L and w, with the former being the length between two potential barriers and the latter being the spatial width of the barrier. If we consider carrier transport across this system, E must be equal to ($E_{C0}-E_F$) on using the terms defined in **(6)**. Every carrier with this amount of energy will be able to travel within L but not across w because of the additional potential E_b. Thus, only carriers with kinetic energy $E(\mathbf{p}) \geq (E+E_b)$ will contribute to the total current in the system if we neglect the possibility of tunnelling. From **(56)** we know that this will increase the total thermopower of the system because the average total energy per carrier has been increased.

In the special case of degenerate semiconductors where we have a large density of states above *and* below the Fermi level, we are interested in immobilizing the carriers on one side of E_F to increase S. If we set $E_b = k_BT$ then the majority of carriers from below E_F cannot contribute to the total current on mere thermal excitation. From **(55)** we can even estimate the magnitude of the total mobility in such a system if we assume transport across the barrier to be the rate-limiting step. On letting L = 100 nm, $m^* = m_0$ and T = 300 K, we obtain $\mu = 370\ cm^2V^{-1}s^{-1}$, which is not significantly smaller than the bulk mobility in typical thermoelectric materials like Bi_2Te_3 or PbTe. In fact, Vashaee and Shakouri showed that with respect to optimizing zT (and not just S), E_b should ideally be on the order of 0 – 4 times k_BT depending on the position of E_F.[29]

Popescu *et al.* developed a full mathematical model based on the BTE to predict the effect of the parameters L, w and E_b on the thermoelectric power factor $S^2\sigma$ of PbTe.[28] They showed that

1. L should not be smaller than 200 nm,
2. E_b should not be greater than 100 meV,
3. the effect of w was practically insignificant.

Whether these results can be generalized, remains to be seen. Most importantly, the authors demonstrated that on choosing appropriate parameters one can actually increase $S^2\sigma$ and not just S. This is in contrast to the strategies discussed above which aimed at improving one particular parameter neglecting the (possibly counteracting) effect on other transport coefficients. This leads to the ultimate question how to improve zT with nanostructures.

Increasing the thermoelectric figure of merit (zT) by nanostructures

On substituting **(29)**, (**34)** and (**36)** into **(1)** we obtain

$$\textbf{(57)} \qquad zT = \frac{\left[-\ln\frac{N_C}{n} - (s+5/2)\right]^2}{\left[ß - \frac{N_C}{n}\right]^{-1} + (s+5/2)}$$

with *ß* being the Chasmar-Stratton-factor defined as:

$$ß = \left(\frac{k_B}{e}\right)^2 \frac{T}{\kappa_L} \cdot 2e\mu \left(\frac{2\pi m^* k_B T}{h^2}\right)^{3/2} .^{30}$$

Where we can gain a qualitative understanding of the dependence of zT on material specific parameters like N_C/n, µ and m*, **(57)** is of little practical use for quantitative predictions. First of all, we still need to include a quantitative expression for κ_L which can be quite complicated as we have seen when discussing the Debye-Callaway-model. Further, on letting $\frac{d(zT)}{d\left(\ln\frac{N_C}{n}\right)} = 0$ we may find an optimal doping level for which zT has a maximum. It turns out that for most materials this applies for $n \approx N_C$, the case of a degenerate semiconductor. Unfortunately, **(57)** only holds true for nondegenerate semiconductors. (Remember that $n \ll N_C$ was the precondition to apply **(32)**.) Therefore, it is not self-consistent and should be handled with care.

In the case of a fully degenerate semiconductor one may use approximations of the type we applied for the thermopower in **(38)**. However, the thus derived solutions for zT are even more complicated and often iterative.

Thus, the model developed by Nolas and co-workers with quantitative predictions for the effect of potential barrier energy filtering onto $S^2\sigma$ is an important achievement. To be precise, we would have to include the effect onto κ_L as well which may very well depend on the spatial width of the potential barrier. This task remains to be solved.

The phonon-glass electron-crystal concept

Another concept to improve zT itself is by designing materials which discriminate in their scattering behavior between phonons and charge carriers. Since the mean free path of phonons is often significantly greater than that of charge carriers, in a polycrystalline material there is a size range for the average crystal grain in which strong interactions with phonons but only weak interactions with charge carriers occur. Precisely, this is the case when the mean free path of the phonon in the bulk material is larger than the average grain size which in turn is larger than the mean free path of the charge carriers in the bulk. According to Slack, such a material would show the transport properties of a glass with respect to phonons but that of a crystal with respect to electrons (or holes). Consequently, it is termed a phonon-glass electron-crystal (PGEC) material.[31] In contrast to crystals, glasses possess no long-range order which renders them poorly conducting for all types of carriers. In a PGEC material, the ratio of charge carrier transport to phonon transport is thus expected to be significantly greater than one. We have $\sigma/\kappa_L > 1$ and, provided the Wiedemann-Franz law holds and thermopower is not affected by the reduced grain sizes, $zT_{PGEC} > zT_{bulk}$. One often finds that this is the case if the grain sizes are properly chosen. **Chapters B**, **C** and **D** are subject to this effect.

With this, I will conclude the theoretical discussion of thermoelectric material design and turn towards practical considerations. So far, we have seen the impact of nanostructures onto various transport coefficients and the pathways provided for improvements in thermoelectric efficiencies. But how can we make such structures? Which are the degrees of freedom to manipulate the parameters discussed above? This is the domain of chemistry or, in this case, of colloidal chemistry.

Materials and methods

The colloidal chemistry approach to nanostructures

All nanostructures described in this work have been prepared by ligand-supported colloidal chemistry in organic solvents. The term “ligand” refers to a long-chained, carbon-based molecule with at least one coordinating functional group. Typical examples are 1-dodecanethiol ($C_{12}H_{26}S$), oleic acid ($C_{18}H_{34}O_2$) or oleylamine ($C_{18}H_{37}N$). “Organic solvents” refer to carbon-based liquids with high boiling points like diphenylether, oleylamine or trioctylphosphine.

The inorganic components are provided by the acetates of their metal salts, e.g. Bi(acetate)$_3$, Sb(acetate)$_3$ or Pb(acetate)$_2$*3H_2O or, in the case of tellurium and selenium, by dissolving the elements in oxygen-free trioctylphosphine. These species will be referred to in the following as “precursors”.

When the dissolved precursors are heated in the presence of suitable ligands, small atomic clusters may form which are referred to as “nuclei”. As they consist of only a few atoms, these nuclei are less stable than the dissolved single-atomic precursors and a lot less stable than larger clusters of the same material. The former is due to the solvation enthalpy provided by the solvent and/or ligand which is most effective for single-atomic species. In small clusters, not all atoms can equally interact with the solvent and the average enthalpy of solvation released per atom is less than that of the precursors. In addition, a considerable amount of entropy is lost in the system on cluster formation. With

$$\Delta G = \Delta H - T\Delta S \tag{58}$$

the Gibbs free energy (ΔG) can only become negative when the release in enthalpy (ΔH) is large enough to compensate the loss in entropy (ΔS). One can expect $\Delta H \geq 0$ on forming small clusters from dissolved single ions, so ΔG will be positive which designates a thermodynamically disfavored process.

In continuation, the latter is the result of the lattice enthalpy released as a sufficient number of atoms is available to form a periodic lattice – in the following referred to as “crystal”. Provided the surface of the crystal is small compared to its volume, it is $\Delta H << 0$ and $\Delta G < 0$. If the solvation of precursors was weak and/or the number of nuclei formed was small compared to the amount of precursor, the size of the crystals can become very large driven by the reduction of the surface-to-volume ratio and thus the energy per crystal. This can be prevented by the presence of ligands with suitable binding sites to attach to the crystals' surfaces and reduce the energy of their surface atoms. Once the Gibbs free energy of the solvated single ionic precursor is equal to the Gibbs free energy of the crystals' lattices and their (ligand stabilized) surface atoms, thermodynamic equilibrium has been reached and crystal growth will stop. Thus, applying ligands with better stabilization properties will lead to smaller crystals. In practice, crystal sizes between 3 to several tens of nanometers are straight forward to achieve.

From these simple thermodynamic considerations it is easy to see that the process of nucleation is the rate-limiting step in nanocrystal growth. The question whether or not crystal growth will occur is linked to the height of the energy barrier associated with the formation of the nuclei. Consequently for every given system, there is a threshold temperature below which no nucleation and hence no crystal growth will occur because the mean thermal energy of the molecules is smaller than the height of the activation barrier.

To lower the barrier, one may apply strongly coordinating ligands to stabilize the nuclei or provide an alternative low-energy pathway for nucleation. The latter may be the surface of a different crystalline material serving as active nucleation sites.

To derive a quantitative expression for the height of the activation barrier, consider fundamental thermodynamic principles:

Following the discussion from above, the change in free energy on adding n_i precursor ions from the solution to a cluster of radius R and surface free energy γ leading to a change in surface area ΔA_i is

$$\textbf{(59)} \qquad \Delta G_i = -n_i k_B T \ln\left(\frac{c}{c_s}\right) + \gamma \Delta A_i$$

The term c_s (the saturation concentration) should be understood as an analogon to the bulk saturation pressure for vapors, which is the constant pressure at the liquid/vapor interface in equilibrium. Thus, c_s is the constant concentration of the precursor in solution at the bulk solid/liquid interface in equilibrium. We see that due to the surface free energy (or surface tension), for small crystals of large surface-to-volume ratios to be in equilibrium ($\Delta G = 0$), the actual concentration in the vicinity of the crystal must be larger than the saturation concentration. In other words, it is required that

$$\textbf{(60)} \qquad n_i k_B T \ln\left(\frac{c}{c_s}\right) = \gamma \Delta A_i$$

Mind that because of

$$\textbf{(61)} \qquad \Delta A_i = \frac{2V_M}{R_i}$$

with V_M being the volume of a precursor-ion, the value of c for which **(60)** is valid depends on the size of the crystal. With increasing R, a smaller value of c is required to establish equilibrium meaning that the precursor concentration in the vicinity of smaller particles is greater than in that of larger particles. This leads to a concentration gradient driven net-flow of precursor from smaller particles to larger particles. Eventually this results in the sacrificial dissolution of smaller particles. This process is called *Ostwald ripening*.

For n_i precursor ions of volume V_M forming spherical crystals, it is

$$\textbf{(62)} \qquad \frac{4\pi}{3} R_i^3 = n_i V_M \,.$$

With **(59)**, we have

$$\textbf{(63)} \qquad \Delta G = -\frac{4\pi}{3}\frac{R^3}{V_M} k_B T \ln\left(\frac{c}{c_s}\right) + 4\pi R^2 \gamma$$

for the total change in Gibbs free energy.

When $c > c_s$ and R is sufficiently large, ΔG becomes negative and growth is thermodynamically favored. However, when the magnitude of R is below a critical value R_c, the right-hand term of **(63)** will dominate and ΔG becomes positive resulting in a decrease in R until $R = 0$. This is the dissolution of the crystal. Hence, ΔG possesses a maximum at R_c which can be determined on using

$$\textbf{(64)} \qquad \frac{dG}{dR} = -4\pi \frac{R_c^2}{V_M} k_B T \ln\left(\frac{c}{c_s}\right) + 8\pi R_c \gamma = 0 \,,$$

so

$$\textbf{(65)} \qquad k_B T \ln\left(\frac{c}{c_s}\right) = \frac{2\gamma V_M}{R_c} \,.$$

This is the *Kelvin equation* for solid-liquid interfaces.

Rearranging **(65)** with respect to R_c and substituting into **(63)** with $R = R_c$ yields

$$\textbf{(66)} \qquad \Delta G_{nuc} = \frac{16\pi}{3} \frac{\gamma^3 V_M{}^2}{\left[k_B T \ln\left(\frac{c}{c_0}\right)\right]^2} .$$

with the height of the activation energy barrier for nucleation ΔG_{nuc}. The surprising result is that ΔG_{nuc} depends on the actual concentration of the precursor. This adds an important degree of freedom for experimentalists:

For crystals to grow from a precursor species in solution, we can distinguish two regimes:

1. $c \geq c_s \exp\left(\frac{2\gamma V_M}{k_B T R_c}\right)$ (the nucleation regime)
2. $c > c_s$ (the growth regime).

The latter is the result of **(60)** stating that as long as $c > c_s$ it is $\Delta A_i > 0$ which is associated with growth. However due to **(61)**, it is $\Delta A_{i+1} < \Delta A_i$ because of $R_{i+1} > R_i$, so the rate of growth is constantly decaying until it terminates at $c = c_s$.

LaMer and Dinegar showed that in order to obtain colloidal crystal solutions of narrow size distribution, it is crucial to strictly separate nucleation and growth in time.[32] If the two regimes overlap, new crystals will evolve whilst already existing crystals continue to grow simultaneously. This results in a distribution in size of the crystals.

From the discussions above, we know that reaction temperature (*T*), ligand stabilization (associated with γ) and precursor concentration (*c*) affect both regimes alike but to different degrees. Thus, on careful manipulation of these parameters it is possible to fulfill the LaMer condition for the synthesis of monodisperse colloidal crystals. Particular emphasis should be put on the nucleation conditions. Only when nucleation is initiated *and* terminated practically instantaneously, one may obtain monodisperse colloidal crystals. Since *T* and *c* can be varied easily throughout a reaction procedure and due to **(66),** an ideal nucleation is started by rapidly increasing temperature and precursor concentration of the system. This may be realized by injecting a concentrated precursor solution into a preheated reaction system within the fastest time possible. This technique is referred to as *hot injection*.

To terminate nucleation, *T* should be immediately decreased and the precursor solution be diluted. The latter occurs automatically as the formally concentrated precursor solution is distributed in the reaction system by stirring. Ideally, the time for which $c \geq c_s \exp\left(\frac{2\gamma V_M}{k_B T R_c}\right)$ is almost zero and the nucleation occurs truly instantaneously. Then, the growth rate for every crystal in the system will be exactly the same at any given time t and monodisperse crystals may be obtained provided there are no concentration gradients in the solution.

Lastly, the set of parameters also depends on γ and thus the choice of ligands. Since the effect is complex and difficult to predict, the right choice of the ligand (and its concentration) is mostly made empirically.

To conclude, colloidal chemistry offers the unique opportunity to obtain small crystals with almost zero size distribution. Typical values for R_c may be as low as 1 nm which sets the lower limit for the size of the crystals. On choosing an appropriate ligand, such crystals may show infinite stability in time in solution as they are protected from agglomeration by the repulsive effect of their surface ligands. If the crystal diameter (and thus its weight) is not too large, such ligand-protected, nanometer-sized crystals may float freely in a suitable solvent in which case they are termed *colloidal*. This allows processing this solid state material in solution which can be greatly beneficial for various applications.

For completeness, I would like to add that nanostructures can be obtained by a variety of other methods. For thermoelectric applications in particular, ball-milling of macroscopic ingots has become increasingly popular. The advantage of this method is an excellent control over chemical composition and crystalline phase of the nanomaterial as well as high yields on the kilogram scale. However, if one is interested in controlling size, size distribution and shape of the nanocrystals, colloidal chemistry is greatly favored over ball-milling as in the latter case such a control is barely existent.

Synthesis of core-shell nanostructures

Another unique advantage of colloidal chemistry is the ability to grow a second crystalline phase onto an existing primary phase of a different material. This can be understood as a nucleation of the second material facilitated by the presence of the existing phase which provides low-energy nucleation sites on its surface. This way, γ in **(66)** is decreased so that the activation energy for nucleation of the second material on the surface of the primary phase is lower than for an independent nucleation in free solution. If T and c are chosen appropriately, one can force nucleation of the second phase exclusively on the surface of the primary phase and entirely prevent its separate nucleation in free solution. In most cases, nucleation and growth follows the crystalline direction dictated by the direction of the primary phase. Such a growth is called *epitactic*. Especially if the surface of the primary material consists of just one type of crystalline facets, this mechanism often leads to a closed shell of the second phase covering a core of the primary phase. On choosing materials with appropriate band edges, core-shell nanostructures may resemble an energy profile to charge carrier transport with which the effect of *potential barrier energy filtering* can be investigated.

Nanostructured bulk materials

To facilitate charge carrier transport across macroscopic amounts of individual nanoparticles, the crystals must be compacted to a dense pellet with macroscopic dimensions. Prior to compaction, ligands are removed from the nanoparticles' surfaces and the pure inorganic material is isolated. In continuation, the powder of nanoparticles is loaded into a WC-dye and pressed under high pressure and the aid of a large DC-current to a macroscopic polycrystalline sample with grain sizes of the same dimensions as the individual nanoparticles. This compaction technique is called *spark plasma sintering*. Details may be found in **Chapters B to E**.

Summary of the results and discussion

Since bismuth telluride has been the most extensively studied bulk material for thermoelectric applications, in **Chapter B** a synthesis for macroscopic samples of nanostructured bismuth telluride is developed and the full thermoelectric characterization between 4 K and 300 K presented. The synthesis of 7 nm – 50 nm colloidal bismuth telluride nanoparticles was realized by a one-pot two-step procedure *via* bismuth nanoparticles as a stable intermediate species. After synthesis, the ligand 1-dodecanethiol was exchanged by oleic acid which in turn was removed in an acid-base reaction by exposure to an excess of hydrazine hydrate. For compaction of the resulting nanopowder, a set of parameters for spark plasma sintering (SPS) has been identified for which relative densities of 80 % could be obtained without unwanted growth of nanoparticles during sintering. The compacted nanostructured samples revealed a decrease in σ at room temperature of less than 30 % compared to the bulk value demonstrating that charge carrier scattering is only lightly enhanced. In contrast, κ was decreased by 50-90 % with respect to bulk Bi_2Te_3 depending on the temperature range. Such asymmetric effect on carrier scattering is inherent to materials with phonon-glass electron-crystal properties as discussed above. For the first time, a material of this type has been synthesized by colloidal chemistry. The important step was the successful removal of surface ligands which was neglected in earlier works and greatly decreased σ.[33] With a $\Delta\sigma/\Delta\kappa$ ratio significantly greater one, this material holds great promises for increasing the thermoelectric figure of merit.

An apparent problem of this material has been the accurate control of crystal phases and chemical composition which greatly affects the thermopower. According to Bos *et al.*, bismuth telluride can be described as an infinitely adaptive series of the type $(Bi_2)_m(Bi_2Te_3)_n$ with m and n being integers and (m+n) being a multiple of three. This renders an accurate control of phase and composition inherently difficult. In contrast to high temperature solid state chemistry where the knowledge of a detailed phase diagram may be applied to selectively obtain single phases, this task is complex in low temperature (T = 90 °C) solution-processed chemistry. As a result, thermopower values of the samples presented in **Chapter B** varied and were always a lot lower than for bulk Bi_2Te_3 (-80 μVK^{-1} *vs.* -180 μVK^{-1}). Consequently, an increase in zT could not be achieved for this material. The possibility of the effect of nanostructuring on S is discussed in **Chapter B** and some evidence is provided by the observation of increasing S-values on annealing the samples. However, this effect may also be due to phase changes.

It can be concluded that colloidal chemistry was successfully applied to synthesize a bismuth telluride material with PGEC-properties and thus with the potential to result in increased thermoelectric conversion efficiencies. Due to the large abundance of crystal phases for bismuth telluride, this material is not a good candidate to be synthesized by colloidal chemistry as the control of phase and composition is the main weakness of this procedure.

The results of **Chapter B** have been published in *Advanced Functional Materials* **2009**, 19, 3476-3483.

In **Chapter C**, the work on nanostructured bismuth telluride is extended to the temperature regime of 300 K – 420 K. For $T \geq 420$ K significant grain growth and thus the disintegration of the nanostructure set in. This underlines the importance of SPS for compaction as other conventional methods usually require much higher temperatures than 420 K to arrive at mechanically stable samples. Consequently, the grain sizes presented in this work (~10 nm) are the smallest ever to be reported for macroscopic samples of nanostructured bismuth telluride. SPS is a key technology in this respect.

The most important result of **Chapter C** is the high temperature behaviour of σ which, in contrast to bulk bismuth telluride, increases with increasing T. The band gap of bulk Bi_2Te_3 is so small (0.15 eV) that it behaves like a metal, that is, σ decreases with increasing T. This is especially true for doped Bi_2Te_3. Since σ of the nanostructured samples in this work is not greatly lower than the bulk value, it can be speculated that the band gap should be very similar. The change in shape of $\sigma(T)$ can then be attributed to grain boundary scattering according to **(55)**.

Another interesting result is a significantly increased heat capacity above the rule of Dulong and Petit. This points at a large surface-to-volume ratio present in the compacted nanostructured material. (See section "*Reducing the lattice thermal conductivity (κ_L) by nanostructures*".)

The analysis of κ has been extended beyond room temperature which was possible on changing the measurement technique to the Laserflash method. It turns out that the lattice thermal conductivity is practically independent of temperature. Thus in contrast to bulk materials, *U*-processes do not play a significant role in limiting κ as they are strongly dependent on temperature (see **(50)**). Instead, I believe that the dominant scattering mechanism for phonons in the nanostructured bismuth telluride presented in this chapter is grain boundary scattering.

Further, the effect of porosity in the samples has been taken into account and the affected transport coefficients corrected accordingly. The corrected total thermal conductivity at room temperature coincided well with theoretical predictions and was over 60 % lower than the bulk value. The presence of a pronounced PGEC-effect as observed in **Chapter B** could be confirmed bearing the potential for an increase in zT of 100 %. However, due to the persisting problems with phase and chemical composition control, thermopower remained low and zT could not be increased. Replacing hydrazine hydrate by a solution of ammonia in methanol to remove the surface ligands had no beneficial effect on the thermopower. Still, this replacement is highly recommended since treatment of tellurides with aqueous bases promotes the formation of highly toxic H_2Te which in turn evaporates from the solid and leads to tellurium deficiencies.[34]

The results of **Chapter C** were published in *Thermoelectric Materials - Growth, Properties, Novel Characterization Methods, and Applications*; Tuller, H. L., Baniecki, J. D., Snyder, G. J., Malen, J. A., Eds.; Mater. Res. Soc. Symp. Proc. 1267, Warrendale, PA, **2010**, DD-08-12.

In **Chapter D,** a synthesis for antimony-doped bismuth telluride nanoplatelets is developed and its full thermoelectric characterization presented.

Most importantly, the control of chemical composition and crystal phase could be realized to high accuracy and reproducibility. Apparently, alloying bismuth telluride with antimony telluride to a combined ternary phase greatly favours the formation of the V_2VI_3-phase. The tellurium content in all samples was 60 ± 2 %, whereas in the antimony-free species it was usually smaller than 50 %. Consequently, thermopower values could be controlled to a high degree in these nanostructured $Sb_{2-x}Bi_xTe_3$ samples. The best results were obtained on letting $x = 0.4$ with a thermopower of $+170\ \mu VK^{-1}$. The change in sign for S indicates the strong p-doping effect provided by antimony which is in agreement with observations in bulk samples. Obviously, this effect outweighs the n-doping effect of oxygen replacing tellurium on the crystal surface which readily occurs in practically all tellurides on exposure to air.

The results for κ in **Chapter C** were confirmed in this material in so far as the reduction in lattice contribution was 60 % at room temperature. Due the large concentration of impurities, κ was greatly reduced as compared to the antimony-free species ($0.55\ Wm^{-1}K^{-1}$ *vs.* $0.75\ Wm^{-1}K^{-1}$ at room temperature). This underlines the significance of impurity scattering for thermal transport.

The electric conductivity was found to be only slightly dependent on temperature so that for $T > 370\ K$, the antimony-free material had a greater σ than the $Sb_{2-x}Bi_xTe_3$ material. An interpretation of this result is difficult due to the unknown phase and composition of the parent bismuth telluride compound. Still, σ(T) of nanostructured $Sb_{2-x}Bi_xTe_3$ showed a positive slope indicating a large degree of grain boundary scattering.

In combination, the PGEC-effect found in the parent compound was equally operative in the antimony doped species with a Δσ/Δκ ratio of 1.8 at 420 K. Due to the large thermopower, this was sufficient to result in an increase in zT over state-of-the-art bulk antimony bismuth telluride for $T \geq 400$ K. For the first time, this has been realized by colloidal chemistry.

The results of **Chapter D** have been published in *ACS Nano* **2010**, 4, 4283-4291.

Lastly, the increased specific heat capacity and decreased melting point as found for the parent compound in **Chapter C** could be verified for the antimony species, too. It is worth to note that the temperature activated transport behaviour due to grain boundary scattering renders these nanostructured samples especially effective at elevated temperatures. However, one always has to bear in mind the greatly reduced melting point which limits the temperature range for long-term application.

Thus, **Chapter E** treats a compound with significantly larger bulk melting point (1246 K *vs.* 846 K*)*: Lead telluride (PbTe). It is found that this nanostructured material is stable up to 500 K and, upon alloying with selenium, to 620 K which greatly extends the working temperature range.

For the synthesis of colloidal PbTe nanoparticles, a remarkable shape control was achieved: Adding a small amount of acetic acid (5 µL) to the reaction system changes the shape of the nanoparticles from cubic to octahedral. The key role of acetic acid in this respect has first been suggested by Houtepen *et al.* and may be interpreted in terms of a dipole driven oriented attachment process following a model by Cho *et al.*[35,36]

Briefly, this mechanism takes advantage of the different reactivities and binding energies of the {100}- and {111}-facets in crystals with rocksalt structure (like PbTe). In the early stage of the synthesis, the particles are so small that their shape resembles a sphere which has the lowest surface-to-volume ratio of all objects. Above a certain size, the difference in rate constants for the growth of the three different facets {100}, {110} and {111} leads to a preferential growth in the directions with greatest reactivity. Usually, these are the <110> and <111> directions. Sufficient time permitted, all {110}- and {111}-facets will disappear leaving an object with only {100}-facets: a cube. On choosing the right conditions, these large cubic crystals will be accompanied by smaller crystals due to a non-uniform nucleation stage in time. I believe the role of acetic acid to be the temporal destabilization of surface ligands (oleate/oleic acid) to activate the {100}-facets of the cube for oriented attachment. As the attachment proceeds alongside the <100>-axis, this inevitably initiates the formation of {111}-facets. Since {111}-facets are made entirely of either Pb *or* Te, these facets bear the potential of generating a dipole in the <100>-direction. The dipole accelerates the attachment in this direction until all {100}-facets have been sacrificed for the formation of {111}-facets: the crystal has been converted into an octahedron.

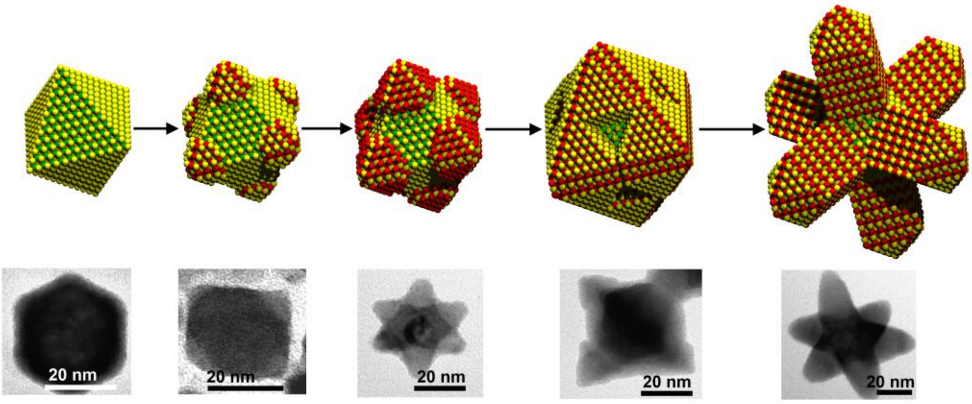

Figure A-10: (Top) Shape evolution of PbTe-PbSe core-shell nanostars with time. Yellow: Pb-atoms, green: Te-atoms and red: selenium atoms. (**Bottom**) Transmission electron microscopy images of the individual stages.

In fact, an octahedron is the crystal structure with the largest dipole alongside the <100>-direction. This has been taken advantage of in **Chapter E** by injecting fresh lead and selenium precursor into a solution of PbTe octahedra. Due to the dipole, the nucleation of PbSe takes place exclusively at the tips of an octahedron, that is, in the direction of the dipole. Eventually, this culminates in the formation of PbTe-PbSe core-shell nanostars as sketched in **Figure 12**. These structures bear the potential of studying the effect of *potential barrier energy filtering* on thermoelectric properties. The results are as follows:

Although great care was taken, the chemisorption of a monolayer of oxygen onto the nanoparticles' surfaces could not be avoided. Where the exact nature of this oxygen containing species is poorly defined, it provides a substantial barrier to charge carrier transport.[37] This resulted in a decrease in σ by over one order of magnitude compared to bulk PbTe. A similar effect was observed for the PbTe-PbSe-species.

The thermopower values of both materials (PbTe and PbTe-PbSe) were increased to 250 % of the bulk value at room temperature. I stress that all samples were phase pure in x-ray diffraction analysis and showed no signs of oxides. The thin layer of (amorphous) oxygen-containing species could only be identified by very careful energy dispersive x-ray spectroscopy and should not amount to more than ~ 2 atomic-%. In other words, rather than investigating a PbTe(O_x) species, the samples in this work comprised of PbTe-PbTe(O_x) core-shell and PbTe-PbSe-PbSe(O_x) core-shell-shell nanoparticles, where the O_x-containing shell in both cases was not significantly thicker than a monolayer. Although of little use for applications in the present form, these two materials demonstrate the feasibility of the *potential barrier energy filtering* concept. It is the first time that core-shell structures have been applied in this way. I pointed out earlier on that a suitable barrier should amount to ~ 4 k_BT. From the σ-values it is clear that the barriers in the present materials were a lot greater which explains why zT could not be increased.

Another important result of this chapter is that the decrease (increase) in σ (S) was *not* due to the small grain sizes in the materials. The argument is as follows: On annealing the PbTe-PbSe-PbSe(O_x) core-shell-shell nanoparticles, a phase change towards a $PbTe_{1-x}Se_x$ alloy was observed. Simultaneously, the star-like structure collapsed to polyhedra of similar size. An immediate increase in σ by two orders of magnitude accompanied by a decrease in S could be observed upon this process. Had electric transport been dominated by grain boundary scattering, the effect of mild annealing should have been barely visible.

I believe that alloying PbTe with selenium moves carrier transport from the valence to the conduction band which is evident from the change in sign in thermopower. Since the oxygen layer is likely to affect predominantly the valence band (the band with tellurium character), n-doping provides an effective way to circumvent the barrier. Therefore, it is not the size of the particles that alters σ and S but the existence of a potential barrier to charge carrier transport. Of course, the former may still be possible if the size is sufficiently small so that the scattering parameter is increased significantly (see **(38)** for degenerate semiconductors). For the $PbTe_{1-x}Se_x$ particles in the present work ($d \approx 100$ nm), this was not the case.

Further results of **Chapter E** included reductions in lattice thermal conductivities of 60 % with respect to the bulk value which is in agreement with the results obtained in **Chapters B-D**. Lastly, I observed again an increase in the specific heat capacity over the saturation level by Dulong and Petit and measured a substantially decreased Debye temperature (θ_D). The significance of θ_D for reducing κ has been discussed when deriving the Debye-Callaway-model for phononic transport.

The results of **C hapter E** will be submitted for publication in the near future.

Chapter B

Synthesis and thermoelectric characterization of Bi_2Te_3 nanoparticles

Manuscript:

Synthesis and thermoelectric characterization of Bi_2Te_3 nanoparticles

By Marcus Scheele[*,1], *Niels Oeschler*[2], *Katrin Meier*[2], *Andreas Kornowski*[1], *Christian Klinke*[1] *and Horst Weller*[1]

[1]*University of Hamburg, Institute for Physical Chemistry, Grindelallee 117, 20146 Hamburg, Germany*

[2]*Max-Planck-Institute for Chemical Physics of Solids, Noethnitzer Strasse 40, 01187 Dresden, Germany*

* To whom correspondence should be addressed

[**] We thank Lucy Mellow and Tobias Vossmeyer for carefully reviewing the manuscript, Prof. Yuri Grin for fruitful discussions, Raul Cardoso for XRD measurements and the "Studienstiftung des Deutschen Volkes" for providing a PhD grant.
Supporting Information is available online from Wiley InterScience or from the author.

We report a novel synthesis for near monodisperse, sub-10-nm Bi_2Te_3 nanoparticles. At first, a new reduction route to bismuth nanoparticles is described which are applied as starting materials in the formation of rhombohedral Bi_2Te_3 nanoparticles. After ligand removal by a novel hydrazine hydrate etching procedure, the nanoparticle powder is spark plasma sintered to a pellet with preserved crystal grain sizes. Unlike previous works on the properties of Bi_2Te_3 nanoparticles, the full thermoelectric characterization of such sintered pellets shows a highly reduced thermal conductivity and the same electric conductivity as bulk n-type Bi_2Te_3.

Introduction

Bulk Bi_2Te_3 and solid solutions thereof are the key materials for state-of-the-art thermoelectric (TE) devices at room temperature. The efficiency of such devices is defined as

$zT = \frac{\sigma S^2 T}{\kappa_L + \kappa_e}$ and peaks at 1.14 for bulk $(Bi_2Te_3)_{0.25}(Sb_2Te_3)_{0.72}(Sb_2Se_3)_{0.03}$.[38] It is estimated that a three-fold increase would result in a Carnot efficiency similar to those of conventional heat generators, thus making thermoelectric materials a promising subject in the search for new power generators.

With the electric conductivity σ, the Seebeck coefficient (or thermopower) S, the absolute temperature T, and the lattice and electronic part of the thermal conductivity κ_L and κ_e, zT can only be significantly changed by varying the Seebeck coefficient or the lattice thermal conductivity. As predicted theoretically [13, 14] and demonstrated experimentally, [39] both parameters can be manipulated by nanotechnology.

Specifically, nanoparticles have been predicted to show a strong scattering effect on phonons similar to that of atomic impurities or crystal boundaries.[40] The effect was found to be inversely related to the nanoparticle diameter. An instructive summary on the effect of nanoscalic dimensions on thermoelectric materials has been given by Dresselhaus *et al*.[41]

Consequently, several recent reports have demonstrated experimental evidence on the perspectives of nanostructured materials for thermoelectric applications, taking advantage of the phonon scattering in these materials.[42, 43]

Particularly important for large-scale applications was a work on hot-pressed bismuth antimony telluride nanoparticles fabricated by ball-milling, which yielded zT of 1.4 at 400 K.[18] In a similar approach, solution grown bismuth telluride nanostructures of approximately 30 nm in diameter were included into a $Bi_2Te_{2.7}Se_{0.3}$ bulk matrix in various concentrations, which led to a decrease in lattice thermal conductivity (1.2 W K^{-1} m^{-1}) meanwhile maintaining low resistivity (3.7 mΩ cm).[44] Both of these works applied hot-pressing of nanoparticles which is a promising approach towards nanostructured bulk materials provided the grain sizes do not increase greatly during the treatment. Particularly suitable in this respect is sintering with a pulsed direct current, known as spark plasma sintering (SPS). This method allows for relatively short sintering times which minimizes the post-synthetic crystal grain growth of nanoparticles.[45]

Since phonon scattering depends on the size and shape of the nanoparticles, a good control over these parameters is essential in achieving further improvements in thermoelectric efficiencies. Several solution-based attempts to a more controlled synthesis of large amounts of small, crystalline bismuth telluride nanoparticles have been reported. For example, crystalline and uniform bismuth telluride disks of 100-200 nm in diameter [46], 2.5 to 10 nm bismuth nanoparticles of medium crystalline quality [47] and highly crystalline bismuth telluride/bismuth sulphide core/shell nanorods of 35 to 290 nm in lengths [48] have been reported. A recent work presented a breakthrough in the size-controlled synthesis of crystalline Bi_2Te_3 nanoparticles in the range of 17 nm to 100 nm of narrow size distribution.[33] Where the thermal conductivity of these nanoparticles pressed to a dense pellet could be reduced to 0.5 W $K^{-1}m^{-1}$ at room temperature, zT was only 0.03 due to a poor electric conductivity stemming from organic residues of the former stabilizing ligands.

To date, a synthesis yielding amounts in the gram scale of uniform, sub-10-nm bismuth telluride nanoparticles of high crystallinity has not been reported.

In the first part of this paper, we report a synthesis which fulfils these requirements. In the second part we demonstrate the fabrication of a nanostructured bulk material comprising of the previously prepared particles by spark plasma sintering after carefully removing the particles’ ligands by a novel hydrazine hydrate based etching procedure. In contrast to other reported ligand removal techniques, the electric conductivity of thus purified nanoparticles is identical to the room temperature bulk value, which sets the basis for a large zT.

In the last part we will present our data on the characterization of the TE properties of such a material.

Results and discussion

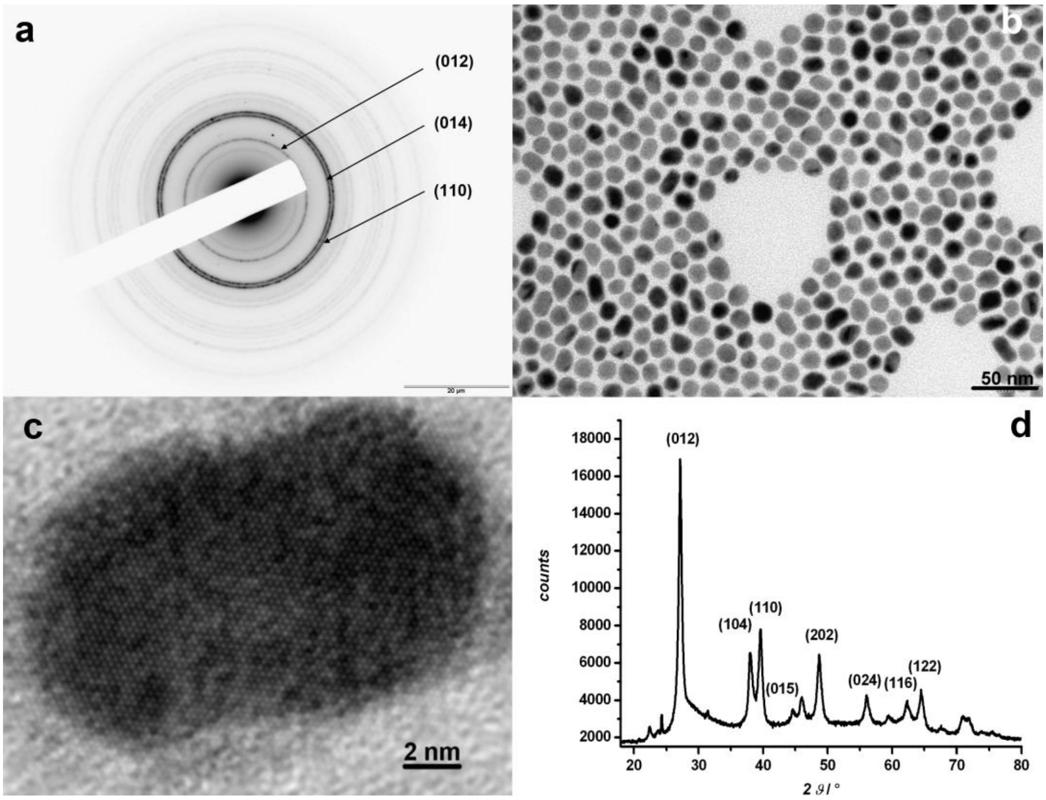

Figure B-1 (a) SAED of bismuth nanoparticles; colours inverted for clarity (b) TEM (c) HR-TEM of a single bismuth nanoparticle showing the (110) lattice spacing (d) p-XRD, indexing according to ICDD PDF-card No. 44-1246 (trigonal $(R\bar{3}m)(166)$)

The difficulty in solution-processed bismuth telluride nanoparticle synthesis is the high reactivity of tellurium with bismuth salts. Where Fang *et al.* [Ref. 12] and Ramanath *et al.* [Ref. 13] have nonetheless demonstrated impressive control over this reaction for large particle sizes, the high reactivity usually does not allow for a controlled growth of small bismuth telluride nanoparticles. An exception is the work by Badding *et al.* [Ref. 15], although even their synthetic procedure did not yield sub-10 nm particles.

The innovation of our synthesis is its two-step nature via a bismuth nanoparticle intermediate. We have tested several attempts for the synthesis of such an intermediate (see supporting information) and found it best to apply oleylamine as the reducing agent at 60 °C together with 1-docdecanethiol (DDT) as the stabilizer (**figure 1a-d**).

The as prepared bismuth nanoparticles can be treated with a solution of tellurium in trioctylphosphine (TOP-Te) without further purification in the same batch to yield a bismuth-tellurium alloy (**figure 2 a-d**). These alloy nanoparticles are single-crystalline and possess a mean particle diameter only ~20 % larger than the former bismuth species due to the inclusion of tellurium (**figure 3 a-d**).

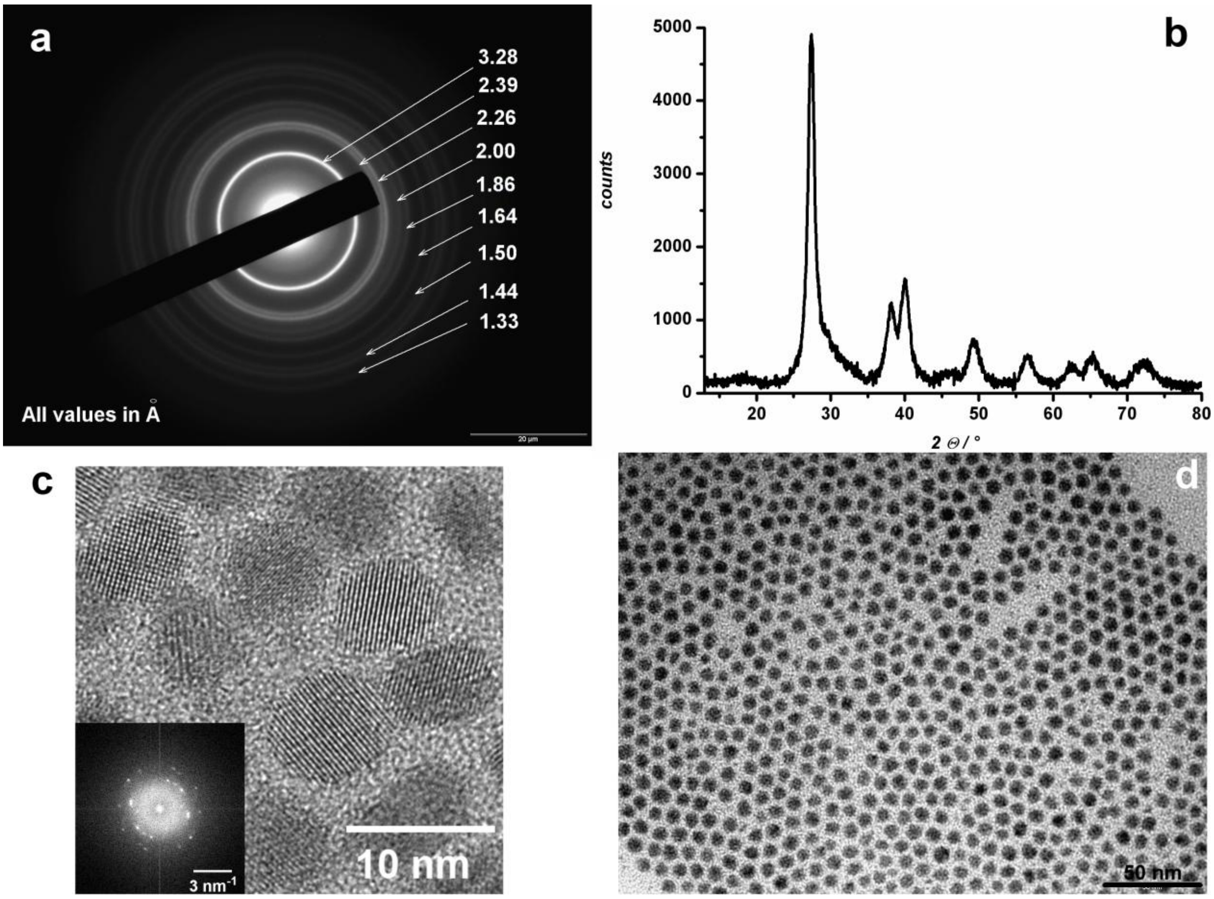

Figure B-2 Typical bismuth tellurium alloy nanoparticles; **(a)** SAED with measured d-values; **(b)** p-XRD; **(c)** HR-TEM with corresponding FFT; the predominant lattice spacing is 3.28±0.03 Å; **(d)** TEM

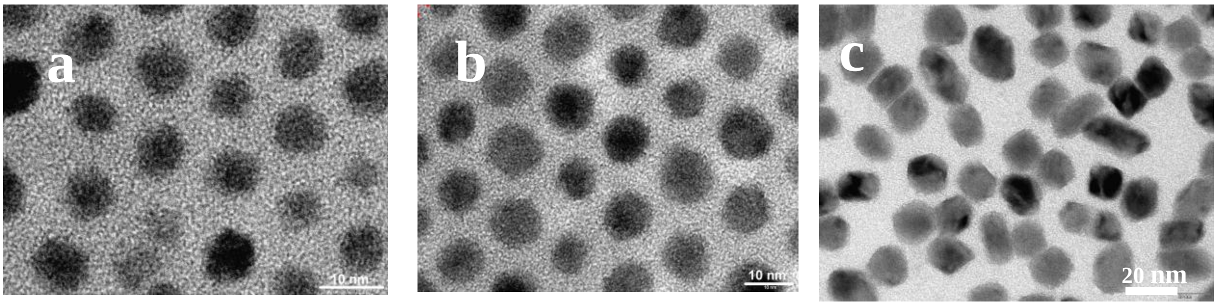

Figure B-3 Bismuth-tellurium nanoparticles **(a)** by a 30.0 mM solution with respect to the Bi precursor; **(b)** by a 90.0 mM solution with respect to the Bi precursor; **(c)** by a 30 mM solution and dilution with toluene

The randomness of this inclusion causes the broadening of the reflections in XRD measurements (**figure 2b and 4**). Bos et al. have given an extensive overview of bismuth tellurides of various compositions and have assigned them to an infinitely adaptive series of the general formular $(Bi_2)_m(Bi_2Te_3)_n$ with (m+n) being a multiple of 3.[49] Their presented XRDs of the members of this homologous series show the very little deviations in XRD reflections and intensity as one moves along from pure bismuth to bismuth telluride in the Bi_2Te_3 modification. It is believed that the large flexibility of bismuth tellurides in terms of their chemical composition leads to the broad XRD reflections.

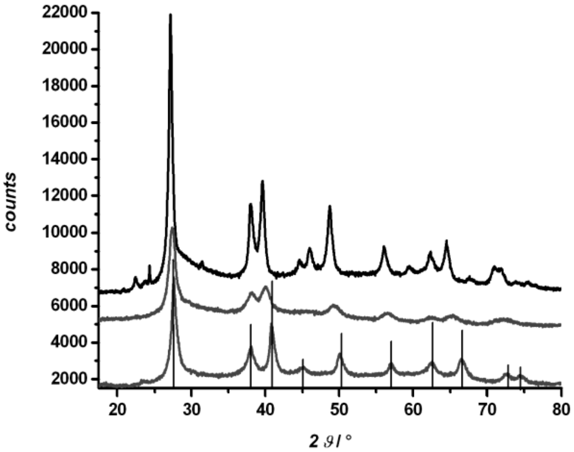

Figure B-4 p-XRD patterns of **(top)** bismuth nanoparticles; **(middle)** the same nanoparticles after alloying with tellurium; **(bottom)** the alloy after annealing at 110°C in solution; the black bars represent characteristic reflections for rhombohedral Bi_2Te_3 ($(R\bar{3}m)(166)$, PDF-Card 15-0863)

Under the specified conditions, the particles can be kept for weeks without any changes in size, composition and crystalline phase. When such a solution is heated to 110 °C for 18 hours, the particle size does not undergo significant changes. However, the shape changes slightly from almost spherical to a more rhombohedral structure and the XRD reflections shift towards practically single-phase, rhombohedral Bi_2Te_3 (space group *R*-3*m* 166) provided an appropriate amount of tellurium was added (**figure 4 and 5 a-d**). (The sharp reflections unknown to Bi_2Te_3 are assigned to excess ligand, which is explained in more detail in the supporting information.) This way, we could synthesize Bi_2Te_3 nanoparticles in a range of 7 to 50 nm in diameter depending on the size of the bismuth nanoparticles used as the starting material.

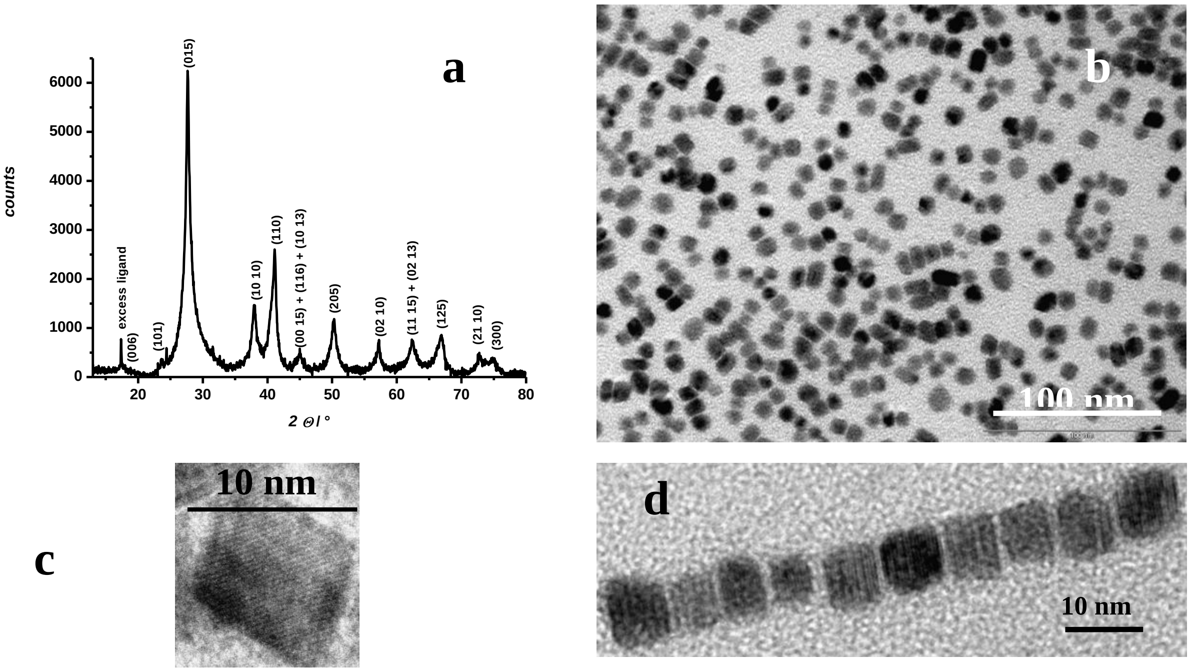

Figure B-5 Bi_2Te_3 nanoparticles **(a)** p-XRD; indexing according to ICDD PDF-card No. 15-0863 (trigonal ($R\bar{3}m$)(166)); **(b)** TEM; **(c)** + **(d)** HR-TEM of typical nanoparticles

To fabricate sintered pellets from these nanoparticles, we removed the nanoparticles’ ligand shell via a two-step procedure. In the first step, the ligand shell of DDT was exchanged by a ligand shell of oleic acid. This exchange is favoured by the weak interaction of DDT with the nanoparticles’ surface (see supporting information, **figure S5**). In the second step, oleic acid stabilized Bi_2Te_3 nanoparticles were suspended in a hydrazine hydrate/hexane two-phase mixture. We chose hydrazine hydrate at this point for three reasons:

(1) As a base it readily deprotonates the acid leaving it incapable of binding to the nanoparticles’ surface. (2) As a reducing agent it repairs oxide defects on the nanoparticles surface. (3) In comparison with the highly explosive and carcinogenic anhydrous hydrazine, hydrazine hydrate can be handled relatively safely in a fume hood under ambient conditions.

As a result of the hydrazine treatment, the ligand-free, polar nanoparticles transferred into the polar phase, whereas the aliphatic hydrazinium oleate remained in the organic phase. Detailed NMR-studies of a similar process can be found elsewhere.[50]. Drying of thus purified nanoparticles yielded a Bi_2Te_3 nanopowder.

This nanopowder was spark plasma sintered to a macroscopic pellet. Provided a careful control of the sintering parameters, we observed the size and phase of the nanoparticles in the pellet to be the same as those obtained directly after synthesis. This is supported by HR-SEM imaging displaying small crystalline grains of ~ 15 nm in a sintered sample of originally 14 nm big nanoparticles and SAED measurements where the fringe patterns indicate polycrystallinity (**figure 6**). (For a more detailed study of the effect of different sintering parameters see supporting information.)

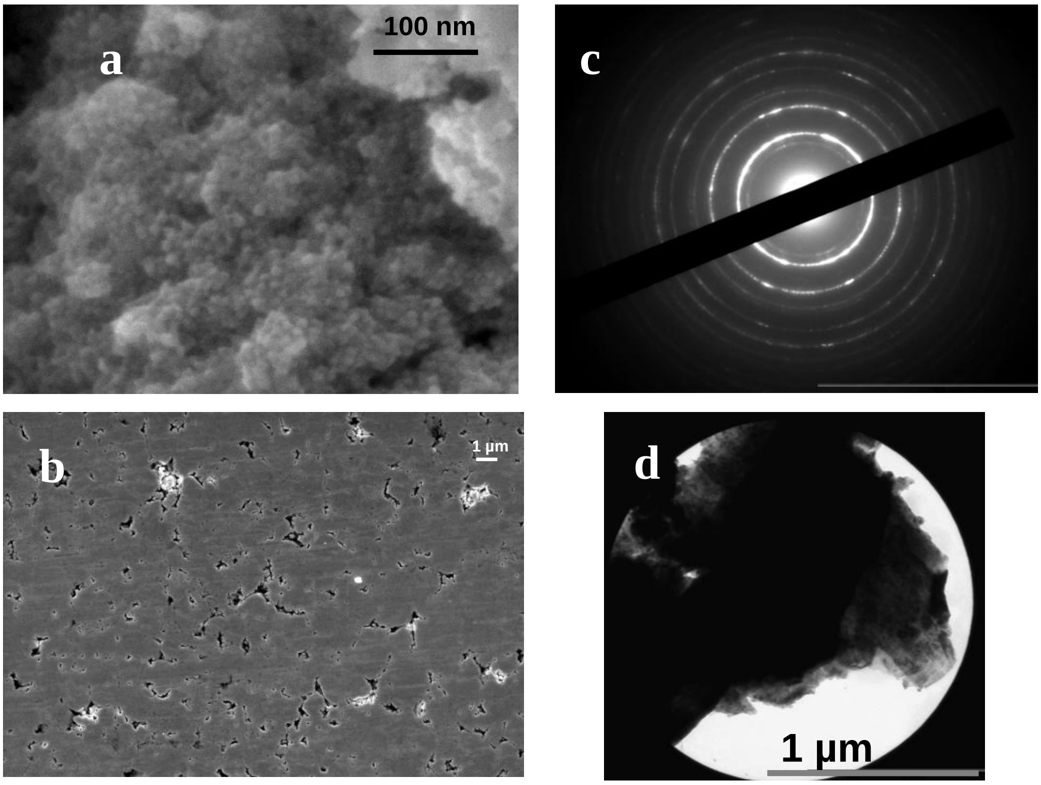

Figure B-6 (a) SEM image of sintered Bi_2Te_3 nanoparticles (14 nm). **(b)** Low-magnification SEM image of the same sample displaying occasional voids**. (c)** SAED of a small piece of a nanoparticle pellet **(d)** TEM image of the piece

We now turn to the discussion of thermoelectric properties of the Bi_2Te_3 nanoparticles in the order (1) electric conductivity, (2) thermopower and (3) thermal conductivity:

Our transport measurements under dc conditions show a classic ohmic and semiconducting behaviour (**figure 7 a**). This is confirmed by ac resistivity measurements between 5 K and 300 K showing a 20 % drop in resistivity as one moves along in this temperature regime (**figure 7 b**). With respect to what was reported about n-type bulk Bi_2Te_3 (ref. [16]) this is unusual as one should expect metallic behaviour. However, it has to be stressed here that the present material possesses a highly polycrystalline and granular structure. Such materials are known to show significantly altered transport properties as compared to their homogeneously disordered equivalents.[51] Still, the room temperature resistivity is less than 50 % higher than that of n-type bulk Bi_2Te_3 (~1.4 mΩ cm), which is unprecedented by solution-grown Bi_2Te_3 nanoparticles.

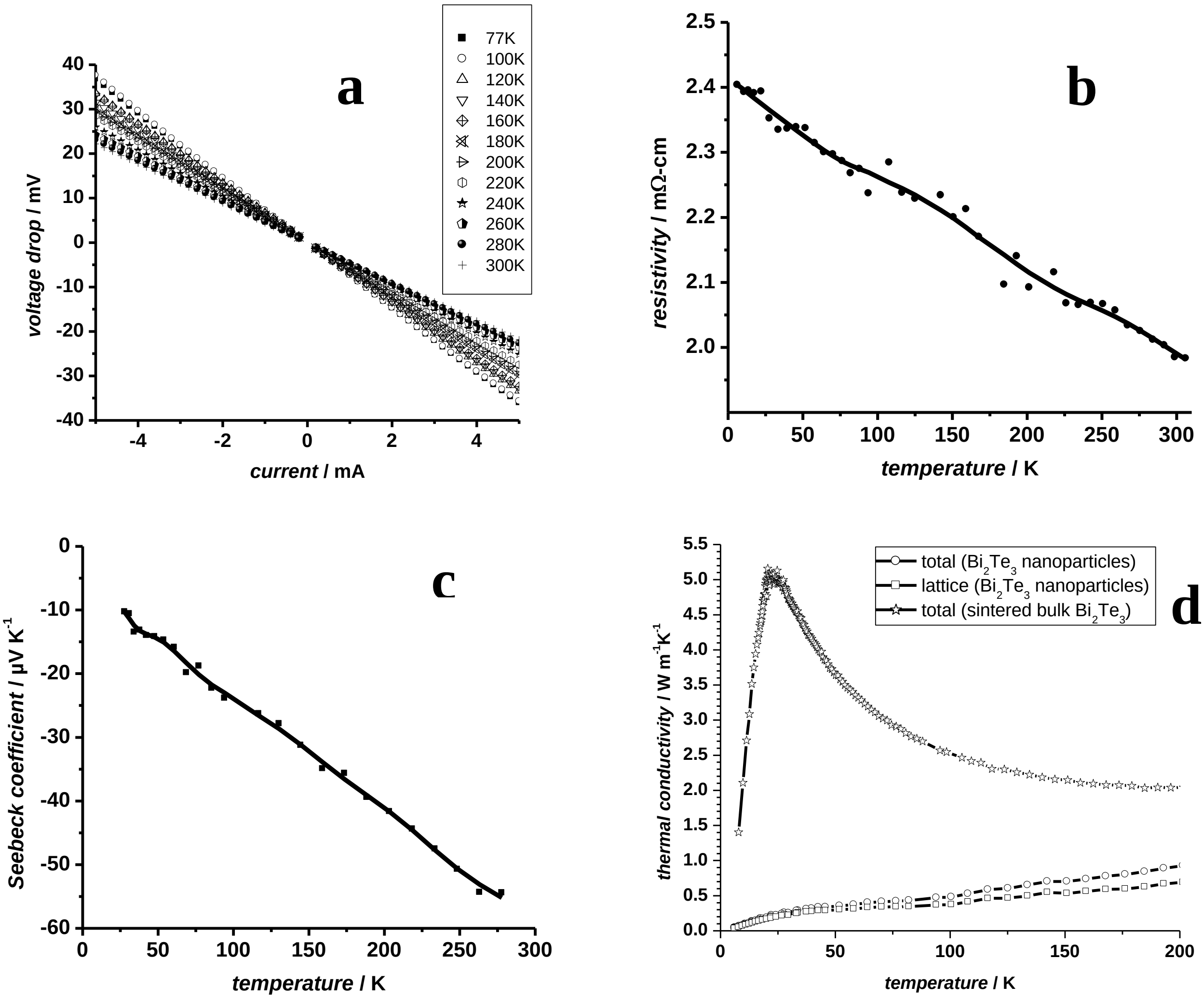

Figure B-7 Transport properties of Bi_2Te_3 nanoparticles: **(a)** dc I/V-measurements **(b)** ac resistivity **(c)** thermopower **(d)** total and lattice thermal conductivity of a pellet of sintered nanoparticles with conditions "c" (**figure S6 ii**). The thermal conductivity data includes a sintered bulk Bi_2Te_3 sample for comparison.

The thermopower of the sintered Bi_2Te_3 nanoparticle pellet shows clear n-type behaviour (**figure 7** c) and a room temperature absolute value of 60 µV K^{-1} which compares to 180 µV K^{-1} for n-type bulk Bi_2Te_3. This is fully in accordance with the work of Glatz and Beloborodov who predicted a decrease in thermopower "most effective for small grains" due to "the delicate competition of the corrections of thermoelectric coefficient and the electric conductivity" (Ref. [18]).

For reasons stated above, materials of small crystal grain sizes are most promising for thermoelectrics in terms of their thermal conductivity. This is immediately apparent from

figure 7 (d) which shows the thermal conductivity of such a material. Due to the significant radiative heat loss above 200 K only the data below this temperature can be considered. We also display the lattice thermal conductivity on subtracting the electronic contribution by assuming the Sommerfeld value for the Lorenz number. For comparison we included the thermal conductivity of a sintered sample of commercially available bulk Bi_2Te_3.

Due to the break-down of Umklapp-processes at low temperatures, single crystals of sufficiently large grain sizes show a maximum in thermal conductivity between 4 K and 9 K before dropping sharply when approaching the zero-point in absolute temperature.[52] Our homogeneously disordered bulk sample displays exactly this behaviour although the maximum occurs at a higher temperature and possesses a lower value due to the non-single crystalline nature. In contrast, the sintered Bi_2Te_3 nanoparticle pellets show a decrease in thermal conductivity without passing a maximum when falling below a certain temperature – in our case approximately 30 K. It is believed that at this temperature, the phonon mean free path approaches its maximum value and is restricted to it for all temperatures below the threshold temperature due to limited grain boundaries. If we apply the kinetic gas theory derived approximation for the thermal conductivity

$$\kappa_L = \frac{1}{3} c_v \upsilon l_t$$

(where κ_L is the lattice thermal conductivity, c_v the specific heat for unit volume, υ the speed of sound and l_t the phonon mean free path), it is apparent that for a constant l_t, the temperature dependence of the lattice thermal conductivity should be that of the specific heat. On using Debye's theory, for low temperatures the specific heat should have a T^2 to T^3 dependence, which is reasonably resembled by our measurements between 5 K and 30 K. Most importantly in the thermal conductivity comparison of the bulk to nanoparticle samples, we observe a minimum depletion by a factor 2 which increases to as much as one order of magnitude. This is in agreement with what was reported by Badding *et al.* [ref. 15] for a similar sample showing the validity of these measurements.

In the last part of this communication, we discuss the effect of optimized fabrication parameters on the thermoelectric properties.

In **figure 8** we prolonged the sintering duration in order to improve the thermopower of otherwise identical sintered Bi2Te3 nanoparticle pellets**.** We also present the measurements of a sintered Bi_2Te_3 bulk sample for comparison. Longer sintering times repeatedly yielded a higher absolute thermopower and a lower resistivity. The room temperature thermopower increased to 80 $\mu V\ K^{-1}$ and the resistivity decreased to 1.3 mΩ cm which is identical with the value for n-type bulk Bi_2Te_3. Moreover, the temperature dependence of charge carrier transport is now metallic in accordance with the bulk material.

From SEM imaging it is apparent that the granular structure is unaffected by the longer sintering duration (**figure 8 i** and **ii**). As a result, we measure a lattice thermal conductivity of 0.8 $Wm^{-1}K^{-1}$ at 200 K, which is consistent with the measurement for short sintering durations in **figure 7 d.**

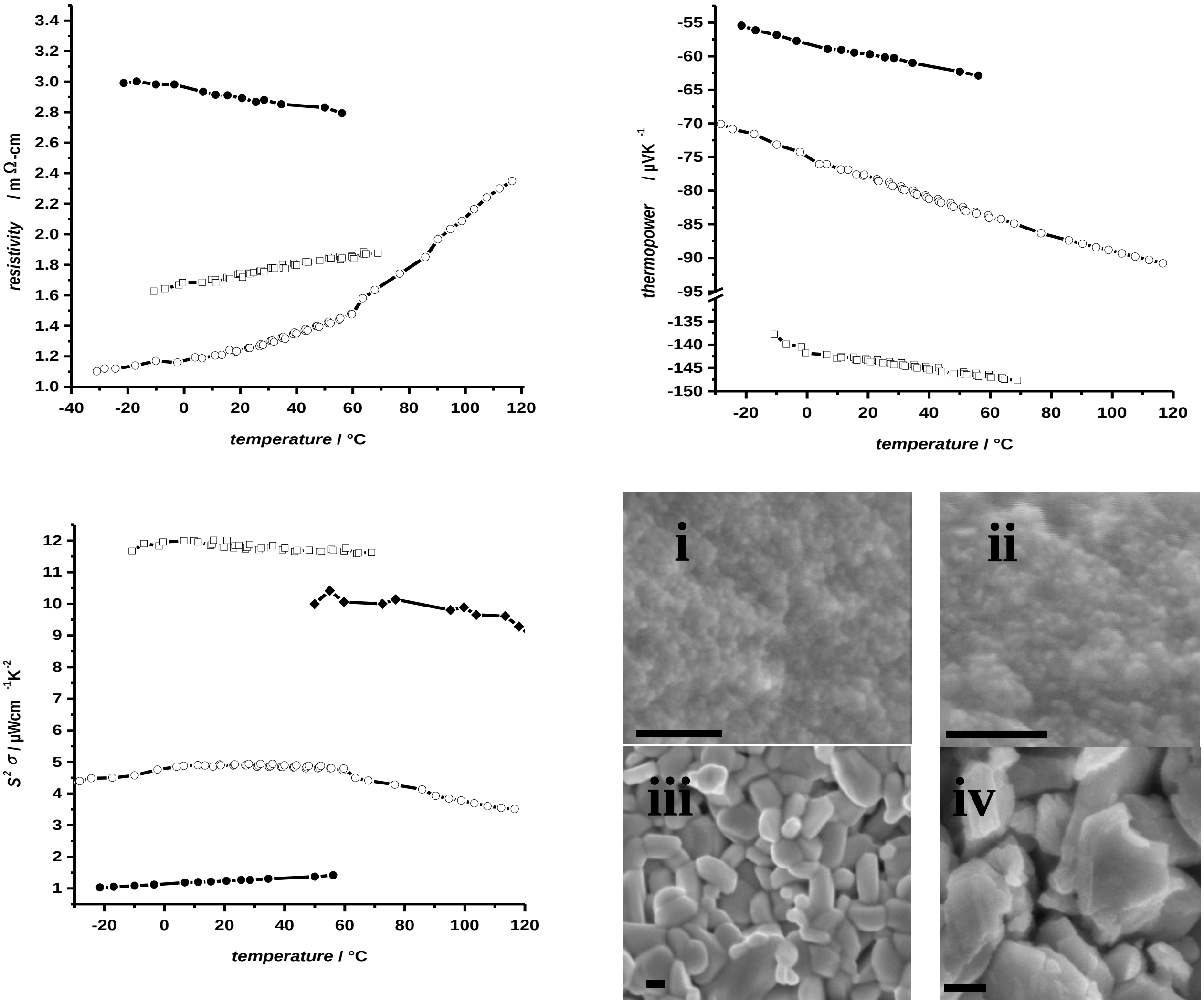

Figure B-8 Resistivity, thermopower, power factor and morphology of sintered 9 nm Bi_2Te_3 nanoparticles. **Closed circles**: Short sintering (conditions “c”), morphology “**i**”; **Open circles**: Long sintering (conditions “d”), morphology “**ii**”; **Closed diamonds**: after thermal treatment, morphology “**iii**”; **open squares**: Homemade bulk Bi_2Te_3 standard (SPS conditions “e”), morphology “**iv**”. All scale bars equal 100 nm.

For better comparison, we summarize the thermoelectric data so far acquired in this work together with suitable reference compounds reported in literature in **table 1**.

When applying a post-sintering thermal treatment at 250 °C in a 0.1 bar helium atmosphere, the power factor of a typical pellet of nanoparticles increases from 1 to almost 10 $\mu Wcm^{-1}K^{-2}$

(**figure 8**). It is reported that at this temperature no melting is to be expected for Bi_2Te_3 nanoparticles.[15] Where SEM imaging suggests a significant reorganization of the nanoparticle pellet’s structure (**figure 8 iii**), XRD measurements (see supporting information) reveal that the crystalline domains only grow slightly (~30 nm) during this process. It is therefore likely that each of the ~300 nm grains in **figure 8 iii** consists of multiple crystalline domains to maintain a low thermal conductivity. This result suggests that careful thermal treatment of the sintered Bi_2Te_3 nanoparticle pellets reported in this work has the potential to yield a zT of at least 0.4 mainly due to an increase in thermopower by optimized crystal grain sizes. This will be subject to a separated publication.

Type of Bi_2Te_3 sample	Resistivity [mΩ cm] (300 K)	Thermopower [µV K^{-1}] (300 K)	Thermal conductivity [W m^{-1} K^{-1}] (200 K)	zT (300 K)
n-type Bulk	**1.4** [Ref. 16]	**180** [Ref. 16]	**2.2** [sintered sample]	**0.32**
this work	**1.3**	**80**	**0.8**	**0.2**
[Ref. 15]	**20**	**91**	**0.5**	**0.03**

Table B-1: Comparison of thermoelectric parameters of selected Bi_2Te_3 samples. Note that all values were recorded at 300 K except for the thermal conductivity which can only be considered up to 200 K due to radiation effects at higher temperatures.

Conclusion

Because of the large reactivity of bismuth and tellurium, the key to unprecedented sub-10 nm single-crystalline Bi_2Te_3 nanoparticles of narrow size distribution is a bismuth nanoparticle intermediate as part of a one-pot two-step solution based procedure. To meet the key requirement for a sufficient electrical conductivity and thus a large power factor we introduced a novel hydrazine hydrate based ligand removal prior to the sintering of the nanoparticles to macroscopic pellets. This yielded an electrical conductivity which is virtually identical to typical n-type bulk samples. The total thermal conductivity of such nanoparticle pellets is by as much as one order of magnitude smaller than that of the bulk material showing characteristic features of a highly polycrystalline sample. The power factor of 5 $\mu W K^{-2} cm^{-1}$ is unprecedented by previous samples purely made from solution-grown Bi_2Te_3 nanoparticles. Optimizing the thermopower by finding suitable grain sizes holds for further improvements.

Experimental

All manipulations were carried out under an inert atmosphere using standard Schlenck techniques if not stated otherwise.

(I) Synthesis of 7-9 nm bismuth nanoparticles

In a typical synthesis, bismuth acetate (1.136 g, 3.000 mmol, 99 % Aldrich) was mixed with 1-dodecanethiol (33.3 mL, 98% Aldrich) and heated to 45 °C for 45 min under vacuum on which a transparent, yellow solution was obtained. The flask was flooded with nitrogen, set to ambient pressure and it was heated to 60 °C on which oleylamine (66.7 mL, 70 %, Aldrich) was quickly added under stirring. The solution turned immediately orange and gradually darkened over the course of several hours. After 24 h the as prepared bismuth nanoparticles were ready for further manipulations.

(II) Synthesis of 12-14 nm bismuth nanoparticles

All manipulations were identical to **(I)** except for the amount of 1-dodecanethiol (20.0 mL). After the evacuation period and flooding with nitrogen, toluene (40.0 mL, analytical grade, Fluka) was added, followed by oleylamine (40.0 mL). The solution darkened immediately.

(III) Synthesis of 40 nm bismuth nanoparticles

All manipulations were identical to **(II)** but instead of oleylamine distilled TOP (9.0 mL, 90 %, Merck) was injected quickly.

(IV) Purification of bismuth nanoparticles for characterization

A fraction of the dark-brown colloidal solution obtained under **(I-III)** was mixed with ethanol (25 vol-%, analytical grade, Fluka) and centrifuged at 4500 rpm for 5 min. The light yellow supernatant was removed under nitrogen and the almost black precipitate dissolved in a few drops of chloroform (analytical grade, Fluka). Such a solution can either be purified by one further precipitation cycle with ethanol/chloroform or be treated with a spatula tip of $(mPEO2000)_2PEI600$ ligand. The ligand exchange occurs practically instantaneously on short shaking after which multiple precipitation cycles with hexane as the precipitation agent and chloroform as solvent after centrifugation may be applied. (For more details see supporting information). The purified nanoparticles should be stored in the absence of oxygen to prevent aging.

(V) Preparation of 0.500 M solution of tellurium in TOP (Te@TOP)

In a glovebox, tellurium (1.276 g, 10.00 mmol, 99.999 %, Chempur) and octadecylphosphonic acid (102 mg, Alfa Aesar) were suspended in distilled TOP (20.0 mL, 90 %, Merck) under stirring. It was heated stepwise to 220 °C from room temperature by increasing the temperature by approximately 50 °C every hour. The final temperature was kept until a completely transparent, orange solution was obtained which turned to bright-yellow on cooling to room temperature. The solution was stored in the glovebox.

(VI) Synthesis of bismuth-tellurium-alloy nanoparticles

The as synthesized bismuth nanoparticles from **(I-III)** were used in the same flask without any further purification. For example, **(V)** (9.0 mL, 4.5 mmol Te) was injected into the product from **(I)** at 60 °C under stirring. The reaction system was kept under these conditions for 2-3 days. For characterization, the procedures described under **(IV)** were applied.

(VII) Synthesis of Bi_2Te_3 nanoparticles

The as synthesized **(VI)** was heated in the same flask without further purification to 110 °C for 18 h after which it was cooled to room temperature. For characterization the particles were treated according to **(IV).**

(VIII) Ligand removal from Bi_2Te_3 nanoparticles

As prepared Bi_2Te_3 nanoparticles were purified on undergoing three precipitation cycles with ethanol/chloroform as described under **(IV)** on which the black precipitate was insoluble in chloroform. After removing the supernatant, the precipitate was mixed with a large excess of oleic acid (~15 mL, 90 %, Aldrich) and allowed to stir overnight on which a black suspension was formed. The supernatant was removed after short centrifugation and fresh oleic acid was added on which the mixture was allowed to stir for several hours. The supernatant was removed again after centrifugation and it was washed three times with hexane (analytical grade, Aldrich). A few millilitres of fresh hexane were added and the black, insoluble precipitate suspended. An equal volume fraction of distilled hydrazine hydrate (98 %, Aldrich) was added to form a two-phase system. On stirring overnight followed by centrifugation (4500 rpm, 5 min), practically the entire black precipitate had passed into the hydrazine phase leaving a milky-white precipitate at the bottom of the (upper) hexane phase. If the phase transfer does not occur quantitatively, a few drops of chloroform may be added.

The hexane phase was discarded and the hydrazine hydrate supernatant carefully removed from the black precipitate in the absence of air. It was washed three more times with fresh hydrazine hydrate and hexane until the black precipitate effortlessly went into the hydrazine phase and the hexane phase appeared completely transparent. All solvents were removed and it was dried under vacuum for several hours on which a fine black powder was obtained.

Typically, the starting amounts specified under **(I)** yield approximately 1 g of Bi_2Te_3 nanopowder.

(IX) Fabrication of Bi_2Te_3 nanoparticle pellets by spark plasma sintering

Typically, 100 mg of **(VIII)** kept under argon were loaded into a WC/Co die of 8.0 mm x 1.5 mm in area. The powder was pressed to a solid pellet of equal dimensions and approximately 1.8 mm in height by spark plasma sintering in a SPS-515 ET/M apparatus (Dr. Sinter®lab) under varying conditions. For example, on applying 325 - 358 MPa pressure, the die containing the nanopowder was heated from 20 °C to 50 °C in 5.0 min with no hold time (conditions "c") or 5.0 min hold time (conditions "d") by applying a DC current between 0 – 165 A, and immediately allowed to cool down to room temperature. The obtained Bi_2Te_3 nanoparticle pellets were mechanically robust and silver-metallic in appearance.

For the synthesis of Bi_2Te_3 bulk materials, 100 mg of commercially available Bi_2Te_3 (99.99 %) were heated from 20°C to 300 °C in 30 min with 10 min hold time (conditions "e"). For additional information on temperature/time profiles see supporting information.

Characterization

(HR-)TEM imaging was performed with a Philips CM-300 UT microscope at 200 kV or a JEM-Jeol-1011 microscope at 100 kV with a CCD camera (Gatan 694). SEM images were obtained on a LEO1550 scanning electron microscope with a spatial resolution of ~ 1 nm,

Powder XRDs were recorded using a Philipps X`Pert-diffractometer with Bragg-Brentano-geometry on applying copper-K_α radiation ($\lambda = 154.178$ pm, $U = 45$ kV; $I = 40$ mA).

Dynamic light scattering measurements were carried out with a Malvern Zetasizer Nano-ZS-apparatus equipped with 173 ° back-scattering system and He-Ne-Laser of 633 nm emission wavelength.

For transport measurements under dc conditions, four 0.25 mm^2 gold electrodes (40 nm thickness, 1 nm titanium wetting layer below) were vacuum deposited onto a pellet of sintered nanoparticles, with a spacing of 0.5 mm between contact 1 and 2 and 3 and 4, respectively. The spacing between contact 2 and 3 was up to 4.0 mm. A probe station (Lakeshore desert) with micromanipulators and Semiconductor parameter analyzer (Keithley-4200) was applied to measure the transport properties under vacuum (10^{-3} mbar) between 77 K and 300 K.

For transport measurements under ac conditions, four 50 µm gold wires were glued (conductive silver glue) onto the sample with the geometry specified above in air and allowed to dry for several hours under helium. The gold wires were brazed to a physical property measurement system (Quantum Design) in air and the transport properties measured under helium between 5 K and 300 K. The excitation current was 0.2 mA to 2.0 mA depending on the sample.

For thermopower and thermal conductivity measurements, the sample was equipped with four short copper bars glued to the sample at 150 °C for thirty minutes in an argon atmosphere in a similar geometry as for the transport measurements using a conductive glue (Polytech, EpoTek H20E). The copper bars were contacted to a physical property measurement system (Quantum Design) and the thermoelectric properties measured between 5 K and 300 K by a relaxation-time method and a low-frequency square-wave using two thermometers under a reduced helium atmosphere.

For high temperature measurements of the thermopower and resistivity a ZEM-3 apparatus (ULVAC-RIKO) was applied under a low-pressure helium atmosphere. The thermopower was determined by a static dc method where the resistivity was simultaneously measured by a four-terminal set-up.

Supporting Information

Thermoelectric characterization of Bi_2Te_3 nanoparticles

Marcus Scheele[*,1], *Niels Oeschler*[2], *Katrin Meier*[2], *Andreas Kornowski*[1], *Christian Klinke*[1]
and Horst Weller[1]

[1]*University of Hamburg, Institute for Physical Chemistry, Grindelallee 117, 20146 Hamburg, Germany*

[2]*Max-Planck-Institute for Chemical Physics of Solids, Noethnitzer Strasse 40, 01187 Dresden, Germany*

* To whom correspondence should be addressed

Study of reduction routes to bismuth and bismuth telluride nanoparticles

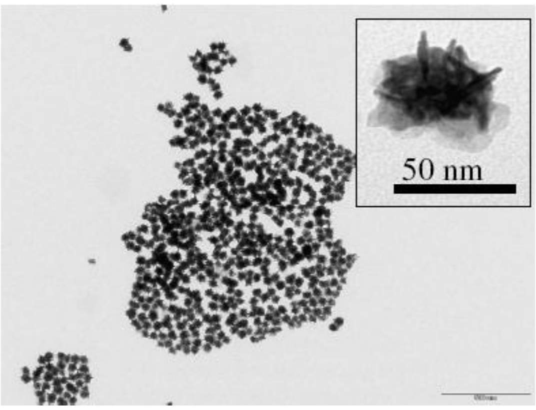

Figure B-S1 (a): TEM image of bismuth telluride nanostructures obtained by direct rduction with TOP-Te

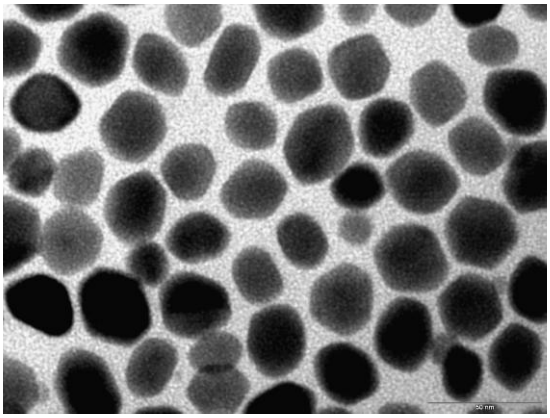

Figure B-S1 (b): TEM image of bismuth nanoparticles obtained by direct reduction with pure TOP under identical conditions

For example, if a solution of bismuth(III) acetate in 1-dodecanethiol (DDT) and toluene is treated with tellurium in trioctylphosphine (TOP-Te) at 60 °C, a dark brown solution is obtained within seconds. Electron microscopy reveals the formation of irregular shaped nanostars, several tens of nanometers in diameter (**Figure S1a**). If the solution mentioned above is treated under identical conditions with the same amount of pure TOP replacing TOP-Te, over 24 h are required to complete the reaction yielding bismuth nanoparticles (**Figure S1b**).

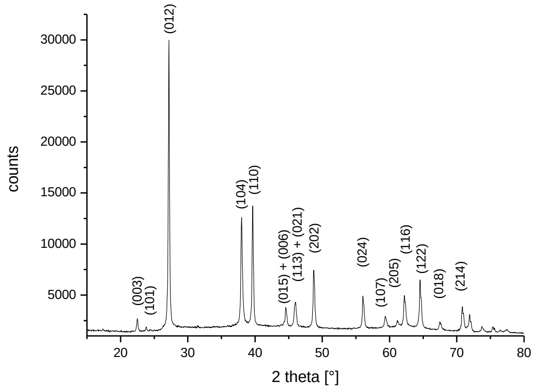

Figure B-S2: p-XRD of bulk bismuth obtained by reduction with 1-dodecanethiol; indexing according to ICDD PDF-card No. 44-1246 (rhombohedral (R$\bar{3}$m)(166))

In fact, even DDT itself may reduce a solution of Bi^{3+} in pure DDT on exceeding a certain, concentration dependent threshold temperature. For example, a solution of 0.3 mmol Bi^{3+} in 2.0 mL DDT will turn from bright yellow to colourless within minutes meanwhile forming a black precipitate when the solution temperature exceeds 70 °C. The powder XRD of the black precipitate shows single phase bulk bismuth (**Figure S2**). Note that no traces of crystalline sulphides can be observed. Due to the consumption of DDT throughout the nanoparticle formation, the particle growth is uncontrolled and leads to bulk bismuth once the nucleation is initiated.

Without attempting a complete case study, we observe the mean bismuth particle diameter to be strongly dependent on the concentration of reducing agent, the concentration of bismuth precursor, the stabilizer concentration and the type of reducing agent (**Figure S3 a-c**). Note the work of Wang et al. in this respect.[53]

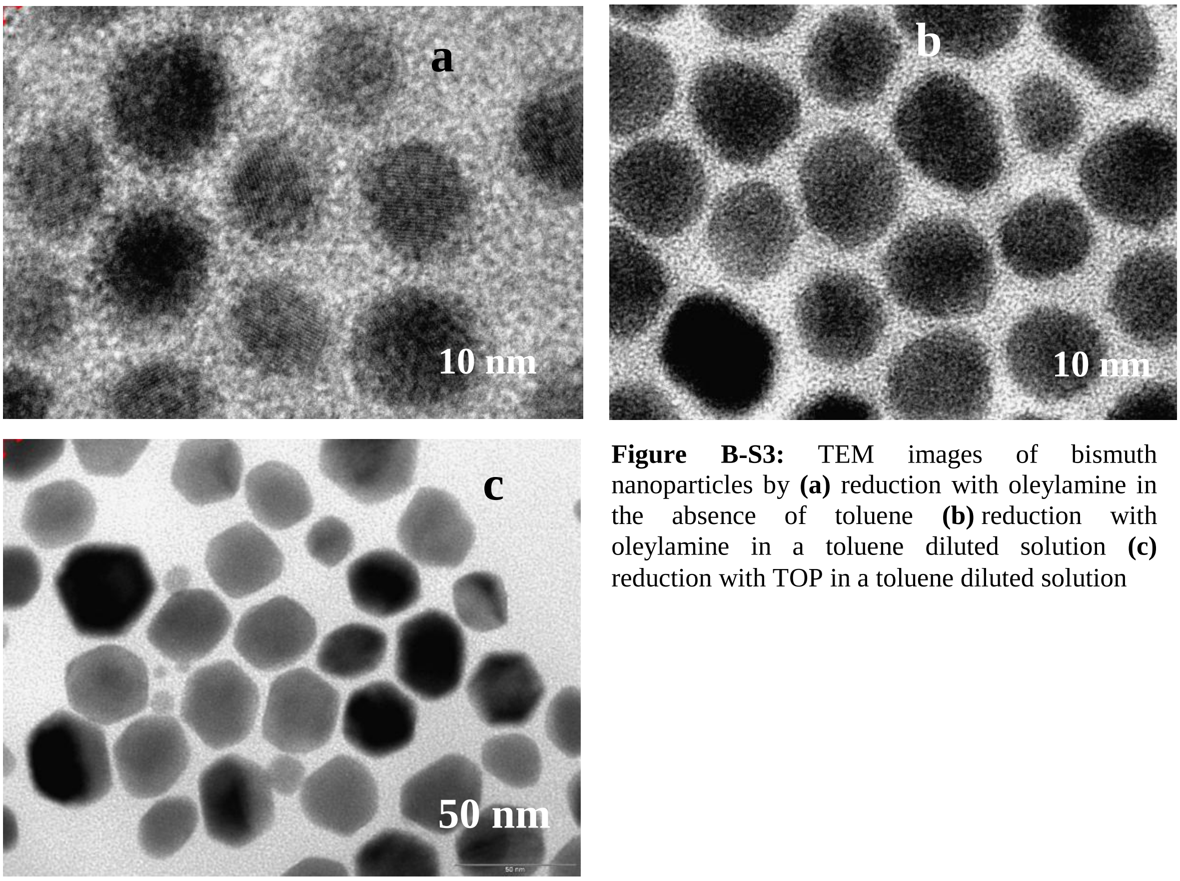

Figure B-S3: TEM images of bismuth nanoparticles by **(a)** reduction with oleylamine in the absence of toluene **(b)** reduction with oleylamine in a toluene diluted solution **(c)** reduction with TOP in a toluene diluted solution

Study of colloidal stability of bismuth telluride nanoparticles

The as synthesized nanoparticles are only partially stable as colloids which stems from the consumption of the stabilizer DDT throughout the annealing process. However, practically all of the formally insoluble precipitate can be dissolved in common organic solvents on adding extra stabilizer after completion of the reaction. As DDT appears to be only loosely bound to the nanoparticles' surface, no more than two washing steps may be applied to preserve the particles' solubility in organic solvents. Even after a single washing step, the colloidal stability is usually quenched within hours unless very concentrated solutions are prepared. To allow for high quality TEM characterization, we apply a polyethyleneoxide-based ligand (**Figure S4**) to obtain practically unlimited colloidal stability in chloroform, even for very dilute solutions after multiple washing procedures whenever necessary (**Figure S5**). The synthesis and characterization of the ligand $(mPEO2000)_2(PEI600)$ was described elsewhere.[54]

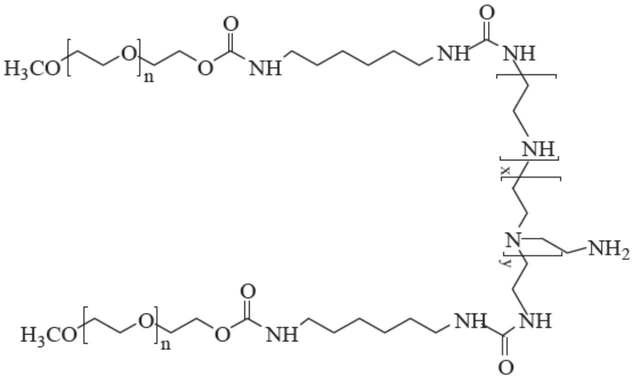

Figure B-S4: $(mPEO2000)_2PEI600$ ligand applied for long-term colloidal stability of Bi_2Te_3 nanoparticles

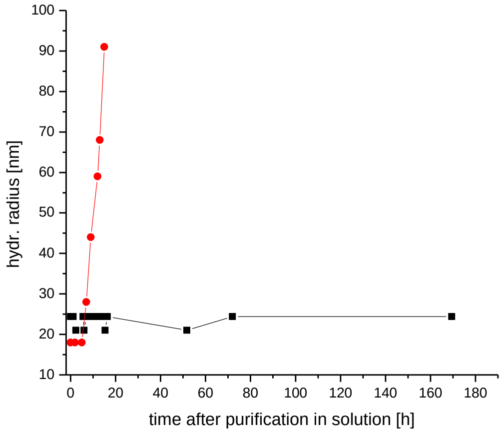

Figure B-S5: Comparison of Bi2Te3 nanoparticle stability in solution as indicated by the hydrodynamic radius with 1-dodecanethiol (red) and $(mPEO2000)_2PEI600$ (black) as stabilizers

On the effect of different sintering parameters on the structure and the transport properties of the nanoparticle pellets

The crystal grain sizes of the pellets of nanoparticles after SPS were determined by XRD, SEM and SAED. A strong dependence of the full-width-half-maximum of Bi_2Te_3 reflections in XRD on the sintering conditions was observed. Under the conditions specified above (conditions "c", **Figure S6**), practically no growth of crystalline domains could be observed from XRD patterns as verified by applying the Debye-Scherrer-equation (**Figure S7**).

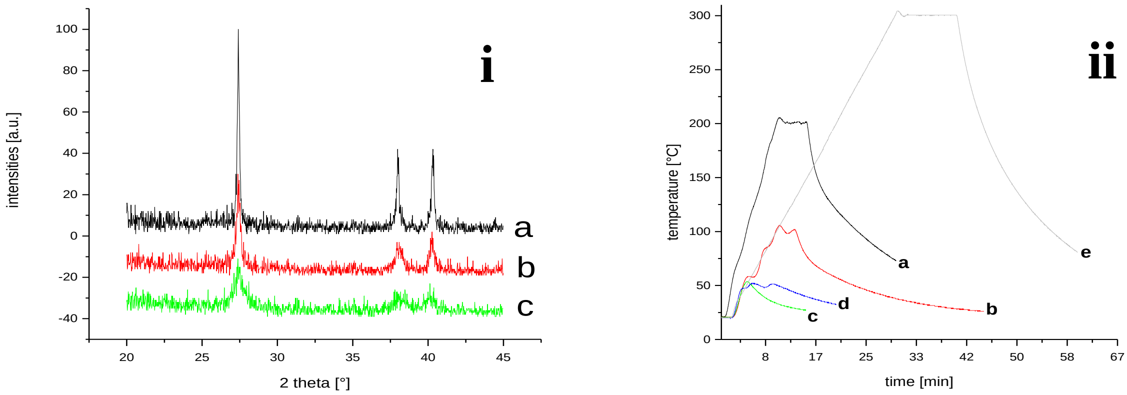

Figure B-S6: (i) XRDs of sintered Bi_2Te_3 nanoparticle pellets for varying SPS conditions **(ii)** Corresponding temperature vs time profiles during SPS of the nanoparticles

On the other hand, when the duration and/or the maximum temperature are increased, the crystal grain sizes grow significantly as derived from XRD full-width-half-maximum reflexes (conditions “a” and “b”, **Figure S6**).

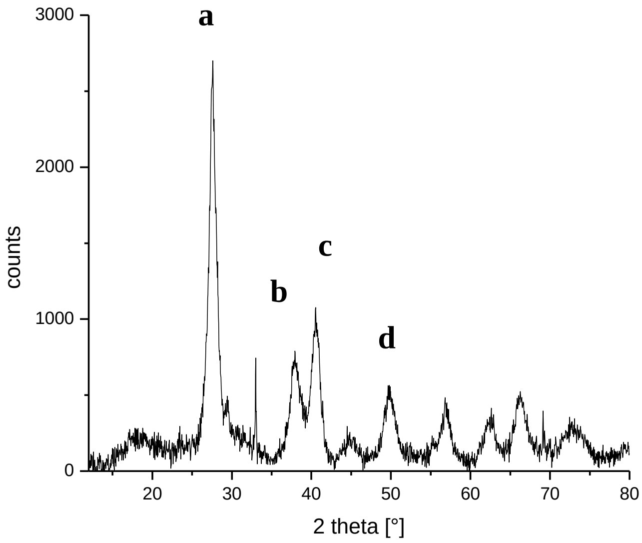

Figure B-S7: XRD of a pellet of sintered Bi_2Te_3 nanoparticles (conditions “c”). Nanoparticle grain size according to the Debye-Scherrer equation: a: 9.3 nm, b: 5.9 nm, c: 8.7 nm, d: 7.1 nm

Study of the structural changes in the pellets of nanoparticles during thermal treatment

When comparing the p-XRDs of a pellet of nanoparticles before thermal treatment (**Figure S7**) and after (**Figure S8**) it becomes obvious that the relatively low temperatures have induced a grain growth from 9 nm to 30 nm as derived by the Debye-Scherrer-equation. XRD measurements of the mere surface of the same pellet reveal significantly larger crystal grain sizes of 77 nm as derived by Debye-Scherrer (**Figure S9**).

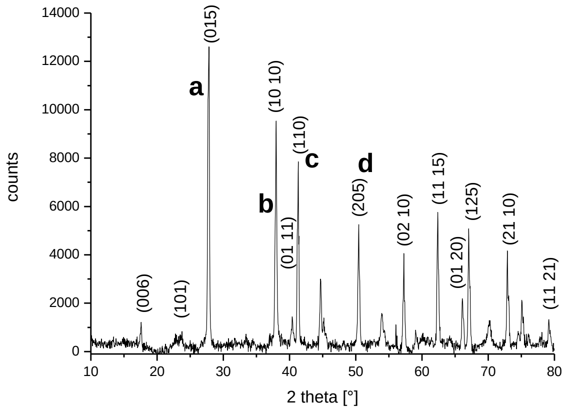

Figure B-S8: XRD of the interior of the thermally treated pellet of nanoparticles characterized in figure **8**. Grain sizes according to the Debye-Scherrer-equation: a: 30 nm, b: 33 nm, c: 30 nm, d: 29 nm.

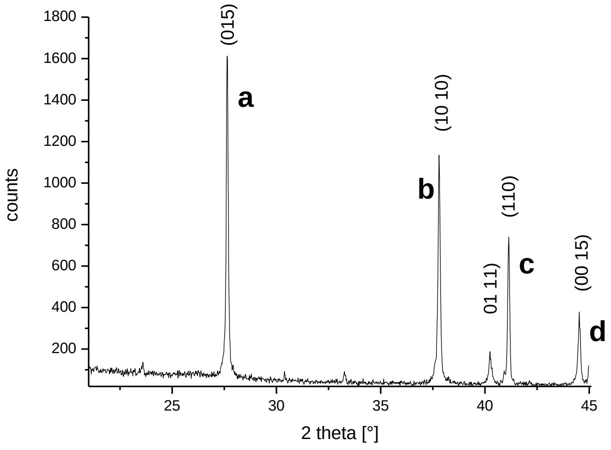

Figure B-S9: XRD of the surface of the thermally treated pellet of nanoparticles as characterized in figure **8**. Grain sizes according to the Debye-Scherrer-equation: a: 77 nm, b: 78 nm, c: 87 nm, d: 69 nm.

Assignment of unusual reflections in the bismuth and bismuth telluride XRDs

All reflections in **Figure 1d**, **4** and **5a** which cannot be assigned to bismuth or bismuth telluride are unusually sharp and occur at high lattice constants (2.5 Å and above). This is typical for excess ligands or metal precursor and can be observed quite frequently in solution-processed nanoparticle synthesis. To confirm this, **Figure S10** and **S11** display comparisons of the XRDs of purified nanoparticle samples in the figures at question with the XRD of the crude reaction product. Note that in the latter, the intensities were depleted by the factor 20 to make them comparable to the former reflection intensities. This way, the only reflections visible are those of the excess ligand or metal precursor completely suppressing those of the actual nanoparticle product. It is therefore not surprising that even small amounts of residues in the purified product are also visible besides the now predominant bismuth or bismuth telluride reflections. The reason why we present XRDs of such slightly impure compounds here is the poor bonding of the DDT ligand to the nanoparticle surface resulting in the loss of the majority of the ligand sphere when more than one washing step is applied. In this case, especially the bismuth nanoparticles are found to be highly sensitive towards oxidation which would be readily visible in the XRD. A sufficient amount of ligands suppresses this effect and allows for high quality XRD data on the expense of the excess ligand reflections as observed in the **Figures 1d**, **4** and **5a.**

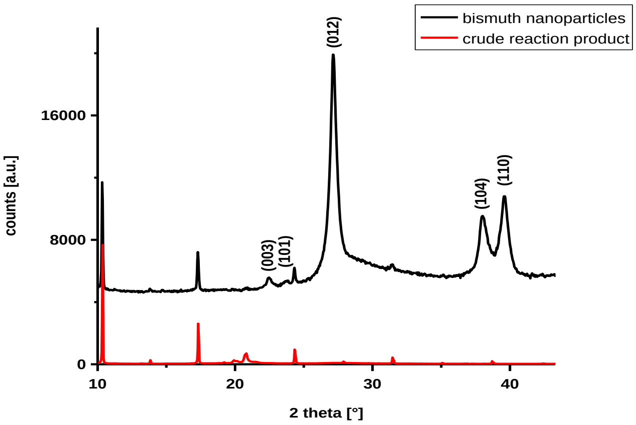

Figure B-S10: XRD of purified bismuth nanoparticles as compared to the XRD of the crude reaction product.

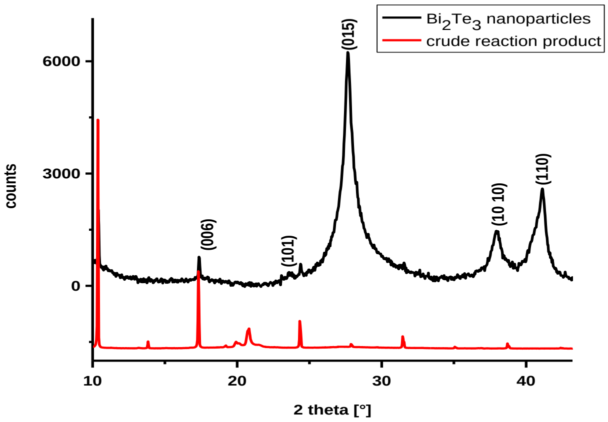

Figure B-S11: XRD of purified bismuth telluride nanoparticles as compared to the XRD of the crude reaction product.

Chapter C

Colloidal nanostructures as building blocks for macroscopic thermoelectric materials

Manuscript

Colloidal nanostructures as building blocks for macroscopic thermoelectric materials with electron-crystal phonon-glass properties

Marcus Scheele[1], Niels Oeschler[2], Katrin Meier[2], Andreas Kornowski[1], Christian Klinke[1], and Horst Weller[1]

[1]University of Hamburg, Institute of Physical Chemistry, Grindelallee 117, 20146 Hamburg, Germany
[2]Max Planck Institute of Chemical Physics of Solids, Noethnitzer Strasse 40, 01187 Dresden, Germany

Abstract

We demonstrate the shape- and size-controlled synthesis of colloidal ~10 nm bismuth telluride nanoparticles stabilized by organic ligands in solution. Post-synthetic ligand exchange with oleic acid allows for a quick and simple ligand removal by consecutive washing with basic ammonia solution. Mild spark plasma sintering yields a macroscopic nanostructured bulk solid with nanograins unaltered in size and shape. We present the full thermoelectric characterization with an emphasis on the thermal properties of this material. It will be shown that thus prepared nanostructured bulk solids possess significantly altered physical properties typical for materials with high surface-to-volume-ratios. These alterations have the potential to lead to improved thermoelectric performances benefiting from their phonon-glass electron-crystal behavior.

Introduction

Fabrication methods of nanostructured bulk solids can generally be divided into top-down and bottom-up techniques. As an example for the former, ball-milling of macroscopic ingots to nanograins followed by hot-pressing has led to remarkable improvements in the thermoelectric figure of merit (ZT) of these materials.[18] Bottom-up techniques such as hydrothermal and wet-chemical methods have been exploited as an alternative to nanograin synthesis followed by sintering to macroscopic pellets.[55,108] To control the rate of crystal grain growth and stabilize the highly energetic surfaces of small nanograins, long-chained coordinating organic molecules such as thiols, carboxylic acids, or amines are added to the reaction mixture. These molecules, referred to in the following as ligands, play a key role in bottom-up synthesis and allow excellent control over shape, size, and size distribution of the nanograins. Since thermoelectric properties are known to depend strongly on these parameters for grains on the nanoscale, bottom-up nanograin synthesis offers exciting possibilities to designing high-performance thermoelectric materials.[13] PbSe nanograins obtained by wet-chemical synthesis were reported to show a remarkable increase in thermopower attributed to sharp spikes in the density of states.[27] However, a major draw-back in previous works was the often low electric conductivity in the final nanostructured bulk solids. This can immediately be understood when imagining the two component structure of individual nanograins obtained by wet-chemical synthesis: The inorganic, highly conductive nanograin core and the organic, insulating shell made of ligands protecting the core. As necessary as the presence of the ligands was throughout the reaction as deleterious it becomes to charge carrier transport when incorporated into the nanostructured bulk solid. In order to fabricate shape- and size-controlled nanostructured bulk solids with high electric conductivities it is mandatory to remove the ligands after the synthesis and before hot-pressing to pellets. Further, unprotected nanograins obtained after ligand removal possess very high surface energies and are prone to post-synthetic grain-growth during hot-pressing. Duration and temperature of the pressing procedure must therefore be kept to a minimum. In this respect, hot-pressing with the aid of a pulsed, high DC current, known as spark plasma sintering (SPS), is found to be an ideal technique. The sintering duration can be shortened to minutes and the overall temperature necessary for good compaction of the grains is usually significantly lower than with conventional, furnace driven systems.

As an example for the potential of the bottom-up approach, we will present the synthesis and thermoelectric properties of colloidal bismuth telluride nanoparticles.

Experiment

Bismuth telluride nanoparticles were synthesized following a previously developed protocol.[64] The as-prepared, 1-dodecanethiol stabilized nanoparticles were precipitated with ethanol and the supernatant removed after centrifugation. The black precipitate was mixed with a large excess of oleic acid (~3 mL, 90 %, Aldrich) and allowed to stir overnight on which a black suspension was formed. The supernatant was removed after short centrifugation and fresh oleic acid was added on which the mixture was allowed to stir for several hours. The supernatant was removed again after centrifugation and it was washed three times with hexane (analytical grade, Aldrich). The precipitate was suspended in a solution of NH_3 in methanol (2 mL, 7 N, Aldrich). After stirring overnight, the supernatant was removed after centrifugation (4500 rpm, 5 min) and it was washed two times with fresh NH_3 in methanol followed by three washing steps with hexane.

All solvents were removed and it was dried under vacuum overnight on which a fine black powder was obtained.

Typically, 100 mg of the powder kept under argon were loaded into a WC/Co die of 8.0 mm x 1.5 mm in area. The powder was pressed to a solid pellet of equal dimensions and approximately 1.5 mm in height by spark plasma sintering in a SPS-515 ET/M apparatus (Dr. Sinter®lab). For thermal conductivity measurements, 170 mg were loaded into a disk-shape die of 6 mm in diameter to obtain a tablet of bismuth telluride nanoparticles with 1.3 mm in height. On applying 340 MPa (for rectangular bars) or 530 MPa (for disks) pressure, the die containing the nanopowder was heated from 20 °C to 50 °C in 5.0 min with 10.0 min hold time by applying a DC current between 0 – 165 A and immediately allowed to cool down to room temperature. The obtained nanoparticle pellets were mechanically robust and silver-metallic in appearance.

Discussion

Imaging of nanostructure

In **Figure 1**, transmission and scanning electron microscopy (TEM and SEM) is applied to investigate the size and shape of individual nanocrystals. The 1-dodecanethiol stabilized bismuth telluride nanoparticles are well separated by their ligand shell and readily soluble in a wide range of organic solvents ($CHCl_3$, toluene, hexanes, etc.). The narrow size distribution is the consequence of well controlled nucleation and growth stages during the reaction. The size of nanocrystals can be controlled between 7 and 20 nm without significant broadening of size-distribution by changing the concentration of reactants. For a theoretical introduction the reader is referred to LaMer et al.[56] The shape of nanocrystals can be tuned from spheres to stars, platelets, and sheets by altering reaction conditions slightly (not shown here). Such a remarkable control over individual nanocrystals is unprecedented by top-down techniques and allows for exciting new possibilities to tune thermoelectric properties of these materials. For example, controlling the shape of bismuth telluride nanoparticles could be applied to benefit from the highly anisotropic, direction-dependent figure of merit.[73] Size-control allows studying the size effect on thermoelectric properties and utilizing recent theoretical predictions to improve the thermoelectric figure of merit.[28] A narrow size distribution is mandatory to enable efficient charge carrier transport between the nanograins and minimize charge carrier scattering.[57]

All of the afore mentioned advantages depend crucially on the presence of stabilizing organic ligands. In their absence, shape control disappears, size distribution broadens dramatically, and the tuning possibilities are lost. To allow for high electric conductivities, organic ligands must not be incorporated into the nanostructured bulk solid. Our ligand removal procedure is simple, at low-cost, and highly efficient (see transport properties further down).

As visible in SEM imaging, careful choice of SPS parameters allows compacting ligand-free nanoparticles to a dense pellet without significantly changing their size and shape.[64] Relative density of typical pellets is 80 %.

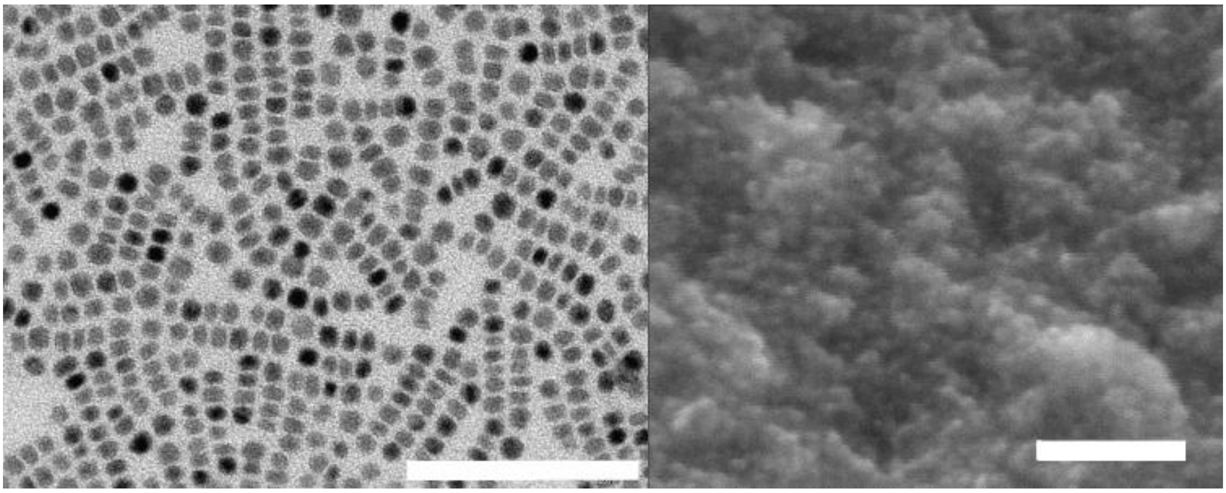

Figure C-1: Imaging of nanostructures. (**Left**) TEM image of 1-dodecanethiol stabilized bismuth telluride nanoparticles on amorphous carbon substrate. (**Right**) SEM image of ligand-free, SPS compacted bismuth telluride nanoparticles. Scale bars correspond to 100 nm.

Charge carrier transport

Electric conductivity (σ) of nanostructured bulk bismuth telluride solids is only slightly decreased with respect to bulk samples (**Figure 2**, **left**). This is the result of efficient ligand removal and purification of the nanocrystalline powder. Unlike bulk Bi_2Te_3, σ has a positive dependence on temperature (T) around room temperature. We attribute this to the effect of grain boundary potential barrier scattering:[22] Due to crystal defects and dangling-bonds, each nanograin in the nanostructured sample possesses a large density of trap-states. Such trap-states immobilize charge carriers at the grain surface meanwhile charging it up. Charged surfaces provide a potential barrier (EB) to charge carrier transport and lead to a changed σ(T) according to $\sigma(T) \sim T^{-1/2} \exp[-E_B/kT]$. Thus, for certain temperatures and magnitudes of EB, σ(T) can become positive regardless of its behavior in single crystals. We note that this shifts the maximum in the thermoelectric power factor to significantly higher temperatures as compared to bulk Bi_2Te_3.

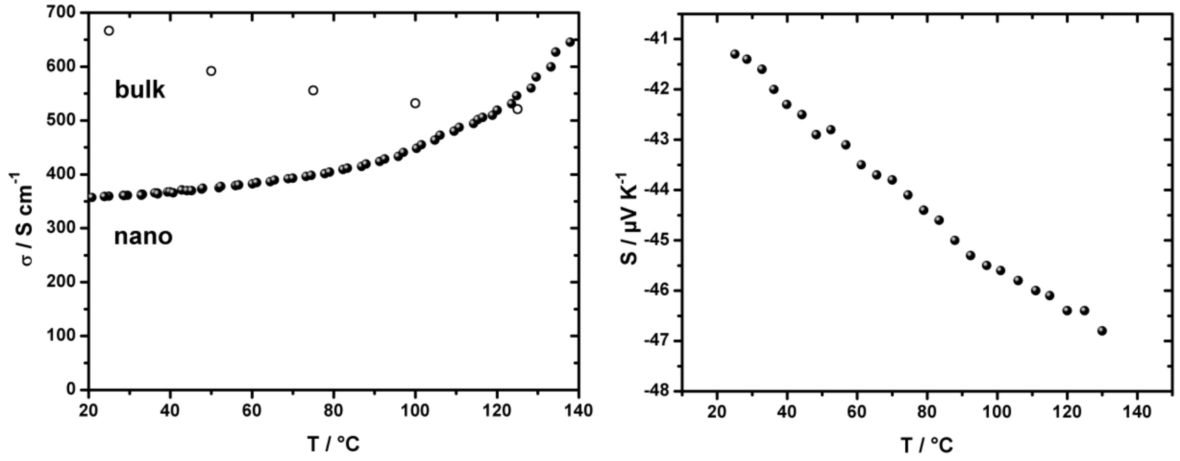

Figure C-2: Charge carrier transport. (**Left**) Electric conductivity of nanostructured (**full circles**) versus bulk (**open circles**) bismuth telluride.[58] (**Right**) Thermopower of nanostructured bismuth telluride bulk solid.

At present, the thermopower (S) (**Figure 2, right**) is significantly decreased compared to bulk Bi_2Te_3. This is the result of a non-optimized chemical composition and is subject to future work under way. According to Inductively Coupled Plasma Optical Emission Spectroscopy, the present material is tellurium deficient and is better described by the formula $BiTe_{1+x}$ rather than Bi_2Te_3. Chemical composition is known to have a large impact on S in bismuth tellurides.[49] Crystal defects may play an additional role in reducing S.[64]

Thermal transport

As displayed in Figure 3 (left), thermal transport (κ) is drastically inhibited in nanostructured bismuth telluride solids. This is attributed to a remarkable decrease in lattice thermal conductivity by as much as 80 % as compared to bulk bismuth telluride. To some degree, the low thermal conductivity is likely to be the result of porosity (P) in the sample. We account for this by applying a Maxwell-Eucken-type correction to derive the theoretical total thermal conductivity (κ_{corr}) of a sample with the same nanostructure but 100 % relative density by following

$\kappa_{corr} = \kappa \cdot \frac{1+P}{1-P}$. As a verification of this correction we refer to Chiritescu et al. who calculated the thermal conductivity of nanostructured Bi_2Te_3 with an average grain size of 15 nm within the assumptions of the Debye-Callaway model.[67] Their room temperature value is almost identical with our porosity corrected value implying that the scattering effect of the nanostructure is fully operative. The additional decrease of 0.2 W $m^{-1}K^{-1}$ in κ beyond the Debye-Callaway predicted value is therefore due to porosity.

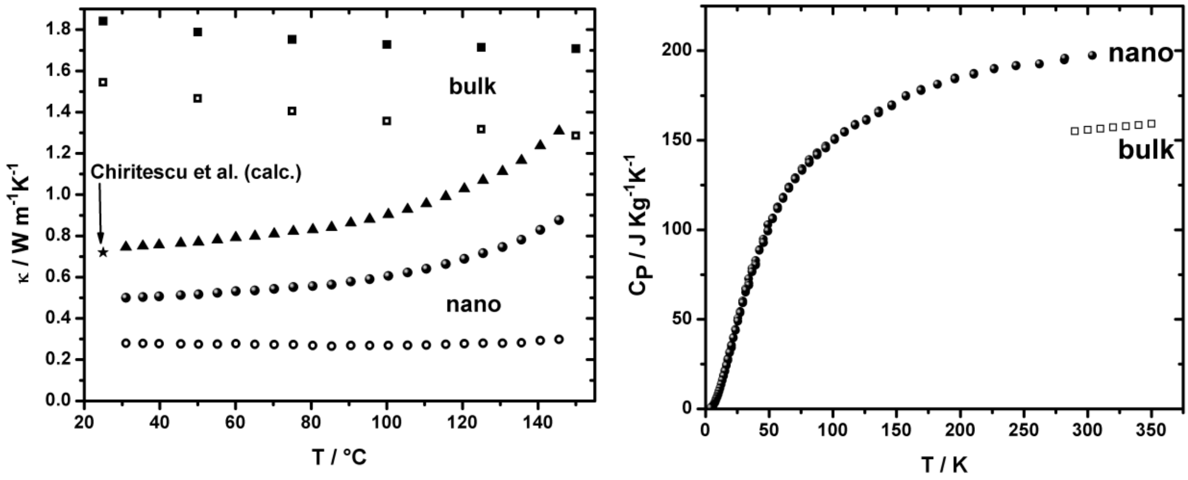

Figure C-3: Thermal transport. (**Left**) Thermal conductivity of nanostructured (**circles**) versus bulk (**squares**) bismuth telluride.[58] Lattice thermal conductivities (**open symbols**) were calculated according to Wiedemann-Franz assuming $L = 2.0 \cdot 10^{-8}\ V^2\ K^{-2}$. A correction for porosity in the nanostructured sample was applied to display the thermal conductivity of a theoretical sample with 100 % relative density (**triangles**). A calculated value for nanostructured bulk Bi_2Te_3 of 15-nm grain size was included for comparison (**stars**).[67] (**Right**) Specific heat of nanostructured (**circles**) versus bulk (**squares**) bismuth telluride.[59]

Another result of the nanostructure is a significantly increased specific heat capacity (C_P) as displayed in **Figure 3** (**right**). The increase by roughly 30 % is typical for highly granular systems and can be attributed to the large percentage of surface atoms which possess different vibrational energies compared to atoms inside the crystal.[72]

Results

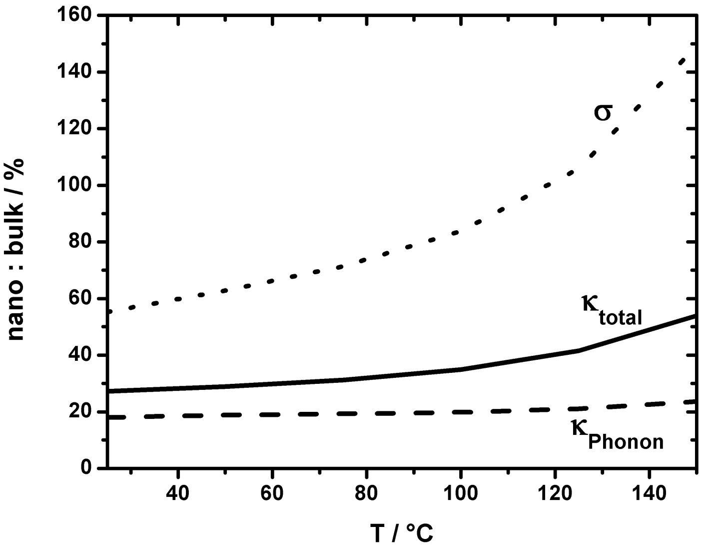

Figure C-4: Relative transport properties. The effect of nanostructuring is investigated by plotting the ratio of electric conductivity (**dotted**), total thermal conductivity (**solid**) and lattice thermal conductivity (**dashed**) of nanostructured bismuth telluride divided by the values for bulk bismuth telluride as a function of temperature.[58]

To sum up the results of this work, we plot the relative transport properties in Figure 4 by dividing the individual property measured for nanostructured bismuth telluride by the same property reported for bulk samples. For the whole temperature range investigated, relative σ is significantly higher than relative κ, implying that phonons are scattered to a higher degree than electrons. Thus, we have made a material with phonon-glass electron-crystal properties. Such materials have great potentials due lead to significantly enhanced ZT values. Due to the non-optimized chemical composition and the reduced thermopower, the current ZT is only about 0.1. Future work is under way to tune the thermopower towards the bulk value and benefit from the phonon-glass electron-crystal effect in this nanostructured material made by wet-chemistry.

Acknowledgements

We thank Igor Veremchuk for performing additional SPS experiments, Klaus-Georg Reinsberg for ICP-OES analysis and gratefully acknowledge a PhD grant by the *Studienstiftung des deutschen Volkes*.

Chapter D

ZT Enhancement in Solution-Grown $Sb_{(2-x)}Bi_xTe_3$ *Nanoplatelets*

Manuscript

ZT Enhancement in Solution-Grown $Sb_{(2-x)}Bi_xTe_3$ Nanoplatelets

Marcus Scheele[1,], Niels Oeschler[2], Igor Veremchuk[2], Klaus-Georg Reinsberg[3], Anna-Marlena Kreuziger[1], Andreas Kornowski[1], José Broekaert[3], Christian Klinke[1], and Horst Weller[1]*

[1]University of Hamburg, Institute of Physical Chemistry, Grindelallee 117, 20146 Hamburg, Germany

[2]Max Planck Institute of Chemical Physics of Solids, Noethnitzer Strasse 40, 01187 Dresden, Germany

[3]University of Hamburg, Institute of Inorganic and Applied Chemistry, Martin-Luther-King-Platz 6, 20146 Hamburg, Germany

We report a solution-processed, ligand supported synthesis of 15-20 nm thick $Sb_{(2-x)}Bi_xTe_3$ nanoplatelets. After complete ligand removal by a facile NH_3-based etching procedure, the platelets are spark plasma sintered to a p-type nanostructured bulk material with preserved crystal grain sizes. Due to this nanostructure, the total thermal conductivity is reduced by 60 % in combination with a reduction in electric conductivity of as low as 20 % as compared to the bulk material demonstrating the feasibility of the phonon-glass electron-crystal concept. An enhancement in the dimensionless thermoelectric figure of merit of up to 15 % over state-of-the-art bulk materials is achieved meanwhile shifting the maximum to significantly higher temperatures.

Introduction

Recently, Bi_2Te_3 based nanostructured materials have received great attention due to their outstanding thermoelectric properties. From the first reports in the 1950s until today, the dimensionless thermoelectric figure of merit (ZT) of such materials at room temperature has been improved threefold. From 0.5 for pure Bi_2Te_3 bulk samples over 1.14 for bulk $(Bi_2Te_3)_{0.25}(Sb_2Te_3)_{0.72}(Sb_2Se_3)_{0.03}$and 1.2 for nanostructured BiSbTe alloys to 1.56 for nanostructured $Sb_{1.52}Bi_{0.48}Te_3$ with “*coherent interfaces*”, advances in semiconductor manipulation have yielded impressive results in this ecologically highly promising field.[60,38,18,61] ZT is estimated to require a value of 3 to be competitive with conventional cooling devices and to open up novel pathways for efficient and greener power generation.

The record high efficiency of 2.4 was reported for molecular beam epitaxy engineered thin films of Bi_2Te_3/Sb_2Te_3 layers, which may be difficult to use in large-scale applications but convincingly demonstrated the potential for further improvements to come from nanostructured Bi_2Te_3 based materials.[42]

In order to fabricate such materials on a macroscopic scale, one conventionally applies high pressure and suitable temperatures to sinter a Bi_2Te_3 based nanopowder to a dense nanocomposite with preserved crystal grain boundaries. Such nanocomposites have been studied by the means of transmission electron microscopy (TEM), energy dispersive X-ray spectroscopy (EDXS) and scanning electron microscopy (SEM).[62,33] It is believed that the unique structural details in these materials such as laminated structure, coherent interfaces, nanoprecipitates with defect concentrations and broad size distribution of crystalline domains effect all three parameters of ZT, namely the thermopower, electric and thermal conductivity and can lead to an overall improvement of thermoelectric efficiency.

Synthetic strategies to Bi_2Te_3 based nanopowders can be divided into two approaches: (a) ligandless or (b) ligand supported nanograin growth. Advantages of the former are the absence of organic impurities and the good alloying possibilities by standard semiconductor manipulations. As a matter of this, the ligandless approach was more successful recently and all of the milestone achievements in enhancing ZT as cited above were due this strategy. Methods of choice are techniques like ball-milling of ingots and melt-spinning.[18,61] An instructive summary has been provided recently by Ren and co-workers.[83] However, it is found almost impossible to achieve a good size control and narrow size distribution of nanoparticles by this strategy. This is the major advantage of solution processed, ligand supported nanoparticle growth strategies. Significantly better size control as compared to ligandless approaches has been achieved for a variety of high performance thermoelectric materials including Bi_2Te_3 and $Sb_{(2-x)}Bi_xTe_3$.[33,63] Majumdar and co-workers have shown that self-assembled colloidal PbSe nanoparticles synthesized in solution show an enhanced thermopower due to sharp spikes in the density of states because of quantum confinement effects.[27] We have reported recently a procedure capable of completely removing the ligand sphere of formally organically protected nanocrystals.[64] Thus treated nanoparticles sintered to a macroscopic composite show the same electric conductivity as the bulk material. This tool in combination with the advances in solution processed nanotechnology opens up pathways to thermoelectric studies of nanocomposites with grain sizes where low-dimensional effects are really prominent, that is drastically below 100 nm. Only when size and size-distribution of nanoparticles are small, one can obtain detailed insight into the change in thermoelectric parameters due to the limited dimensions. In the recent past, a growing number of theoreticians have turned to modelling the thermoelectric properties of such nanogranular composites, including the thermoelectric coefficient and figure of merit, transport properties and the power factor.[51,28,65] Their results suggest that nanogranular materials not only display the easily understood decrease in lattice thermal conductivity but also alterations in transport properties which are not as straightforward to comprehend as the influence on phonon transport. For the on-going discussion to advance, new systems need to be designed to deliver experimental data for comparison with theoretical predictions. In this respect, ligand supported growth of nanostructures provides an additional tool to access new and complex thermoelectric materials which are difficult to obtain by conventional top-down approaches. Specifically, the synthesis of ultra-thin Bi_2Te_3-based nanostructures has received great attention owed to the quickly evolving field of topological insulators.[66] As such, these structures have been synthesized by the means of the elemental reactant technique, exfoliation and vapor-solid growth.[67] [68] [69] These techniques allow for much better control of the nanostructures' thickness than the top-down approaches mentioned above. However, the absolute yield is usually too low to fabricate macroscopic samples of it.

Here, we report the large scale synthesis of $Sb_{(2-x)}Bi_xTe_3$ nanoplatelets in solution, their purification from organic ligands, the fabrication of macroscopic nanocomposites and their full thermoelectric characterization.

Results and discussion

$Sb_{(2-x)}Bi_xTe_3$ nanoplatelets are synthesized similarly to a previously developed protocol for Bi_2Te_3 nanoparticles.[64] The acetates of Bi^{3+} and Sb^{3+} are treated with excess 1-dodecanethiol (DDT) under vacuum to remove acetic acid and form the metal thiolates which are easily soluble in organic media. Injecting the mild reducing agent oleylamine into this solution exclusively initiates the formation of a bismuth(0) species, referred to in the following as "*slow reduction*". Adding a solution of tellurium in trioctylphosphine (Te@TOP) within minutes after initiating the slow reduction triggers a much faster reduction by the more potent reducing agent trioctylphosphine (TOP). The metal(0) species formed during the "*fast reduction*" is unstable in the presence of the tellurium complex and reacts to the ternary antimony-bismuth-telluride compound. Shortly after beginning the fast reduction under these conditions, thin nanostructures only few nanometers in thickness of Sb-Bi-Te can be found, referred to in the following as "nanoflakes" (See supporting information, **Figure S1**). If kept at moderate temperatures (60 °C), the nanoflakes will combine to larger structures, referred to in the following as "nanosheets". During this process the thickness of the sheets does not change significantly. Over time, an increasing number of defined geometric features like sharpe edges, corners and even symmetric hexagons is observed. Typically, the dimensions of the final nanosheets are 50-200 nm across and up to 5 nm in thickness as estimated by X-ray powder diffraction (XRPD) measurements. By increasing the reaction temperature (90 °C *vs*. 60 °C), the thin and often porous nanosheets grow in thickness by the up-take of Sb_2Te_3 from the solution. The nanostructures resulting from this process are single-crystalline, 15 – 20 nm in thickness and will be referred to in the following as "nanoplatelets".

In **Figure 1**, transmission electron microscopy (TEM) reveals the shape of typical nanosheets **(1a)** and nanoplatelets **(1b)**. A high resolution (HR-TEM) image **(1c)** verifies the discontinuous nature of the nanosheets with the amorphous carbon substrate visible underneath. It is noteworthy that the whole sheet appears to be almost single-crystalline which is further studied in **Figure 1e**. Here, the fast Fourier transformed (FFT) of the image displays a clear atomic ordering, however with a slight directional misalignment of the individual crystalline domains. From this, it is inferred that the porous nanosheets evolve from nanoflakes throughout the course of the reaction. During this process, the individual nanoflakes have to align perfectly in one crystalline direction to eventually form a single crystal. The crystal depicted in the inset of Figure **(1c)** is therefore an intermediate stage in this process. In contrast, the thicker nanoplatelets are continuous and perfectly single-crystalline (see **Figure 1d)**. They are believed to develop from nanosheets of similar diameter by growing in thickness.

As visible in the FFT of the HR-TEM image **(1 e+ f)**, the direction of growth of the sheets and platelets is in the a-b-plane, that is along the [110] direction ([11-20] in Bravais annotation). This is a typical behaviour of Bi_2Te_3 and Sb_2Te_3 owed to its highly anisotropic crystal structure.[107,70] For the evolution of platelets from sheets, an additional growth in the c-direction is required. The rate of this growth is too low at 60 °C so that even after 4 days of reaction only sheets are obtained. Increasing the temperature to 90 °C initiates growth in the c-direction and begins the formation of nanoplatelets.

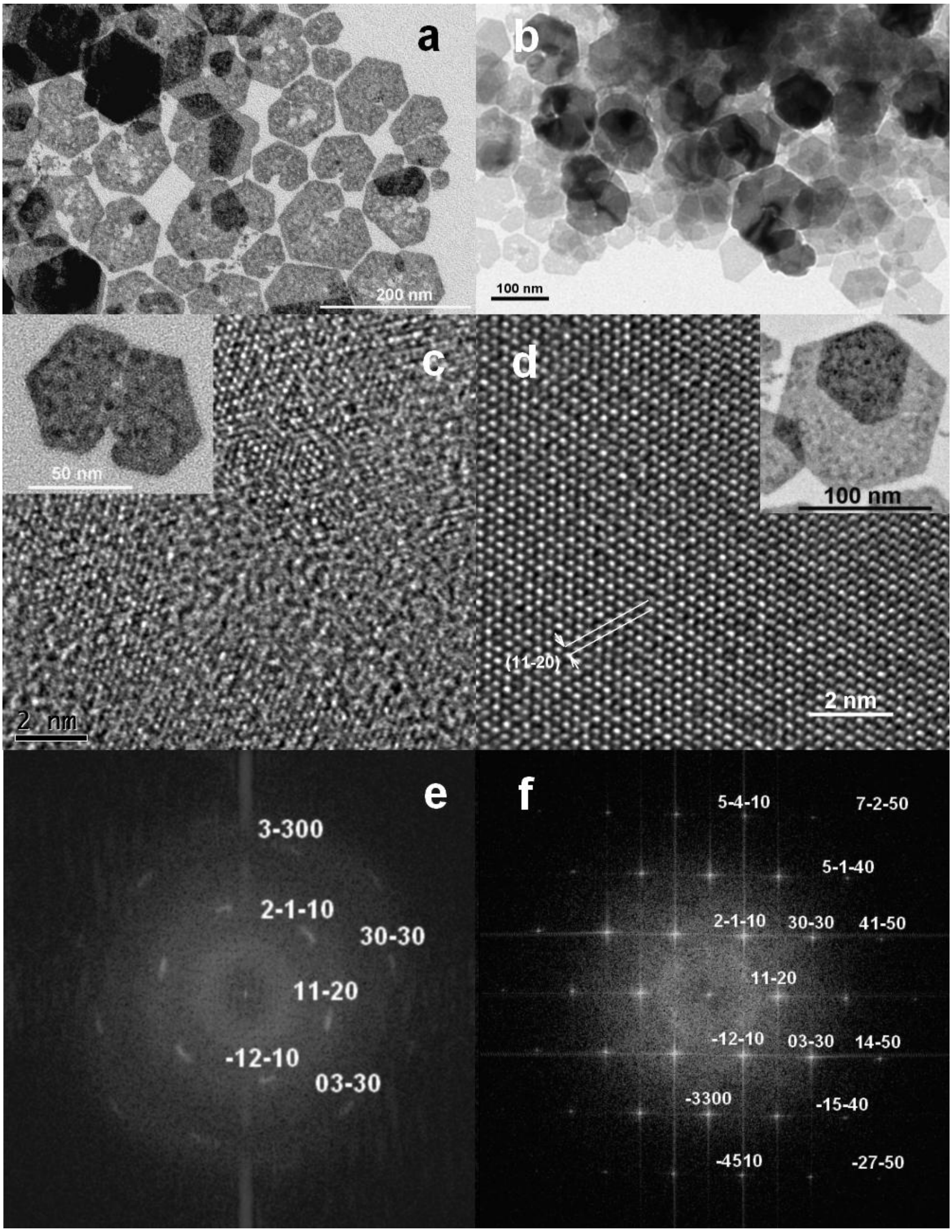

Figure D-1: TEM images of $Sb_{(2-x)}Bi_xTe_3$ nanosheets (**a**) and nanoplatelets (**b**). HR-TEM images of individual (*see inset*) nanosheets (**c**) and nanoplatelets (**d**). The indicated lattice spacing is 2.15 Å which corresponds to the spacing of (11-20) planes. Fast Fourier transformed of the HR-TEM images of nanosheets (**e**) and nanoplatelets (**f**). In each case, the direction of view is [0001].

Compositional analysis is shown in **Figure 2** by the means of XRPD, energy dispersive X-ray spectroscopy (EDXS) and inductively plasma coupled optical emission spectroscopy (ICP-OES). The XRPD **(Figure 2 left)** of $Sb_{(2-x)}Bi_xTe_3$ nanoplatelets reveals a single-phase product with slightly broadened reflections typical for crystals with nanoscalic dimensions. Position and intensity of the reflections can be attributed to an intermediate of Bi_2Te_3 and Sb_2Te_3 with a Sb:Bi ratio much larger than unity. Lattice constants for a hexagonal unit cell were determined to a = 4.268 Å and c = 30.40 Å which compares to 4.260 Å/30.45 Å for pure Sb_2Te_3 and 4.38 Å/30.48 Å for pure Bi_2Te_3. For comparison, an XRPD of nanosheets is displayed in the SI unit (**Figure S2**) revealing lattice constants of a = 4.272 Å and c = 30.50 Å.

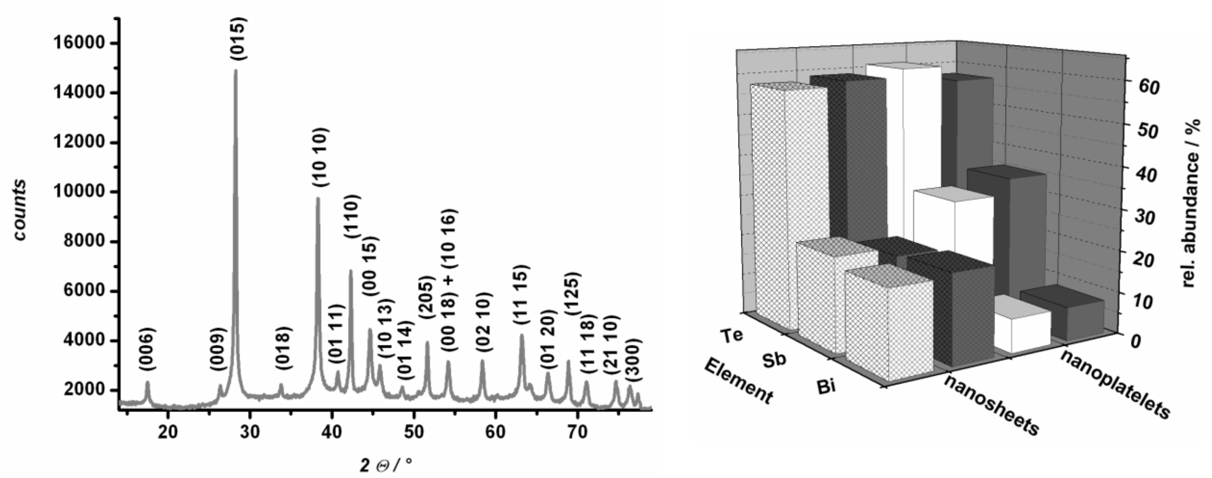

Figure D-2: (Left) XRPD of $Sb_{(2-x)}Bi_xTe_3$ nanoplatelets with Sb:Bi ≈ 4:1. Indexing according to space group R-*3m* (166). (**Right**) Elemental analysis of $Sb_{(2-x)}Bi_xTe_3$ nanosheets (*hatched*) and nanoplatelets (*blank*). Individual nanocrystals were analyzed by EDXS (*light*), large quantities of nanocrystal powder were analyzed by ICP-OES (*dark*).

EDXS and ICP-OES analysis **(Figure 2 right)** reveal antimony, bismuth and tellurium as the main constituting elements in the nanosheets and nanoplatelets. When comparing the quantitative elemental analysis of nanosheets and nanoplatelets it becomes evident that the $Sb_{(2-x)}Bi_xTe_3$ sheets have a much larger bismuth content (Sb:Bi ≈ 1:1, $Sb_{1.0}Bi_{1.0}Te_{3.0}$) than the platelets (Sb:Bi ≈ 4:1, $Sb_{1.7}Bi_{0.4}Te_{3.0}$). Note that optimized, bulk $Sb_{(2-x)}Bi_xTe_3$ usually has a Sb:Bi ratio of 3:1 ($Sb_{1.5}Bi_{0.5}Te_3$).[18] In both of the two structures the relative abundance of tellurium is always 57-59 at.-%. The analytical results of individual nanosheets and platelets obtained by EDXS (see also **Figure S3** in the SI unit) are in good agreement with the results of ICP-OES analysis of the same material subsequent to wet chemical digestion showing the homogeneity in chemical composition of the individual nanocrystals.

All organic residues are removed from the inorganic nanosheets or nanoplatelets to allow for high electric conductivities. Where solvents can be effectively withdrawn by multiple washing steps, the separation from the stabilizing agent DDT is realized by a modified procedure similar to a previously developed protocol.[64] As the only alteration, after ligand exchange with oleic acid we apply a methanolic NH_3 solution rather than hydrazine hydrate.

The advantage is the non-reductive nature of NH_3 in comparison to the powerful reducing agent hydrazine. This way, an unwanted partial reduction of the nanosheets during the washing procedure can be excluded. After drying the inorganic material under vacuum, we obtain a dark-grey nanopowder. According to XRPD, this procedure has no significant impact on the crystalline phase of the nanomaterial (see SI unit, **Figure S4**).

To fabricate a nanostructured bulk material, this powder is spark plasma sintered (SPS) to a macroscopic pellet. Pellets of $Sb_{(2-x)}Bi_xTe_3$ nanosheets or nanoplatelets are silver-metallic in appearance with a density of 5.73 ± 0.10 g cm^{-3} (85 % of theoretical density) under the conditions specified in the experimental section and SI unit (**Figure S5, S6 and S7**). To achieve larger densities towards 100 % of the theoretical value, significantly higher sintering temperatures and duration are required which resulted in unwanted grain growth during compaction.

In the following, we will focus on the thermoelectric properties of $Sb_{1.7}Bi_{0.4}Te_{3.0}$ nanoplatelets.

In **Figure 3**, the fine structure of the sintered pellets and its impact on the thermal conductivity is investigated. As displayed by SEM imaging in **Figure 3a**, the shape of individual nanoplatelets is preserved in the final pellets yielding a highly polycrystalline, layered material. We compare our thermal conductivity results with state-of-the-art macrocrystalline, bulk $Sb_{1.5}Bi_{0.5}T3_{3.0}$.[18] (Note: This reference mainly reported on nanostructured $Sb_{1.5}Bi_{0.5}Te_{3.0}$. In addition, it presented the complete thermoelectric characterization of a macrocrystalline sample for comparison. The values reproduced in the present work are those of the macrocrystalline sample.)

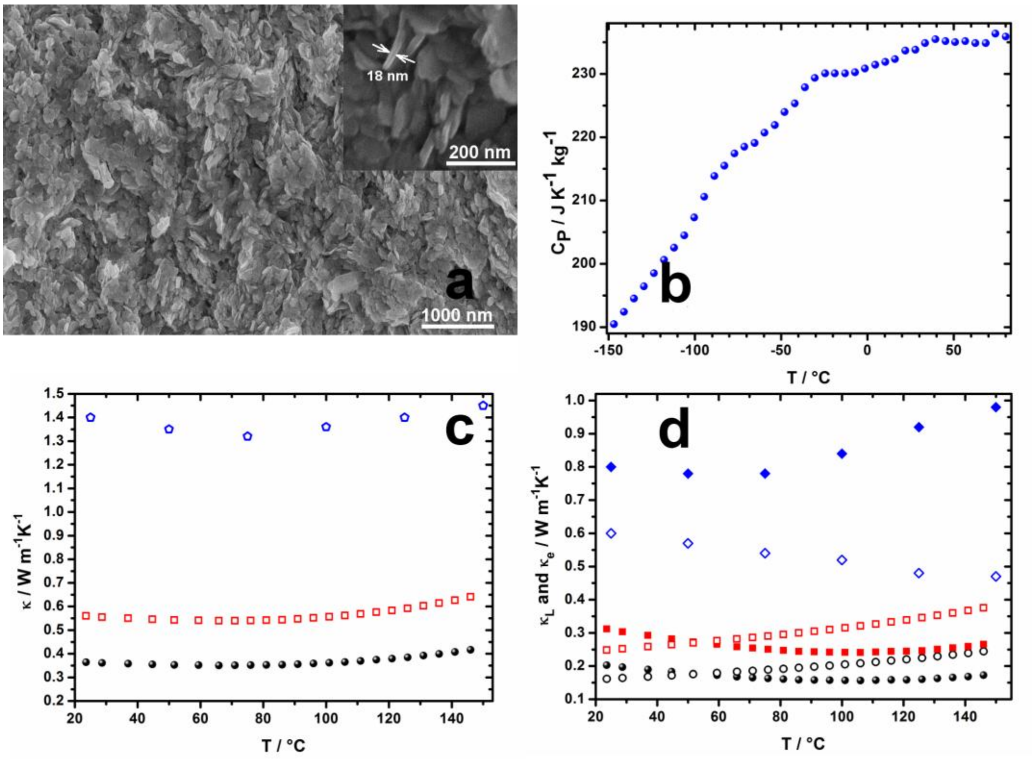

Figure D-3: (a) SEM image of a spark plasma sintered pellet of $Sb_{1.7}Bi_{0.4}Te_{3.0}$ nanoplatelets. The inset contains a side view on individual nanoplatelets revealing their approximate thickness. (**b**) Specific heat capacity of the nanoplatelet. (**c**) Total thermal conductivity of nanoplatelets uncorrected (*closed circles*), corrected for porosity (*open squares*) and of a $Sb_{1.5}Bi_{0.5}Te_{3.0}$ bulk ingot taken from reference 18 (*open diamonds*). (**d**) Lattice (κ_L, *closed*) and electronic (κ_e, *open*) thermal conductivity of nanoplatelets uncorrected (*circles*), corrected for porosity (*squares*) and bulk ingots (*diamonds*).

To calculate the total thermal conductivity (κ) from Laserflash measurements, we measured the specific heat (C_P, **Figure 3b)** repeatedly of several samples and on using three different measurement systems (Physical Property Measurement System by Quantum Design; Differential Scanning Calorimeter by Netzsch and Linseis). The deviation of all measurements was less than 5 %. At 300 K we obtain $C_P = 235$ J kg^{-1} K^{-1}. Note that this is almost 25 % higher than the Dulong-Petit limit for bulk materials. Such a deviation is typically observed for nanostructures and has been attributed to the large amount of surface atoms as compared to the total volume of these structures.[71,113,72,109] With this, an average density (ρ) of 5.73 g cm^{-3} and the thermal diffusivity results (D_t) we calculate the total thermal conductivity following the equation:

$$\kappa = D_t\ \rho\ C_P$$

(67)

When measuring the transport properties of Bi_2Te_3-based compounds, great care must be taken about the individual measurement directions relative to the crystal's orientation. As Fleurial *et al.* have worked out, the anisotropy in thermal and electric transport between the a-b-plane and the c-axis of single-crystalline Bi_2Te_3 is 2 to 2.5.[73] A similar degree of transport anisotropy can be expected for single-crystalline $SbBiTe_3$. In pressed pellets of $SbBiTe_3$ nanoparticles, transport anisotropy depends on the degree of ordering of the individual nanocrystals in the pellet. As Ma *et al.* have shown, the random orientation of nanocrystals during hot-pressing can decrease transport anisotropy in nanostructured bulk $SbBiTe_3$ to less than 5 %.[74] For the material presented in this work, we determined a temperature dependent anisotropy in the thermal conductivity of 8 to 18 % with the lower thermal conductivity in the c-direction. (For details see Supporting information, **Figure S8**.) This anisotropy has been taken into account for all thermal conductivity measurements discussed below.

To allow a quantitative comparison of transport properties with 100 % dense, bulk samples, it is important to account for the porosity of about 15 % in the nanostructured samples presented in this work. As several groups have reported, porosity decreases thermal conductivity and electric conductivity alike.[123,84] Where the effect of porosity on ZT is usually small if not negligible, individual transport parameters must be corrected for porosity in order to judge the effect of nanostructuring alone.[123] To do so, we follow Adachi *et al.* by using a Maxwell-Eucken expression:[120]

$$x_P = x_0 \cdot \frac{1-P}{1+\beta P}$$

(68)

where x is either the thermal or the electric conductivity, x_P is the transport property in the porous medium, x_0 is the same property in the 100 % dense medium, P is the degree of porosity (a fraction between 0 and 1) and β an empirical parameter describing the shape of the pores. In the following, we set P to 0.15 and β to 2.0 which is a fair estimate related to similar works reported in literature.[120] Thus, the porosity in the material presented is estimated to account for a reduction in both, thermal and electric conductivity, to 65 % of the theoretical value to be expected for an absolutely dense sample. Comparisons with other models accounting for the effects of porosity (*e.g.* the percolation model) verify this assumption to be very reasonable.[75,76] To display the pure effect of nanostructuring on the transport properties, we will use only the porosity corrected values in the following discussion. In **Figures 3** and **4** we prefer to show both, the uncorrected and corrected measurements, for clarity.

The qualitative behaviour of κ(T) of the pellets of nanoplatelets **(Figure 3c)** is similar to the bulk material in so far that the variation over the measurement range from 25° C to 145 °C is less than 10 % with a minimum at 80 °C. With 0.56 W $m^{-1}K^{-1}$ at 300 K, κ is 60 % lower than that of a comparable bulk material.[18] As discussed below, some of this decrease results from a simultaneous decrease in electric conductivity (σ) (see **Figure 4**) which overall has no effect on the thermoelectric figure of merit due to the Wiedemann-Franz law. Therefore, a more suitable measure to judge the potential of our material for improved thermoelectrics is the lattice part (κ_L) of the thermal conductivity. To calculate κ_L at a given temperature (T), we follow Tritt and co-workers and use $L = 2.0 \cdot 10^{-8}\ V^2\ K^{-2}$ which is accepted to be the appropriate value of the Lorentz number for heavily degenerated semiconductors.

$$\kappa_L = \kappa - \kappa_e = \kappa - L\,\sigma\,T$$

(69)

With $\kappa_L = 0.31$ W m^{-1} K^{-1} at 300 K (**Figure 3d**), the decrease in phononic heat transport is again 60 % with reference to the bulk material. It is worth mentioning that this value for κ_L is in excellent agreement with similar attempts to reduce phononic transport *via* nanostructuring by other groups.[18,61] Poudel *et al.* reported $\kappa_L = 0.34$ $Wm^{-1}K^{-1}$ and Xie *et al.* showed $\kappa_L = 0.26$ $Wm^{-1}K^{-1}$ (uncorrected for porosity of 4.5 %).

Another important aspect in **Figure 3d** is the different behaviour of $\kappa_L(T)$ and $\kappa_e(T)$. At room temperature, heat transport in the nanoplatelets is dominated by lattice vibrations, that is, $\kappa_L > \kappa_e$. With increasing T, this is reversed to $\kappa_L < \kappa_e$ due to improved electric transport. Quite the opposite behaviour is known about bulk $Sb_{1.5}Bi_{0.5}Te_3$ where κ_e is always smaller than κ_L in this temperature regime.

In **Figure 4,** we display our σ (**4a**) and thermopower (S, **4b**) measurements, combine it to the power factor (σS^2, **4c**) and calculate the dimensionless figure of merit (ZT, **4d**) according to

$$ZT = \frac{\sigma\,S^2}{\kappa}\,T.$$

(70)

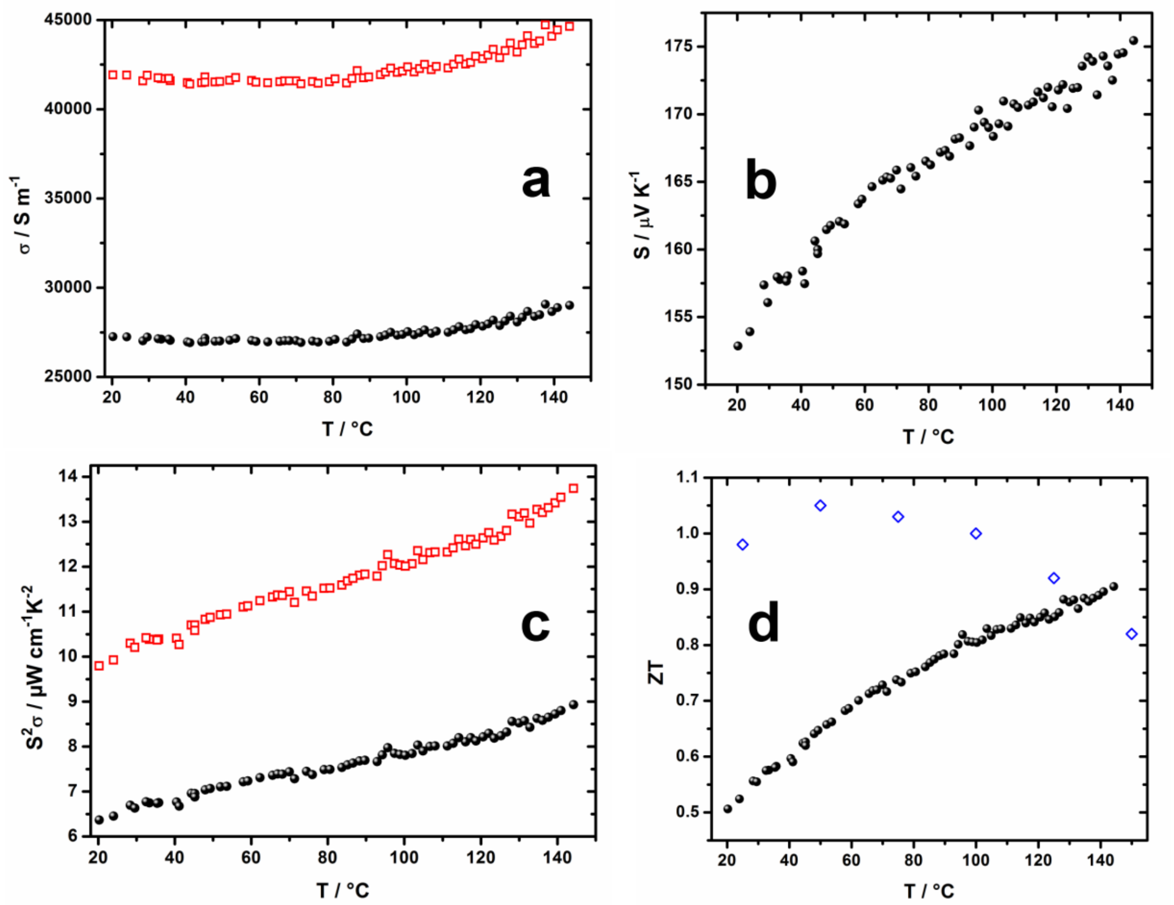

Figure D-4: (a) Electric conductivity, (**b**) thermopower, (**c**) power factor and (**d**) dimensionless figure of merit of a pellet of $Sb_{1.7}Bi_{0.4}Te_{3.0}$ nanoplatelets uncorrected (*closed circles*) and corrected for porosity (*open squares*). For comparison, the figure of merit of bulk $Sb_{1.5}Bi_{0.5}Te_{3.0}$ ingots is displayed (*open diamonds*).[18]

At room temperature, σ is decreased to 40 % of the bulk value which is the result of electron scattering at crystal grain boundaries. The large surface-to-volume ratio of nanograins results in high trap-state densities at each grain boundary caused by defects and dangling bonds. These trap-states immobilize charge carriers, leading to a reduced, effective mobility as compared to single crystals.[23] Further, the grain boundaries become electrically charged and provide a grain boundary potential barrier to electric transport.[77] In contrast to bulk $Sb_{1.5}Bi_{0.5}Te_3$, the pellets of nanoplatelets show a positive $\Delta\sigma/\Delta T$ ratio. This behaviour has recently been predicted by Nolas and co-workers for nanostructured materials where transport properties are dominated by *grain boundary potential scattering* in combination with phonon scattering.[22] At not too low temperatures, electric transport across the grain boundaries can be described by thermionic emission with $\sigma(T) \sim T^{-1/2} \exp[-E_B/kT]$ where E_B is the height of the grain boundary potential barrier. Thus, for certain temperatures and grain boundary potential barriers, $\Delta\sigma/\Delta T$ can become positive. This is an important difference to bulk $Sb_{1.5}Bi_{0.5}Te_3$ where the negative Δσ/ΔT ratio forces a maximum in ZT at 50 °C preventing an efficient application at significantly higher temperatures.

The positive thermopower (**Figure 4b**) indicates p-type behaviour in accordance with other $Sb_{1.5}Bi_{0.5}Te_3$ materials. The magnitude of, at best, 175 $\mu V\ K^{-1}$ is lower than that of comparable materials by other groups which can reach up to 220 $\mu V\ K^{-1}$. Like no other thermoelectric parameter, S varies strongly with the chemical composition. For example, for the nanosheets displayed in **Figure 1a,c,e** with a composition of $Sb_{1.0}Bi_{1.0}Te_{3.0}$ (see **Figure 2b**), we find a thermopower of merely 30 $\mu V\ K^{-1}$. We note that the composition of the nanoplatelets is with $Sb_{1.7}Bi_{0.4}Te_{3.0}$ too rich in antimony to fully compete with the optimized $Sb_{1.5}Bi_{0.5}Te_{3.0}$ samples applied in other works showing the best thermopower values. We believe that further optimization of our synthesis towards this ideal chemical composition will also lead to thermopower values of up to 220 $\mu V\ K^{-1}$. The precondition that the thermopower of nanostructured materials can be at least as high as in single crystals has been verified by several other groups already.[78,79,80,44]

The combination of the two parameters to the power factor (σS^2, **4c**) leads to an unusual temperature dependence. In bulk samples, σS^2 decreases with T at not too low temperatures owing to the negative Δσ/ΔT ratio. In contrast for the material in this work, $\sigma S^2(T)$ increases with temperature since Δσ/ΔT is positive.

Consequently, ZT(T) (**Figure 4d**) also increases with temperature. Starting with a moderate $ZT_{25\,°C} = 0.5$, at the highest measurement temperature we find $ZT_{145\,°C} = 0.9$ which is 15 % larger than that of a comparable bulk material. A maximum in ZT can be estimated to be found significantly above 145 °C when thermopower begins to be depleted by bipolar conduction and other effects. This is in agreement with other reports which translated the maximum in ZT of bulk $SbBiTe_3$ at 50 °C to about 100 °C *via* nanostructuring.[18, 74, 78] The present work demonstrates the continuation of this trend probably due to the introduction of larger *grain boundary potential barriers* which has been shown to drastically alter electron transport. This needs to be verified in the future *via* Hall mobility measurements.

In **Figure 5 (left)**, the reason for the enhanced thermoelectric efficiency is summarized. By fitting the experimental data on the transport properties of bulk and nanostructured $Sb_{(2-x)}Bi_xTe_3$ from **Figures 3c, d and 4a**, we plot the relative reduction of σ, κ and κ_L as a function of T resulting from the material's nanostructure. Over the entire temperature range, the reduction in κ is larger than the reduction in σ. As mentioned above, this is the key requirement for designing more efficient thermoelectric materials.

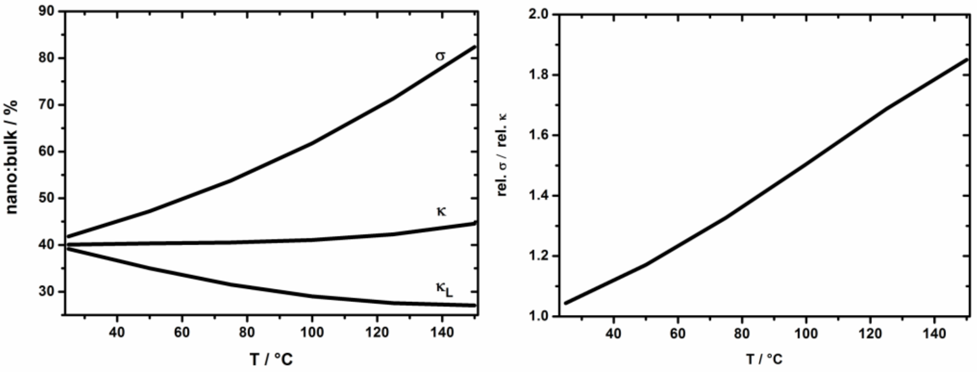

Figure D-5: (Left) Relative decrease of transport parameters of a pellet of $Sb_{1.7}Bi_{0.4}Te_{3.0}$ nanoplatelets as compared to bulk $Sb_{1.5}Bi_{0.5}Te_{3.0}$ ingots. (**Right**) "PGEC-factor" (the ratio of relative electric to total thermal conductivity) of $Sb_{1.7}Bi_{0.4}Te_{3.0}$ nanoplatelets.

It is noteworthy that the relative reduction of κ is with 60 % practically constant over the entire temperature regime. This is the result of the increased relative electric conductivity in combination with a simultaneous decrease in the relative lattice thermal conductivity. Materials with this behaviour are often referred to as "*phonon-glass electron-crystals*" (PGEC), meaning materials with good charge carrier but poor phonon transport.

In **Figure 5 (right)** we introduce the temperature dependent "PGEC-factor" defined as the ratio of the relative electric to total thermal conductivity compared to the bulk state. For the pellets of $Sb_{1.7}Bi_{0.4}Te_{3.0}$ nanoplatelets in this communication, the PGEC-factor starts at almost unity at room temperature but increases quickly to 1.8 at 140 °C. Provided the thermopower can be improved to the bulk value by adjusting the chemical composition to $Sb_{1.5}Bi_{0.5}Te_{3.0}$, the PGEC-factor is a direct measure ($ZT_{nano} = ZT_{bulk}$ x PGEC-factor) for the expected improvement in ZT as compared to the bulk material. This way, ZT = 1.5 is within reach.

Conclusion

We have demonstrated the applicability of ligand supported, bottom-up synthesized $Sb_{(2-x)}Bi_xTe_3$ nanoplatelets for highly efficient, macroscopic, p-type thermoelectric materials. The enhancement in ZT is achieved by the *phonon-glass electron-crystal* effect which describes the preferential scattering of phonons as compared to electrons by the nanostructure. The key to this property is a reduction in the lattice (or phononic) thermal conductivity leading to an enhancement in ZT by up to 15 % as compared to comparable bulk materials. Future adjustments of the chemical composition hold for an enhancement of up to 80 %. The maximum in ZT is shifted to larger temperatures which seems to be a direct consequence of the nanostructure.

Methods

All manipulations were carried out under an inert atmosphere using standard Schlenck techniques if not stated otherwise.

(I) *Preparation of a 0.500 M solution of tellurium in TOP (Te@TOP)*

In a glovebox, tellurium (1.276 g, 10.00 mmol, 99.999 %, Chempur) and tetradecylphosphonic acid (102 mg, Alfa Aesar) were suspended in distilled TOP (20.0 mL, 90 %, Merck) under stirring. It was heated stepwise to 230 °C from room temperature by increasing the temperature by approximately 50 °C every thirty minutes. The final temperature was kept until a completely transparent, orange solution was obtained which turned to bright-yellow on cooling to room temperature. The solution was stored in the glovebox.

(II) *Synthesis of $Sb_{1.0}Bi_{1.0}Te_{3.0}$ nanosheets*

In a typical synthesis, bismuth acetate (0.045 g, 0.12 mmol, 99 % Aldrich) and antimony acetate (0.323 g, 1.08 mmol, 99 % Aldrich) were mixed with 1-dodecanethiol (13.3 mL, 98% Aldrich) and heated to 45 °C for 45 min under vacuum on which a transparent, yellow solution was obtained. The flask was flooded with nitrogen, set to ambient pressure and it was heated to 60 °C on which oleylamine (26.7 mL, 70 %, Aldrich) was quickly added under stirring (referred to as "*slow reduction*" in the main body of the paper). After three minutes when the solution had visibly darkened, 3.6 mL of (**I**) were injected under vigorous stiring (referred to as "*fast reduction*" in the main body of the paper). After 24 h the as prepared $Sb_{1.0}Bi_{1.0}Te_{3.0}$ nanosheets were ready for further manipulations.

(III) *Synthesis of $Sb_{1.7}Bi_{0.4}Te_{3.0}$ nanoplatelets*

The amounts and procedure were identical to **(II)** with the only alteration being the reaction temperature which was 90 °C instead of 60 °C.

(IV) *Purification of $Sb_{(2-x)}Bi_xTe_3$ nanosheets or nanoplatelets for characterization*

A fraction of the dark-grey suspension obtained under **(II)** or **(III)** was mixed with ethanol (25 vol-%, analytical grade, Fluka) and centrifuged at 4500 rpm for 5 min. The light yellow supernatant was removed under nitrogen and the almost black precipitate suspended in a few drops of chloroform (analytical grade, Fluka) on which the washing cycle was repeated two more times. The purified nanosheets or nanoplatelets should be stored in the absence of oxygen to prevent aging.

(V) *Ligand removal from $Sb_{(2-x)}Bi_xTe_3$ nanosheets or nanoplatelets*

The purified **(II)** or **(III)** were precipitated again with ethanol and the supernatant removed after centrifugation. The black precipitate was mixed with a large excess of oleic acid (~3 mL, 90 %, Aldrich) and allowed to stir overnight on which a black suspension was formed. The supernatant was removed after short centrifugation and fresh oleic acid was added on which the mixture was allowed to stir for several hours. The supernatant was removed again after centrifugation and it was washed three times with hexane (analytical grade, Aldrich). The precipitate was suspended in a solution of NH_3 in methanol (2 mL, 7 mol L^{-1}, Aldrich). After stirring overnight, the supernatant was removed after centrifugation (4500 rpm, 5 min) and it was washed two times with fresh NH_3 in methanol followed by three washing steps with hexane. All solvents were removed and it was dried under vacuum overnight on which a fine black powder was obtained. Typically, the starting amounts specified under **(II)** yield approximately 100 mg of $Sb_{1.0}Bi_{1.0}Te_{3.0}$ nanosheets and 180 mg of $Sb_{1.7}Bi_{0.4}Te_{3.0}$ nanoplatelets for (**III),** respectively.

(VI) *Compaction of $Sb_{(2-x)}Bi_xTe_3$ nanoplatelett pellets by spark plasma sintering*

Typically, 95 mg of **(V)** kept under argon were loaded into a WC/Co die of 8.0 mm x 1.5 mm in area. The powder was pressed to a solid pellet of equal dimensions and approximately 1.4 mm in height by spark plasma sintering in a SPS-515 ET/M apparatus (Dr. Sinter®lab). For thermal conductivity measurements, 165 mg of **(V)** were loaded into a disk-shape die of 6 mm in diameter to obtain a tablet of $Sb_{(2-x)}Bi_xTe_3$ nanosheets with 1.3 mm in height. On applying 340 MPa (for rectangular bars) or 530 MPa (for disks) pressure, the die containing the nanopowder was heated from 20 °C to 50 °C in 5.0 min with 10.0 min hold time by applying a DC current between 0 – 165 A and immediately allowed to cool down to room temperature. The obtained $Sb_{(2-x)}Bi_xTe_3$ nanosheet pellets were mechanically robust and silver-metallic in appearance.

(HR-)TEM imaging was performed with a JEOL JEM 2200 FS (UHR) with CESCOR and CETCOR corrector at an acceleration voltage of 200 kV or a JEM-Jeol-1011 microscope at 100 kV with a CCD camera. SEM images were obtained on a LEO1550 scanning electron microscope with a spatial resolution of ~ 1 nm. XRPDs were recorded using a Philipps X`Pert-diffractometer with Bragg-Brentano-geometry on applying copper-K_α radiation (λ = 154.178 pm, U = 45 kV; I = 40 mA).

For measurements of the thermopower and resistivity a ZEM-3 apparatus (ULVAC-RIKO) was applied under a low-pressure helium atmosphere. The thermopower was determined by a static dc method where the resistivity was simultaneously measured by a four-terminal set-up.

The specific heat was measured by a relaxation technique in a Physical Property Measurement System by Quantum Design. A heat pulse of 2% of the bath temperature has been applied and repeated 3 times at each temperature.

Thermal diffusivity measurements were recorded with a Netzsch LFA-441 and a Netzsch LFA-457 Microflash with a Pyroceram standard for calibration.

ICP-OES analysis was performed with a Spectro Ciros CCD (Spectro Analytical Instruments) subsequent to powder sample digestion in a microwave assisted sample decomposition system (MARS 5, CEM Corporation) with a mixture of 20 % nitric acid and tartaric acid (L(+)-tartaric acid, p.a., 99.5 %, Sigma-Aldrich). The latter proved necessary as complexing agent to overcome the formation of insoluble Sb_2O_3. The bismuth, antimony and tellurium contents were determined by calibration with matrix matched solutions produced form ICP-standard solutions (1000 mg L^{-1} Bi, $Bi(NO_3)_3$ in HNO_3 2-3 %, Merck, 1000 mg L^{-1} Sb, Sb_2O_3 in HCl 7 %, Merck, 1000 mg L^{-1} Te, H_6TeO_6 in HNO_3 2-3 %, Merck). The relative errors of the analysis by ICP-OES were < 3.7 %.

Acknowledgements

We thank Katrin Meier for help with SPS experiments, William Töllner for help with DSC measurements and Michael Baitinger for fruitful discussions. A PhD-grant by the *Studienstiftung des deutschen Volkes* is gratefully acknowledged.

Supporting Information Available: TEM image of nanoflakes (**S1**). XRPD of $Sb_{1.0}Bi_{1.0}Te_{3.0}$ nanosheets (**S2**). EDX spectrum of $Sb_{1.7}Bi_{0.4}Te_{3.0}$ nanoplatelets (**S3**). XRPD of $Sb_{1.7}Bi_{0.4}Te_{3.0}$ nanoplatelets before and after ligand exchange (**S4**). Temperature-time-profile of SPS experiments (**S5**). Photograph of nanostructured bulk samples (**S6**) and XRPD after SPS sample fabrication (**S7**). Investigation of anisotropy in structure and thermal transport (**S8**). This material is available free of charge *via* the Internet at http://pubs.acs.org.

Supporting Information

ZT Enhancement in Solution-Grown $Sb_{(2-x)}Bi_xTe_3$ Nanoplatelets

Marcus Scheele[1,*], *Niels Oeschler*[2], *Igor Veremchuk*[2], *Klaus-Georg Reinsberg*[3], *Anna-Marlena Kreuziger*[1], *Andreas Kornowski*[1], *José Broekaert*[3], *Christian Klinke*[1], *and Horst Weller*[1]

[1]University of Hamburg, Institute of Physical Chemistry, Grindelallee 117, 20146 Hamburg, Germany

[2]Max Planck Institute of Chemical Physics of Solids, Noethnitzer Strasse 40, 01187 Dresden, Germany

[3]University of Hamburg, Institute of Inorganic and Applied Chemistry, Martin-Luther-King-Platz 6, 20146 Hamburg, Germany

Figure S1 displays a TEM image of irregular, ~10-20 nm large nanostructures shortly after initiating the fast reduction. These structures are referred to as "nanoflakes" in the main body of the manuscript. Selected area electron diffraction reveals these nanoflakes to be crystalline $Sb_{(2-x)}Bi_xTe_3$.

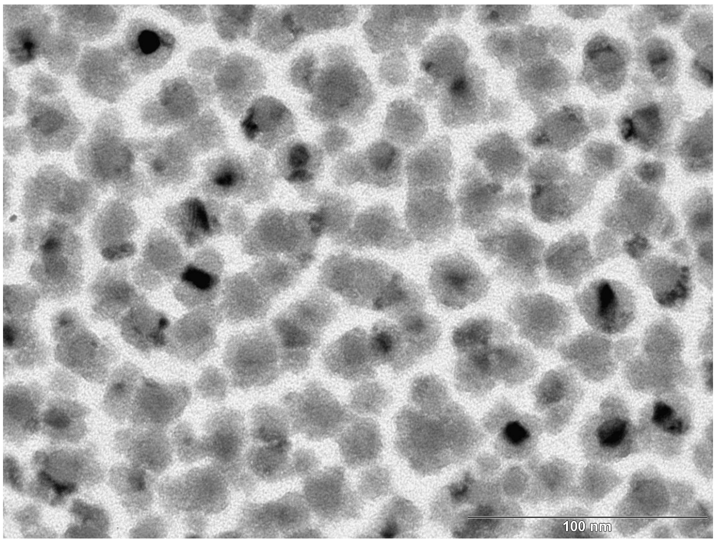

Figure D-S1: TEM image of Sb2-xBixTe3 nanoflakes.

In **Figure S2**, an XRPD pattern of $Sb_{1.0}Bi_{1.0}Te_3$ nanosheets is provided. In accordance with the picture of nanosheets as a thinner and bismuth.rich pre-stage of nanoplatelets, the reflections are shifted to slightly larger lattice spacings and the intensities of the (00X) reflections are reduced. The lattice constants for a hexagonal unit cell were determined to a = 4.272 Å and c = 30.50 Å.

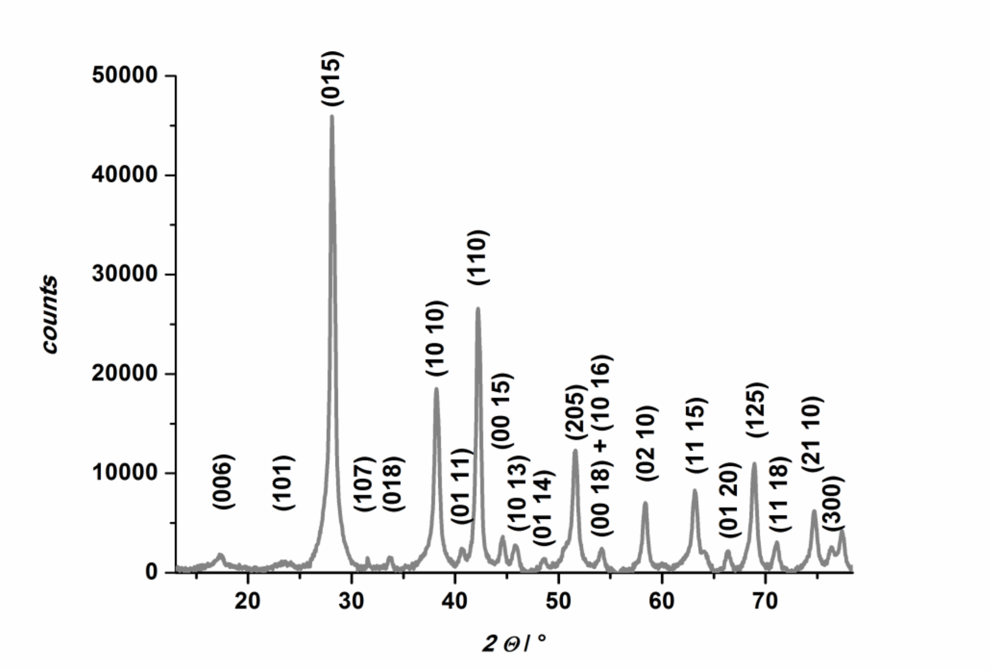

Figure D-S2: XRPD pattern of $Sb_{1.0}Bi_{1.0}Te_3$ nanosheets. Indexing according to space group R-3m (166). Note the reduced intensities of the (00X) reflections in comparison to the XRPD pattern of $Sb_{1.7}Bi_{0.4}Te_3$ nanoplatelets displayed in **Figure 2**.

Figure S3 depicts a typical energy dispersive X-ray spectrum (EDXS) of a single $Sb_{1.7}Bi_{0.4}Te_{3.0}$ nanoplatelet.

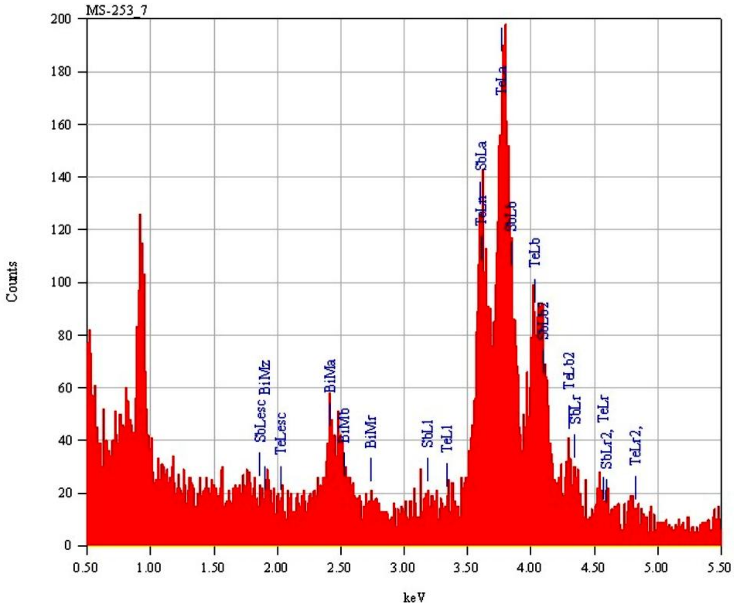

Figure D-S3: Typical EDXS of Sb$_{1.7}$Bi$_{0.4}$Te$_3$ nanoplatelets. Analyzed transitions were the M-transitions for bismuth and the L-transitions for antimony and tellurium. The peak at ~1 keV is an L-transition of copper caused by the copper-carbon-substrate necessary for TEM imaging.

Figure S4 presents a comparison of the X-ray powder diffraction (XRPD) behaviour between 1-dodecanethiol stabilized Sb$_{1.7}$Bi$_{0.4}$Te$_3$ nanoplatelets and the same platelets after removal of the stabilizing agent as described in the experimental part of the main body of the manuscript. It is noteworthy that the crystalline phase does not change significantly during this procedure. The change in relative intensities of selected reflections (for instances that of the (110) plane at 2θ = 42.3 °) can be interpreted as a preferential alignment of individual of 1-dodecanethiol stabilized nanoplatelets during drying on the substrate. In the case of ligand-free nanoplatelets such an alignment is not possible.

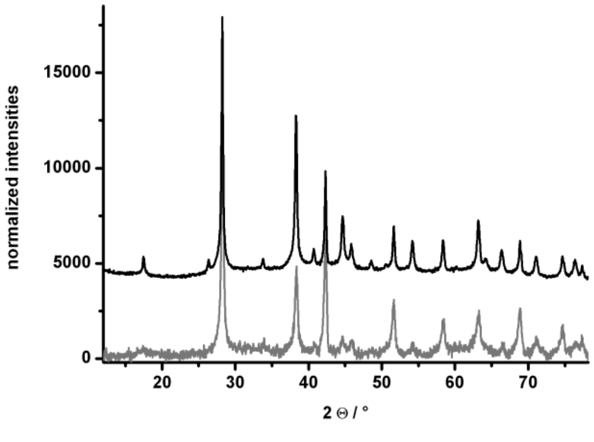

Figure D-S4: XRPD of Sb$_{1.7}$Bi$_{0.4}$Te$_3$ nanoplatelets before (**top**) and after (**bottom**) ligand removal with a methanolic solution of ammonia.

In **Figure S5** a temperature time profile of a typical spark plasma sintering experiment is displayed. It must be emphasized that the temperature in this figure is the overall temperature measured at the outside surface of the die. Determining the actual sample temperature inside the die is not possible due to the high pressure applied during the experiment. As with every spark plasma sintering experiment, the sample heating was achieved by applying a pulsed disalternating current on the sample of approximately 100 A. Noteworthy is the short sintering time and the low maximum temperature as compared to bulk samples. From our experience for comparable bulk samples, one requires considerably higher die temperatures (~ 300 °C) and longer sintering times (~1 h) to obtain similar relative densities (85 %) as that obtained with the conditions displayed in **Figure S5** for nanostructured samples. This implies a significant reduction in the melting point of the material due to the nanostructure and its high surface energy.

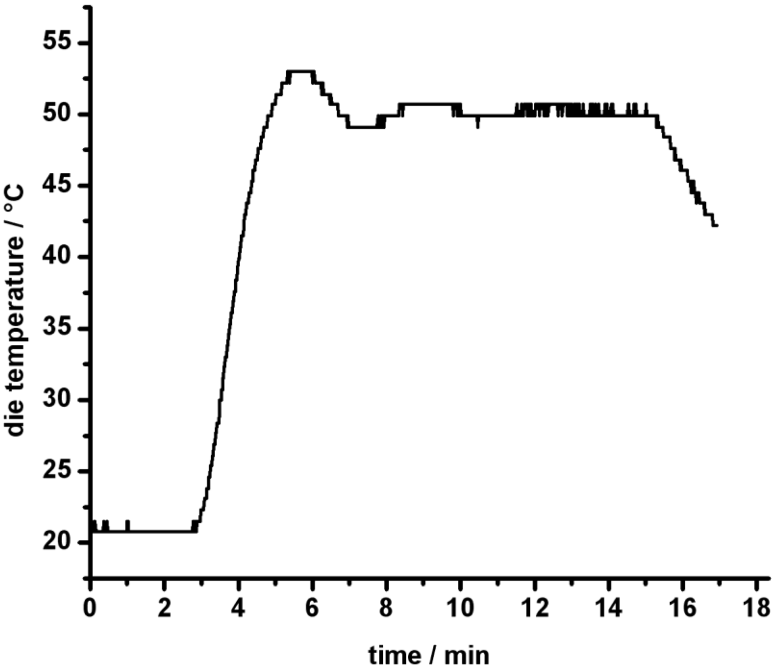

Figure D-S5: Temperature-time-profile of a typical spark plasma sintering experiment. Note that the y-axis displays the overall outside-temperature of the die. The actual temperature inside the sample is unknown and believed to be considerably higher.

In **Figure S6** a photograph of typical pellets of nanoplatelets is shown. They are mechanically robust and silver-metallic in appearance. The choice of geometry was for convenience in view of the thermoelectric characterization but is not limited to the sizes depicted in the figure. Although all samples were stored in the absence of air wherever possible, no apparent changes to the samples' surfaces were notable even after hours of exposure to ambient atmosphere.

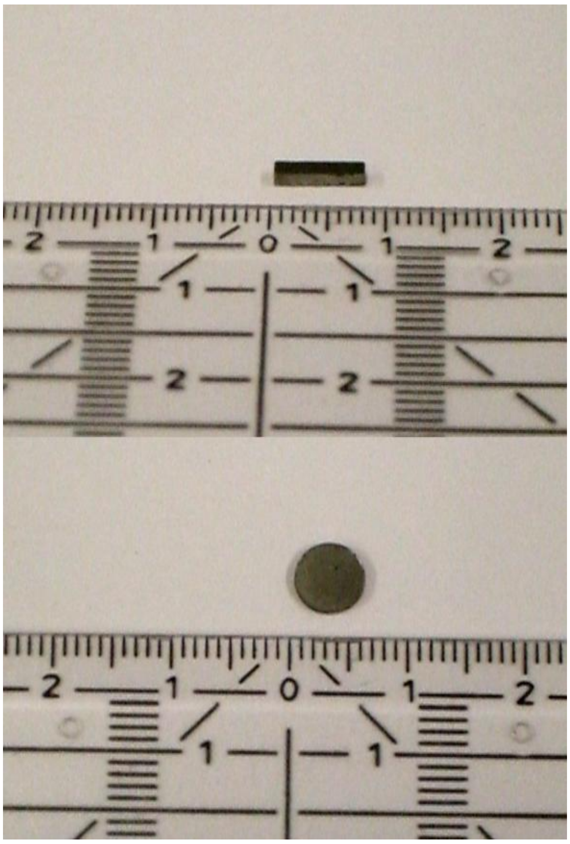

Figure D-S6: Photograph of typical pellets of $Sb_{1.7}Bi_{0.4}Te_3$ nanoplatelets used for thermoelectric characterization. (**Top**) 8.0 mm x 1.5 mm x ~1.5 mm bar for determination of resistivity and thermopower. (**Bottom**) 6.0 mm x ~1.2 mm disk for determination of the thermal diffusivity. The scale bar is in units centimeter.

To investigate the effect of spark plasma sintering under the mild conditions depicted in **Figure S5**, a typical pellet of $Sb_{1.7}Bi_{0.4}Te_3$ nanoplatelets was ground to a fine powder and investigated by XRPD as presented in **Figure S7**. Neither did the crystalline phase change nor the full width half maximum of several selected reflections indicating that no significant grain growths occurred during the sintering.

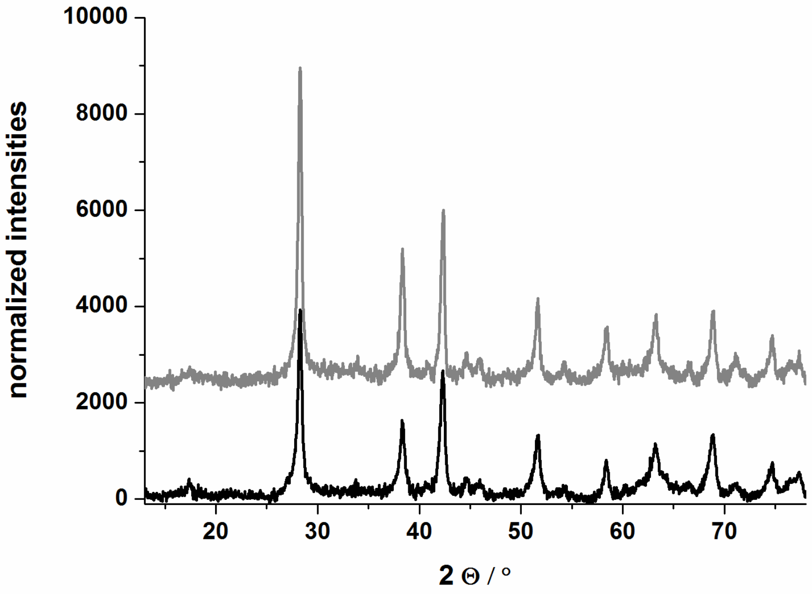

Figure D-S7: XRPD of a pellet of $Sb_{1.7}Bi_{0.4}Te_3$ nanoplatelets before (**top**) and after (**bottom**) spark plasma sintering.

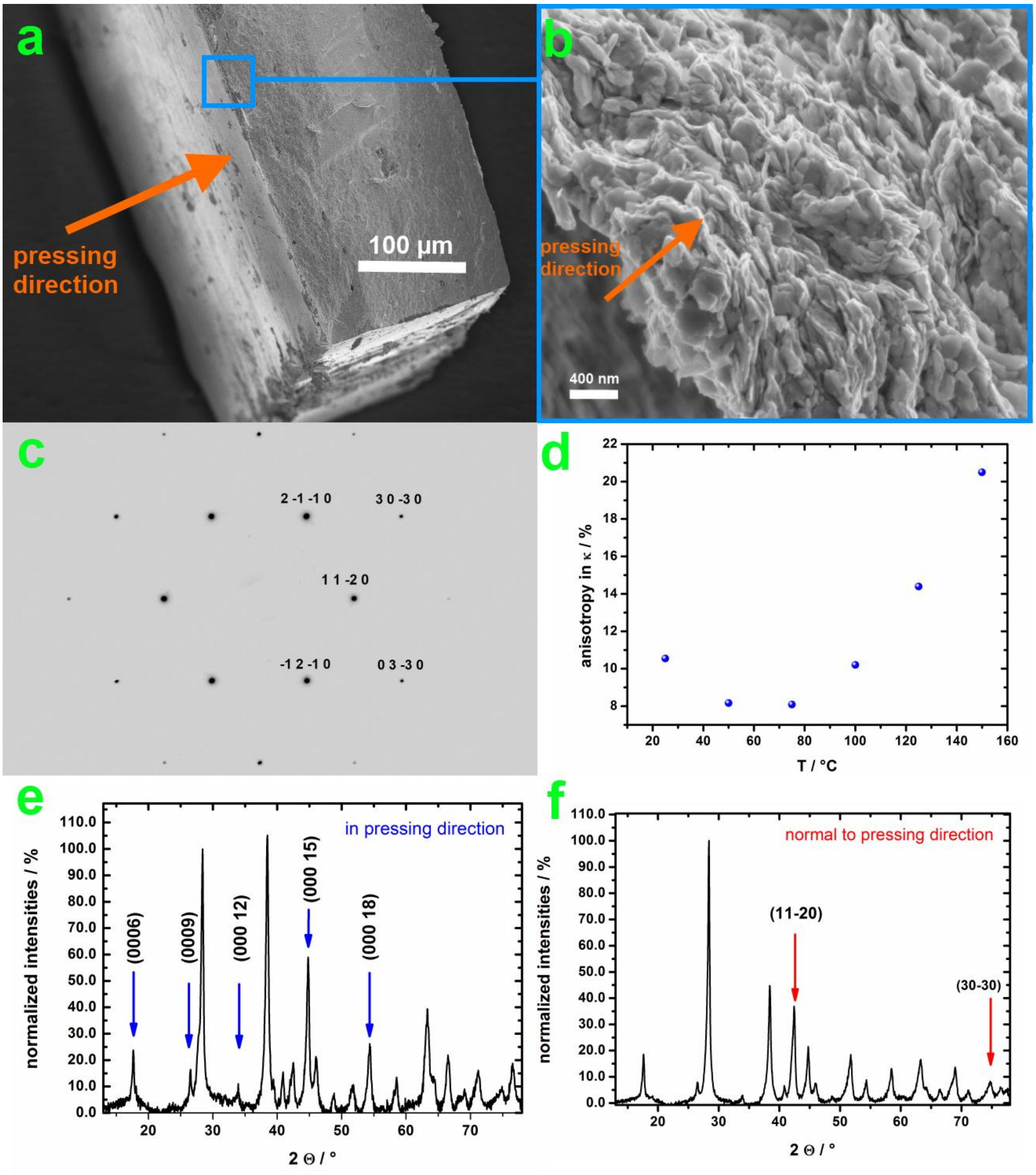

Figure D-S8: (**a**) Low magnification SEM image of a small piece cut from the rectangular sample displayed in **Figure S6**. The smooth side on the left is the bottom of the original sample. Pressure during SPS was applied normal to this plane. (**b**) High magnification SEM image of the edge of the same sample. The pressing direction during SPS is indicated by the orange arrow. (**c**) Electron diffraction of a single nanoplatelet viewed from above verifying that platelets have grown in the a-b-plane. (**d**) Difference in thermal conductivity of the sample displayed in **S5** when measured normal to the pressing direction and in the pressing direction. Measuring normal to the pressing direction results in higher thermal conductivity. (**e**) XRD of the sample in pressing direction and (**f**) normal to the pressing direction. The (01-15) reflection at 28.3 ° is normalized to 100 % intensity for both XRDs. Reflections of the c-planes ((000x) and the a-b-planes ((11-20) and (30-30)) are indicated.

In **Figure S8**, we investigate anisotropy in microstructure and transport of the pellets of nanoplatelets. Structural characterization ((**a**) and (**b**)) reveals that individual platelets are poorly ordered after spark plasma sintering with a slight tendency to align with the flat surface (the a-b-plane) normal to the pressing direction. This tendency is further studied by diffraction methods. For clarification, an electron diffraction pattern of a single nanoplatelet viewed from above is given ((**c**)). Since each nanoplatelet growths in the a-b-plane, a sample with perfectly orientated individual nanoplatelets would exclusively show the (11-20) and (30-30) reflection when inspected normal to the pressing direction by X-ray diffraction. Likewise, X-ray diffraction in the pressing direction of a perfectly orientated sample would solely show the (0003) reflection and higher orders thereof which is the c-direction. In contrast to this, the material in this work displays almost every reflection to be expected for SbBiTe3 regardless of the measurement direction which underlines the low degree of nanocrystal orientation. Again, there is a slight tendency for the c-planes to be orientated in the pressing direction ((**e**)) and the a-b-planes to be orientated normal to the pressing direction ((**f**)) as one compares the intensities of the reflections of interest. This underlines the picture of a sample with a significant but low degree of preferential orientation of individual nanoplatelets.

Since thermal transport in the a-b-direction of single-crystal Bi_2Te_3 is 2 to 2.5 times higher than in the c-direction, the degree of preferential orientation can be deduced form direction-dependent thermal conductivity measurements. To do so, we fabricated a flat disc from four rectangular bars of pellets of nanoplatelets. Firstly, the four bars were attached side-by-side with standard graphite spray in such a way that the resulting disk extended normal to the pressing direction of the four individual bars. The thermal conductivity was measured by Laser flash analysis as described in the experimental part. Secondly, the four bars were detached, each bar turned by 90 °C and fixed again with graphite spray to a flat disk. This time, the resulting disk extended in the pressing direction of the four individual bars and the thermal conductivity was measured. In **Figure S8** (**d**), the difference of the two measurements is shown. In accordance with the picture of a sample with a slightly preferential orientation of individual nanocrystals, the sample's thermal conductivity is between 8 – 18 % larger normal to the pressing direction than in the pressing direction. However, this should be compared to the difference of 100 % and more to be expected for a perfectly orientated sample.

Since the absolute measurement values of samples fabricated by attaching several bars are likely to possess a larger uncertainty than measurements of single pieces, we prefer to carry out measurements with the single-piece disks displayed in **Figure S6** (**bottom**). However, with these samples one can only measure thermal transport in the pressing direction. To allow a combination with electric transport measurements (measured normal to the pressing direction), the thermal conductivity data reported in this work was corrected for the temperature dependent effect of anisotropy as shown in **Figure S8** (**d**) to larger values.

Chapter E

Thermopower enhancement by energy filtering in lead chalcogenide core-shell nanostructures

Thermopower enhancement by energy filtering in lead chalcogenide core-shell nanostructures

Introduction

Lead chalcogenides have been extensively investigated for thermoelectric applications.[81] With a maximum of 0.7 (at 773 K) in the thermoelectric figure of merit (ZT), PbTe is one of the best thermoelectric materials at intermediate temperatures (at 450-800 K).[82] To increase ZT towards economical competitiveness with conventional electric power generators, nanostructuring is nowadays widely applied.[83] A key concept of this approach is the electron-crystal phonon-glass (ECPG) effect, which arises from the preferential scattering of phonons over charge carriers leading to a larger decrease in thermal conductivity (κ) than in electric conductivity (σ).[31] Since ZT is proportional to σ/κ, the ECPG effect leads to an enhancement in ZT.[84] Nanoparticle inclusions of a second material (e.g. Sb_2Te_3, $AgSbTe_2$ or Sb) into PbTe are known to lead to drastic reductions in κ.[85, 86, 87] Specifically, inclusions of PbS have been shown to maintain high electron mobilities due to the presence of coherent interfaces but decrease phononic contributions to κ to 0.5 $Wm^{-1}K^{-1}$ for temperatures of 300-700 K.[88, 89]This is believed to be the lower limit for PbTe-based materials.[90] Therefore, complimentary approaches to the ECPG-concept need to be addressed to achieve further enhancements in ZT.

A suitable concept is the Mahan-Sofo theory predicting large improvements in ZT for materials where the Fermi level is tuned into a region with a high density of states (DOS).[21] For PbTe this has been achieved by controlled doping with thallium which leads to a 2-fold increase in ZT.[91] Regions with large DOS can conveniently be created in semiconductor nanoparticles with sizes smaller than the exciton-bohr radius by utilizing the quantum confinement effect. Theoretically, δ-functions of DOS are possible for 0D-structures bearing the potential for extreme improvements in ZT.[12] The applicability of this concept has been demonstrated with ligand protected PbSe nanoparticles of less than 10 nm in diameter leading to an unusually high thermopower of > 1 mV K^{-1}.[27] Due to its large exciton-bohr radius of 152 nm, PbTe is an ideal material to employ quantum confinement effects for improvements of ZT.[92, 93] Shape-controlled PbTe nanoparticles of suitable sizes have been prepared by several groups.[94, 95, 96, 97, 98] The low electric conductivities resulting from insulating surfactants necessary in these synthetic protocols can now be circumvented by various procedures.[99,50,100] To confine carriers inside a nanoparticle and manipulate the DOS, growing a shell of a second material onto the core of the primary material is a suitable technique.[101,102] Lead chalcogenide core-shell nanoparticles have been prepared by other groups but were mainly investigated in terms of their optical properties.[103,104,105]

Another promising attempt is energy filtering by intentionally introducing potential barriers to charge carrier transport. Since most materials applied for thermoelectrics are degenerate semiconductors, the Fermi level (E_F) in these compounds is located close to or even inside a band. This leads to the disadvantageous situation that carriers from both sides of the Fermi level contribute to the total thermopower. Since thermopower is a measure for the average energy per charge c arrier *with respect to* E_F, the individual thermopower of carriers from one side of E_F partially cancel that of carriers from the other side of E_F. Thus, the total thermopower of a degenerate semiconductor would be larger if carriers from one side of E_F are immobilized. When a low potential barrier ($\Delta E \leq 100$ meV) is introduced above E_F, only carriers of higher energy can contribute to electric transport and the average energy per charge carrier is increased. This concept has been modeled for metal-based superlattices and nanocomposites. [28,29] Experimental proof of principle has been provided by samples of nanostructured bulk PbTe. The large surface area in such nanograined materials provides a high trap state density in each grain caused by surface adsorbates. When charge carriers are trapped on the surface, they provide an energy barrier to electric transport which leads to energy filtering.[22] However, it is unclear if the observed increase in thermopower in nanograined materials is due to energy filtering or to an increase in the scattering parameter caused by the large density of incoherent crystalline domains.[20]

Here, the effect of epitaxially growing a shell of a second material onto PbTe nanoparticles and fabricate macroscopic nanostructured samples of this material is studied. It is shown that core-shell nanoparticles are ideal candidates to apply the energy filtering concept and increase a materials thermopower. By alloying of the core and shell material, the formerly heterophased grains are transformed into a single phase of similar grain size which allows to determine whether the increased thermopower is a result of energy filtering or of enhanced carrier scattering.

Results and discussion

PbTe nanoparticles were synthesized in dephenylether solution on applying oleic acid as the stabilizing ligand. A typical synthesis yields several 100 mg per batch of monodisperse octahedral nanoparticles (**Figure 1a-f**). A histogram of the edge lengths for the particles displayed in **Figure 1b** is given in **Fig. 1e**, revealing an average of 20 nm. On assuming regular octahedra, this corresponds to an insphere diameter of 16 nm.

In **Figure 1f**, the electron diffraction pattern of the single PbTe crystal displayed in **Fig. 1c** is depicted revealing the direction of view as <111>. Since PbTe crystallizes in the fcc lattice, it follows that each facet of the octahedron is a {111}-facet. Within the rocksalt structure, structural discrimination from cubic to octahedral can be achieved by thermodynamic *versus* kinetic control, respectively. Slow growth kinetics of the {111}-facets are typically achieved for a large excess of Pb-precursor in combination with the presence of primary amines or thiols.[36,106] As a reason for this unusual stability of {111}-facets, a μ-Pb$_3$-SR-bonding at least in the case of thiol-stabilization was proposed. {111}-Facets in PbTe are composed exclusively of either Pb or Te atoms which distinguishes them from {100}-facets in which both atoms are equally abundant. Only in the former case, multiple binding modes with high binding energies are possible. When working with a large excess of Pb-precursor, the {111}-facets are likely to be terminated by Pb-atoms in which case the growth in this direction can be inhibited.

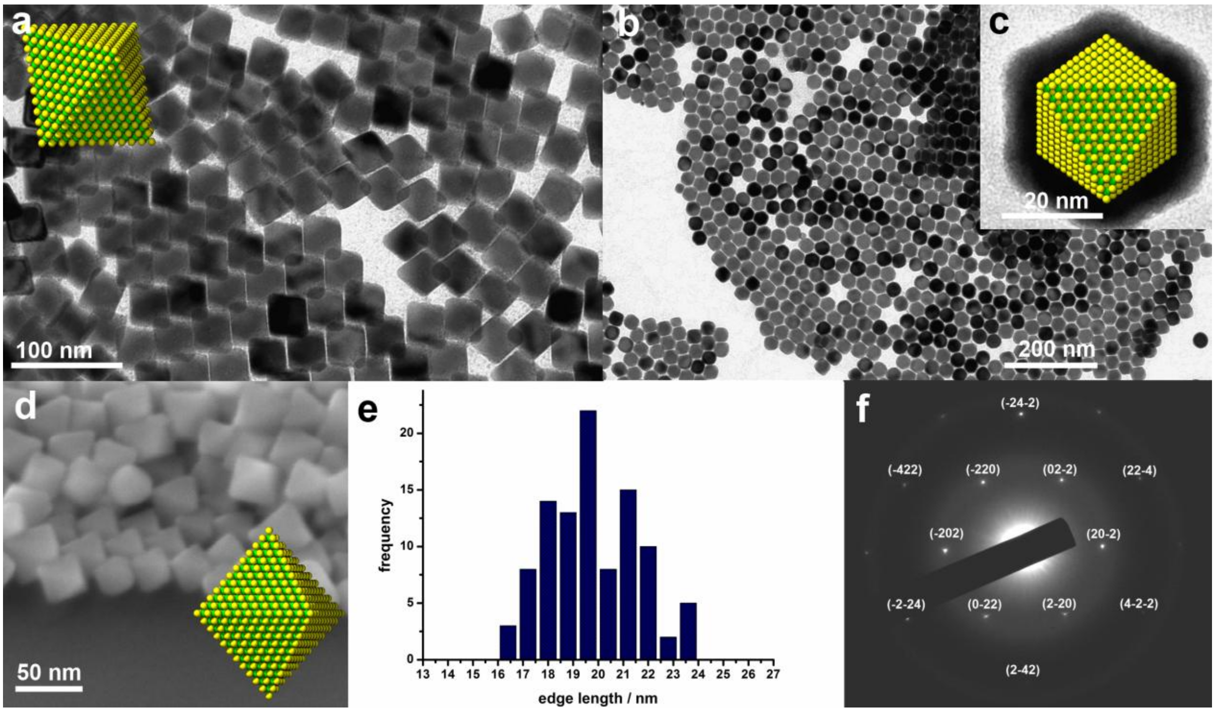

Figure E-1: (a-c) TEM images of octahedral PbTe nanoparticles in <110>- (**a**) and <111>-projection (**b** and **c**). (**d**) SEM image of PbTe nanoparticles. (**e**) Histogram of the PbTe nanoparticles' edge lengths. (**f**) SAED of the single PbTe nanoparticle in (**c**). Indexing according to the rock salt structure.

Another important aspect about structural discrimination in lead chalcogenide nanocrystals has been investigated by Houtepen et al.: the presence of catalytic amounts of acetic acid.[35] Their observations can be fully confirmed in so far as the presence of a small amount of acetic acid is essential in order to obtain the octahedra depicted in **Fig. 1a-d**. If acetic acid is absent, only cubic nanoparticals can be synthesized under otherwise identical conditions (see **Figure S1** in the appendix).

The mechanism involved is a dipole driven oriented attachment supported by acid induced ligand destabilization. Briefly, it can be shown that spherical lead chalcogenide nanoparticles (constructed by six {100}-facets and eight {111}-facets) possess an unusually high reactivity in the <100> direction due to a dipole generated by an asymmetric distribution of the four lead and chalcogenide {111}-facets.[36] This dipole can be strong enough to lead to a large variety of anisotropic structures like wires, rings, stars, and octahedra by oriented attachment along the axis of the dipole. If cubic nanoparticles are present, each of the cube's six {111}-facets provides a suitable place for oriented attachment of the smaller nanoparticles carrying a dipole.[107] If the stabilizing ligand is oleic acid/oleate, the probability of oriented attachment to the cubes is greatly increased if catalytic amounts of acetic acids are present.[21] By protonation of the oleate ligands, facets are temporarily destabilized which supports an attachment. This attachment necessarily leads to the formation of {111}-facets on the former cube which generates a second dipole for the same reason as discussed above but this time alongside the <111>-axis of the former nanocube. This way, the oriented attachment is self-accelerating and terminates in a crystal without any {111}-facets which is the regular octahedron.

To allow for high electric conductivities, all organic residues have to be removed from the inorganic nanoparticles. Oleic acid stabilized PbTe nanoparticles in hexane were treated with an excess of phosphonic acid in solution to induce ligand exchange. Phosphonic acid ligands were removed by adding a methanolic ammonia solution which separated the polar nanomaterial from the non-polar organic residues following a previously developed protocol.[100] After drying the inorganic material under vacuum, a dark-grey nanopowder was obtained.

To fabricate a nanostructured bulk material, this powder was spark plasma sintered (SPS) to a macroscopic pellet. Pellets of PbTe nanoparticles were silver-metallic in appearance with a density of 7.30 ± 0.10 g cm^{-3} (89 % of theoretical density) under the conditions specified in the experimental section and the appendix (**Figure S2**). To achieve larger densities towards 100 % of the theoretical value, significantly higher sintering temperatures and duration are required which resulted in unwanted grain growth during compaction.

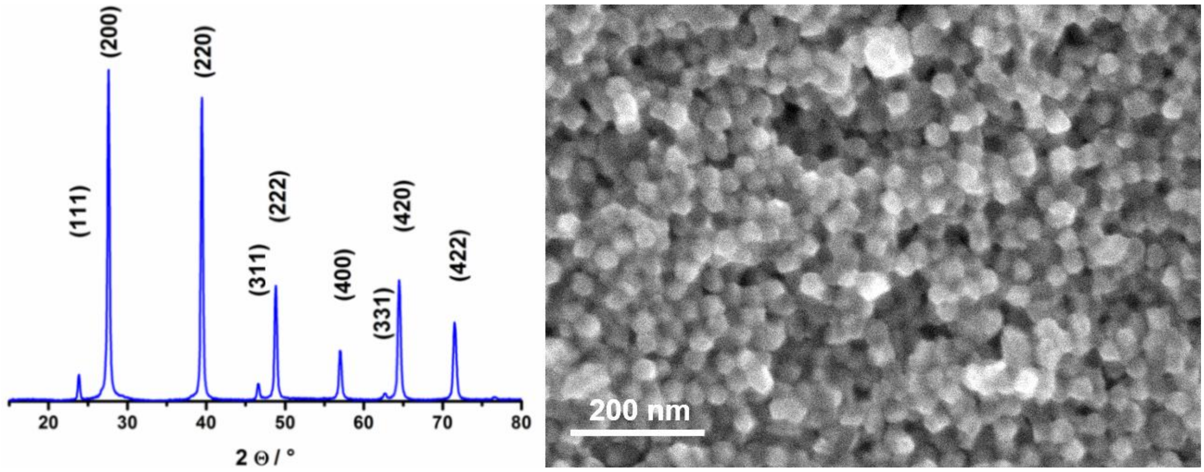

Figure E-2: (left) XRPD of spark plasma sintered pellet of PbTe nanoparticles. Indexing according to the rock salt structure. (**Right**) SEM image of the compacted pellet of PbTe nanoparticles.

It should be noted that several other groups have compacted lead telluride nanocrystals before by either SPS or hot-pressing. In all cases, the applied temperatures were significantly higher (310 – 500 °C) than our applied temperature range (100 – 200 °C).[84,87,74,108] The results in **Figure 2** suggest that nanostructured PbTe bulk samples with grain sizes < 30 nm can only be obtained if the temperature during SPS is kept to ~100 °C. At 195 °C and even at 154 °C significant grain growth was observed. (Note that during SPS the actual sample temperature inside the die is not known but anticipated to be somewhat higher.)

The low melting point of nanostructured PbTe pellets with grain sizes of ~30 nm is a consequence of the high surface to volume ratio in this material. Surface atoms possess higher degrees of freedom and greater energy as opposed to their bulk equivalents due to unsaturated binding sites. This is known to cause a large depression in melting temperature for sufficiently small crystal grains.[109] Note that bulk PbTe melts at 924 °C.

Another effect of the high surface to volume ratio in nanostructured materials is an alteration of the molar specific heat (C_P) as visible in **Figure 3**. There are a number of experimental verifications that nanograined materials generally possess a specific heat which exceeds Dulong-Petit's rule by up to 40 % at 300 K.[110,111,112,113] Other groups found reduced Debye temperatures (T_D) in nanostructured materials.[114,115] In the nanostructured PbTe sample in this work, both effects are present. At 300 K, the rule of Dulong and Petit with C_P approaching 3 N R is violated by an excess of almost 20 % (**Figure 3a**).

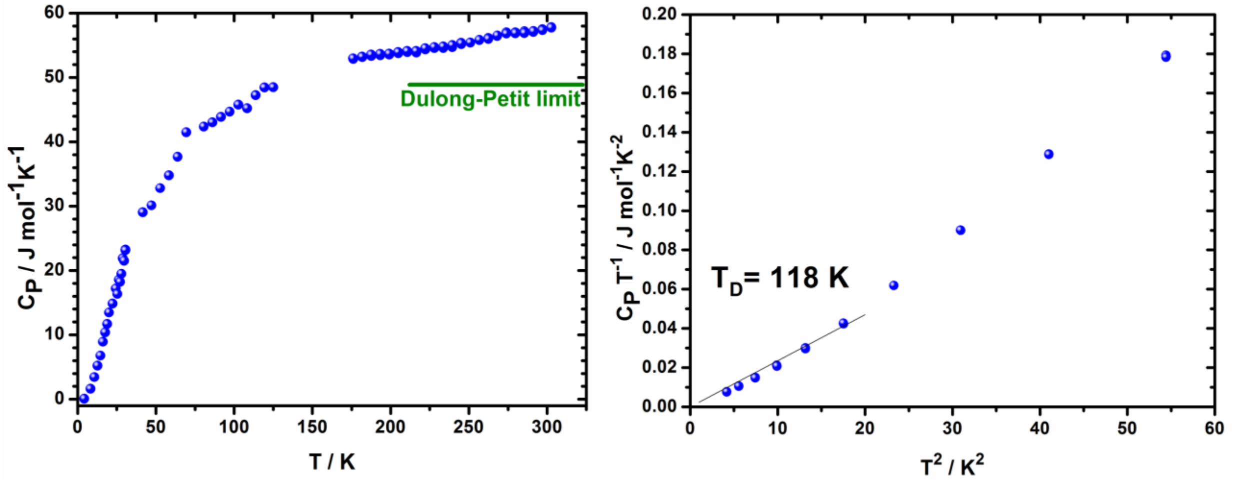

Figure E-3: (left) Specific heat capacity of spark plasma sintered PbTe nanoparticles. (**Right**) Plot of C_P/T *vs.* T^2 to derive the Debye temperature of a pellet of spark plasma sintered PbTe nanoparticles.

From the plot in **Figure 3b**, T_D can be evaluated applying

$$C_P = \frac{12\pi^4}{5} NR \left(\frac{T}{T_D} \right)^3$$

with N = 2 being the number of atoms per molecule and R = 8.314 J mol^{-1}K^{-1} being the gas constant. The resulting T_D = 118 K is significantly smaller than the value reported for large PbTe single crystals (T_D = 168 K).[116] These findings qualitatively support a recent theoretic description of the dependence of C_P and T_D on the grain size in nanostructured materials.[17]

In **Figure 4**, the elemental composition of individual PbTe nanoparticles after ligand removal is investigated by high angle attenuated dark field (HAADF) and energy dispersive X-ray spectroscopy (EDS). Even close to the surface, particles appear to be single-crystalline (**Fig. 4a**). In contrast to previous works no significant amorphous shell could be detected which easily forms if PbTe is treated with aqueous bases or exposed to oxygen.[105] However, elemental mapping (**Fig. 4b**) and spatially resolved EDX scans across individual particles (**Fig. 4c**) show significant amounts of oxygen especially close to the particle's surfaces. Oxidation of PbTe surfaces is a complex, multi-staged process which is believed to start with the formation of peroxide-like structures and terminates in the formation of $PbTeO_3$ on exposure to large O_2 concentrations.[117, 118] The absence of features originating from such materials in XRPD (**Fig. 2 left**) and high resolution transmission electron microscopy (HRTEM, **Fig. 4a**) confirm earlier observations that oxidation by O_2 affects almost exclusively the uppermost monolayer of PbTe.

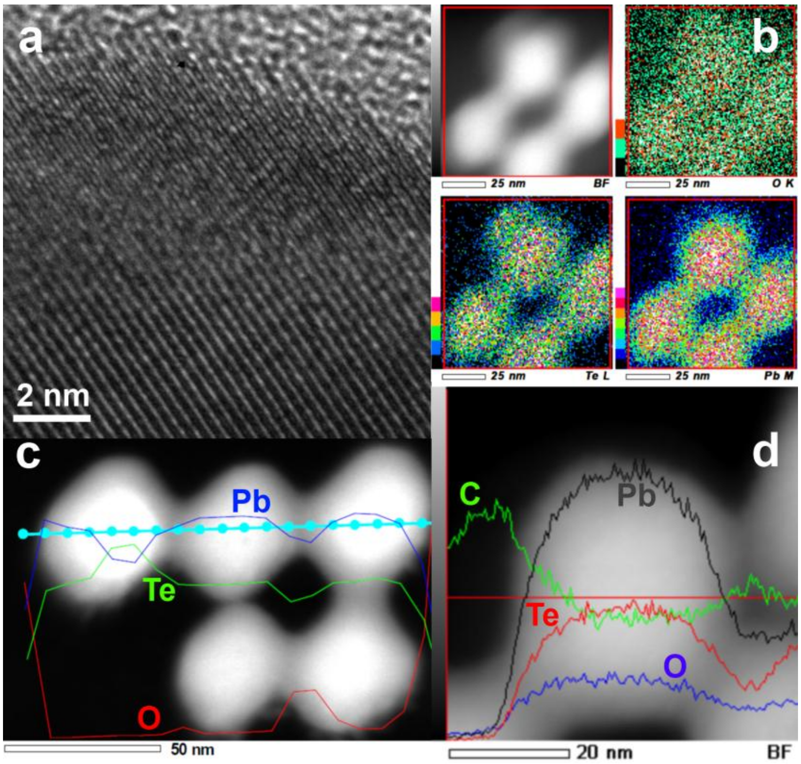

Figure E-4: (a) HR-TEM image of the edge of a single PbTe nanoparticle. The region of lower contrast shows the amorphous carbon substrate. (**b**) EDS based elemental mapping of four PbTe nanoparticles: (**top left**) Bright field STEM image, (**top right**) oxygen K-line, (**bottom left**) tellurium L-line and (**bottom right**) lead M-line. Scale bars are 25 nm. (**c**) EDS line scan across three PbTe nanoparticles with 5 nm resolution. The spatial variation of the quantified EDS signals of Pb, O and Te are depicted over the corresponding STEM image in the background. The scale bare corresponds to 50 nm. (**d**) Continuous, non-quantified EDS line scan over a single PbTe nanoparticle and spatial variation of the Pb, Te, C and O signal plotted over the STEM image in the background. The scale bar corresponds to 20 nm.

The continuous non-quantified EDS scan in **Figure 4d** reveals the carbon signal originating from the free (carbon covered) TEM substrate to be larger than that from an area additionally covered with a PbTe nanoparticle. This underlines the effectiveness of the ligand removal process leaving no substantial amounts of carbon containing residues on the particles’ surface.

The thermoelectric properties of sintered pellets of PbTe nanoparticles as imaged by scanning electron microscopy (SEM, **Fig. 2 right**) are displayed in **Figure 5**. In accordance with the picture of surface oxidized PbTe nanoparticles, electric transport (**Fig. 5a**) shows strong temperature activated behavior and a resistivity (ρ) which is more than one order of magnitude larger than in a comparable bulk material.[89] Nolas and coworkers found a similar behavior for nanostructured PbTe samples with grain sizes of ~350 nm and explained it with grain boundary potential barrier scattering due to chemisorbed oxygen at the PbTe grain boundaries.[72,73] They calculated and experimentally demonstrated that surface oxygen can trap charge carriers and provide an energy filter which allows only carriers of sufficient energy to pass and contribute to electric conduction as well as thermopower (S). Since this increases the mean energy per carrier, they found significantly larger S values. Such energy filtering is especially effective in heavily doped semiconductors where the Fermi level (E_F) is often found almost inside a band. At temperatures sufficiently above absolute zero, a substantial amount of carriers with energies greater and smaller than E_F counteract each other leading to a partial cancellation in S. Trapping low-energy carriers at grain boundaries prevents such cancellations and increases the total thermopower.[19] The unusually large thermopower of nanostructured surface oxidized PbTe with grain sizes of ~ 30 nm presented in **Figure 5b** demonstrates this effect. With 600 μV K^{-1} at room temperature, this significantly exceeds the bulk value of 265 μV K^{-1} and that of the Nolas group with 325 μV K^{-1}. This may be explained with the much smaller grain sizes and thus the larger number of trap states in the sintered sample. Following an experimentally derived dependence between S and the carrier concentration for PbTe reported in literature, 600 μV K^{-1} corresponds to a hole concentration (p) of roughly 2.0 x 10^{-17} cm^{-3} which should be compared to p = 2.2 x 10^{-18} cm^{-3} for typical bulk samples.[119,72]

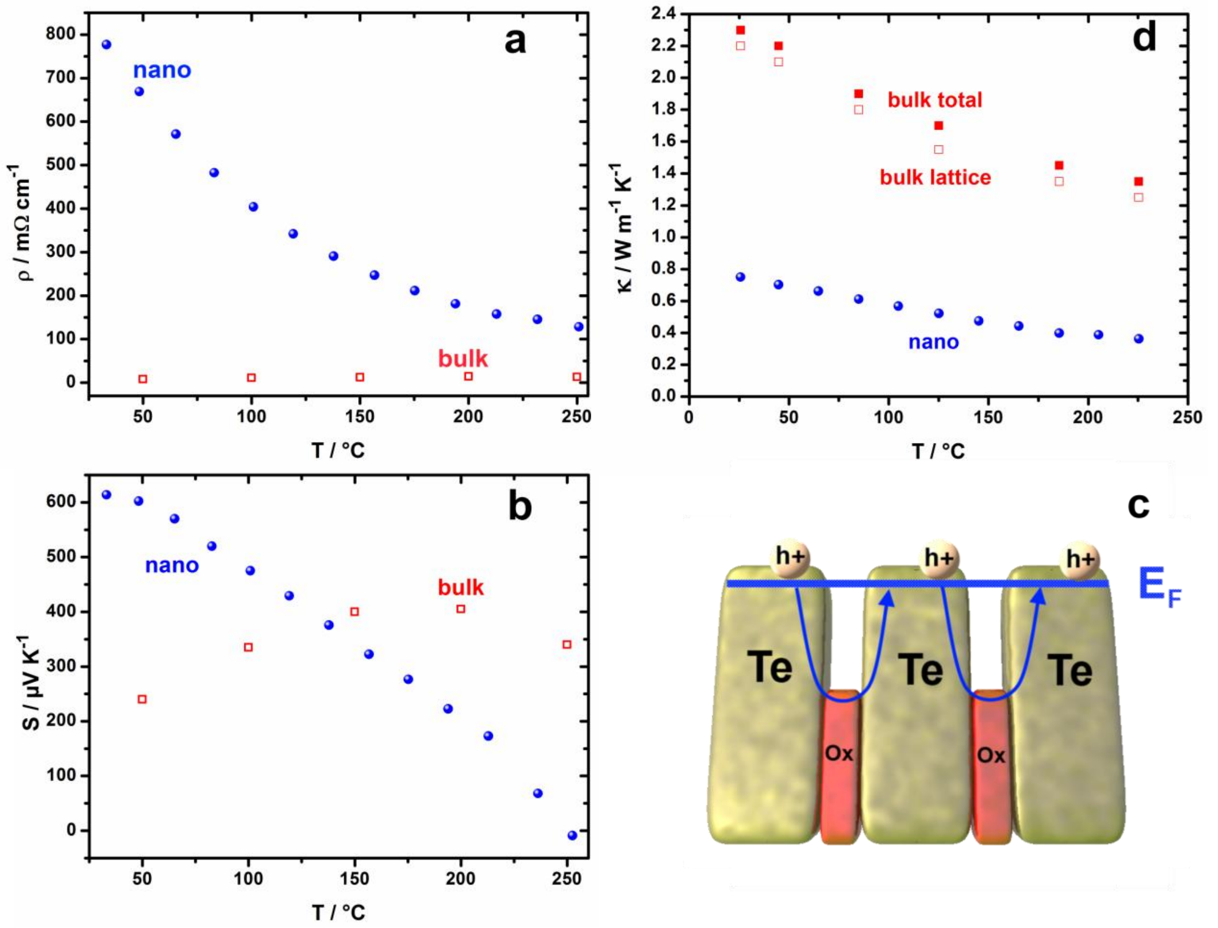

Figure E-5: (a) Resistivity, (**b**) thermopower and (**d**) thermal conductivity of spark plasma sintered, surface-oxidized PbTe nanoparticles (**circles**) in comparison to bulk values reported in literature (**squares**). The bulk thermal conductivity in (**d**) is plotted in terms of its lattice contribution (**open squares**) and total value (**closed squares**). The lattice contribution of the nanostructured sample is identical with the total thermal conductivity. (**c**) Simplified band structure around the valence band edge for the pellet of surface-oxidized PbTe nanoparticles.

The simplified band structure leading to this drastic reduction in hole density is depicted in **Figure 5c**. Approximatively, the conduction band has mainly lead character, whereas the valence band has tellurium character. E_F is supposed to lie very close to the valence band edge if not inside. Thus, only the electronic structure around the valence band edge is of importance for electric transport. Hole transport from grain to grain is greatly impeded by the frequent occurrence of narrow sinks in the valence band edges due to surface oxidation of each grain. This reduces the amount of mobile holes capable of traveling through the entire nanostructured sample. Meanwhile the average energy per hole increases as only holes of sufficient energy can pass the barriers. As a consequence ρ and S show the increase discussed above. For a more detailed discussion of the electronic structure, see also **Figure S5** and the accompanying text in the appendix.

Figure 5d verifies the well known advantages of nanostructured materials in terms of minimizing thermal conductivity (κ). Due to poor electric transport properties, the depicted total thermal conductivity of the nanostructured material is practically identical to the lattice contribution. It should be noted that both, resistivity (**Fig. 5a**) and thermal conductivity, have been corrected for effects of porosity according to the Maxwell-Eucken approach (parameters: porosity (P) = 11 % and $\beta = 2$) as described elsewhere.[120] In comparison with bulk PbTe, the lattice contribution to the thermal conductivity is reduced by approximately 70 % over the whole temperature range between 25 and 225 °C. The lowest reported lattice thermal conductivity of PbTe was found in a highly insulating nanostructured pellet with grains of 9-12 nm with 0.5 $Wm^{-1}K^{-1}$ at 300 K (not corrected for porosity).[90] This is only slightly smaller than the value reported in this work (0.75 $Wm^{-1}K^{-1}$) demonstrating that below a certain grain size only small additional reductions in κ can be achieved. According to other reports this critical grain size is to be found between 100-300 nm above which κ quickly increases towards the bulk value of 2.2 $Wm^{-1}K^{-1}$.[84, 108]

Following the idea of energy filtering by small potential barriers a second material has been synthesized: PbTe-PbSe core-shell nanostars as presented in **Figure 6**. PbSe has the same crystal structure as PbTe and almost the same band gap. Since a useful barrier height for effective energy filtering in combination with large electric conductivity is believed to be 40-100 meV, combining two materials of very similar band gaps to an alternating heterostructure can be highly advantageous for thermoelectric applications due to an expected increase in the power factor.[121]

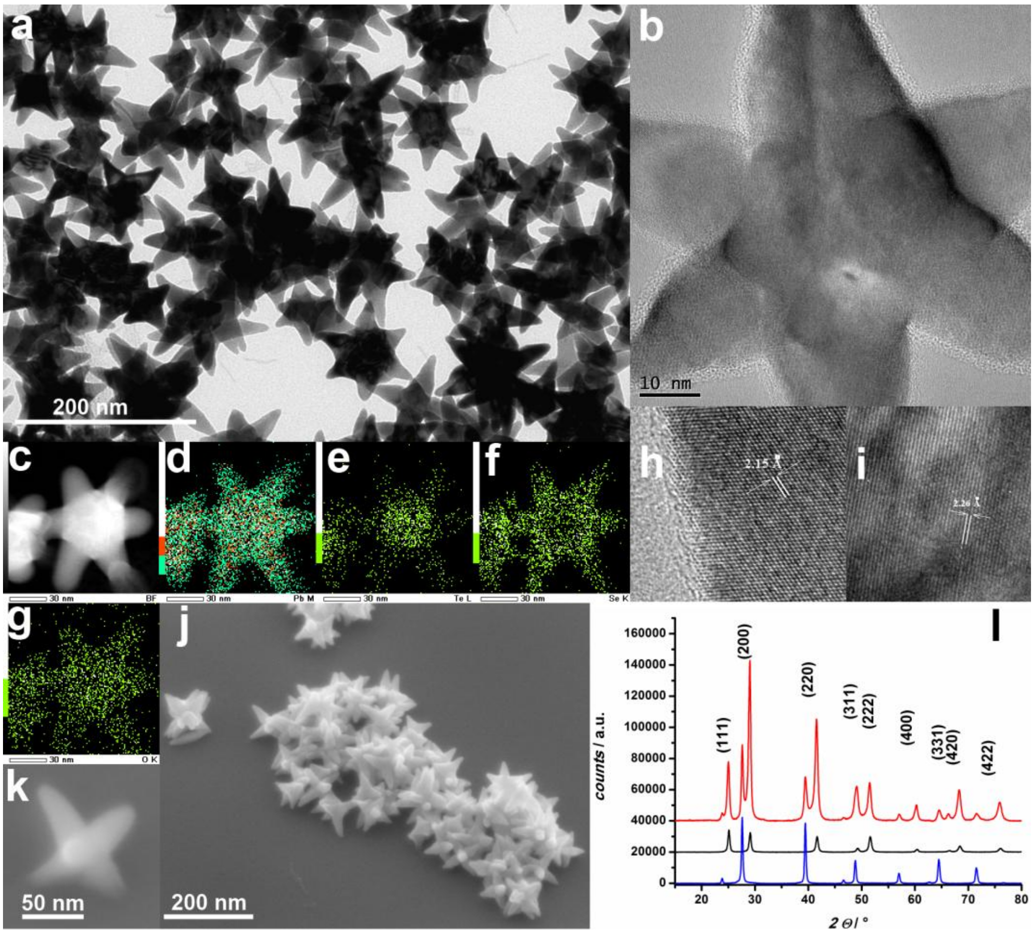

Figure E-6: (a-b) TEM images of surface-oxidized PbTe-PbSe nanostars. (**c-g**) EDS based elemental mapping of an individual nanostar. In order of appearance: Bright field STEM image, lead M-line, tellurium L-line, selenium K-line and oxygen O-line. Scale bars correspond to 30 nm. (**h-i**) HR-TEM images of the edge and centre of a nanostar. (**j-k**) SEM images of the nanostars. (**l**) XRPD of surface-oxidized PbTe-PbSe nanostars (**top**), PbSe nanoparticles (**middle**) and PbTe nanoparticles (**bottom**). Indexing according to the rock salt structure.

TEM images (**Figs. 6a,b**) reveal that on each PbTe octahedron six PbSe arms have been grown to result in a star-like structure. This can be understood in terms of epitaxial growth of PbSe in the <100>-direction onto each of the octahedron’s six tips. The key to this anisotropic growth is passivation of the {111} facets by stabilization with amines. **Figures 6c-g** display elemental mapping of an individual nanostar by EDS with respect to lead, tellurium, selenium, and oxygen. Tellurium is almost exclusively found in the core (**Fig. 6e**) whereas selenium is enriched in the arms. Note that due to the three-dimensional structure, there will always be one arm located behind the core of the nanostar which misleadingly adds to the selenium signal recorded in the core area. **Figure 6g** reveals a substantial degree of oxidation over the whole structure which is likely to be comparable with the results for pure PbTe nanoparticles (**Fig. 4**).

HRTEM images of a nanostar’s arm (**Fig. 6h**) and its core (**Fig. 6i**) display single-crystallinity and a difference in lattice spacing (d) in these two domains. The predominant spacing in the core (d = 2.26 ± 0.03 Å) is substantially larger than the spacing found in the arms (d = 2.15 ± 0.03 Å). This should be compared to the lattice spacing of the (220)-planes in PbTe (2.28 Å) and PbSe (2.16 Å) reported in literature.[122] No area with a significant number of stacking faults characteristic for an abrupt change from pure PbTe to pure PbSe crystalline material could be located. An intermediate section where a $PbTe_{1-x}Se_x$ alloy is present is assumed. For a SAED pattern of a single nanostar revealing the heterophased nature of the crystal see **Figure S3** in the appendix.

SEM imaging (**Figs. 6j, k**) shows the three-dimensional six-armed nanostar structure. Each star measures roughly 75 nm from tip to tip.

An XRPD comparison is presented in **Figure 6l**. At the bottom, the XRPD of pure PbTe is reproduced from **Fig. 2**. In the middle, the XRPD pattern of a product is shown which was obtained if PbSe nucleation was carried out in the absence of PbTe nanooctahedra. (See also **Figure S3** for more details about the pure PbSe phase.) This pattern matches with cubic PbSe ($Fm\bar{3}m(225)$). On top, the XRPD pattern of PbTe-PbSe nanostars is presented. Each index refers to a pair of reflections as both crystalline phases are of the same space group and possess the same number of reflections at similar angular positions. Since selenium is smaller than tellurium, the first reflection of a pair always represents PbTe where the second one stands for PbSe. For the higher indexed planes, some reflections of the two phases overlap and appear unresolved. From this XRPD pattern it can be concluded that each nanostar is mostly heterophased and only a small section consists of an alloy which is not abundant enough to appear as a distinct reflection in XRPD measurements. If any, the PbTe reflections in the heterophased nanostars appear to be shifted to higher angles as compared to the pure core material. This can be interpreted in terms of a $PbTe_{1-x}Se_x$ alloy formation in the core whereas the shell consists of practically pure PbSe which is consistent with **Figs. 6e and f**. However, x must be small since the angular shift is not prominent.

PbTe-PbSe nanostars were treated according to the procedure described for PbTe nanooctahedra to remove organic ligands and prepare a nanopowder for SPS. The density after SPS compaction was 6.40 ± 0.10 g cm^{-3} (78 % of theoretical density). This relatively low value accounts for the bulky star like structure which was preserved after SPS. Nonetheless, samples were mechanically stable and silver metallic in appearance.

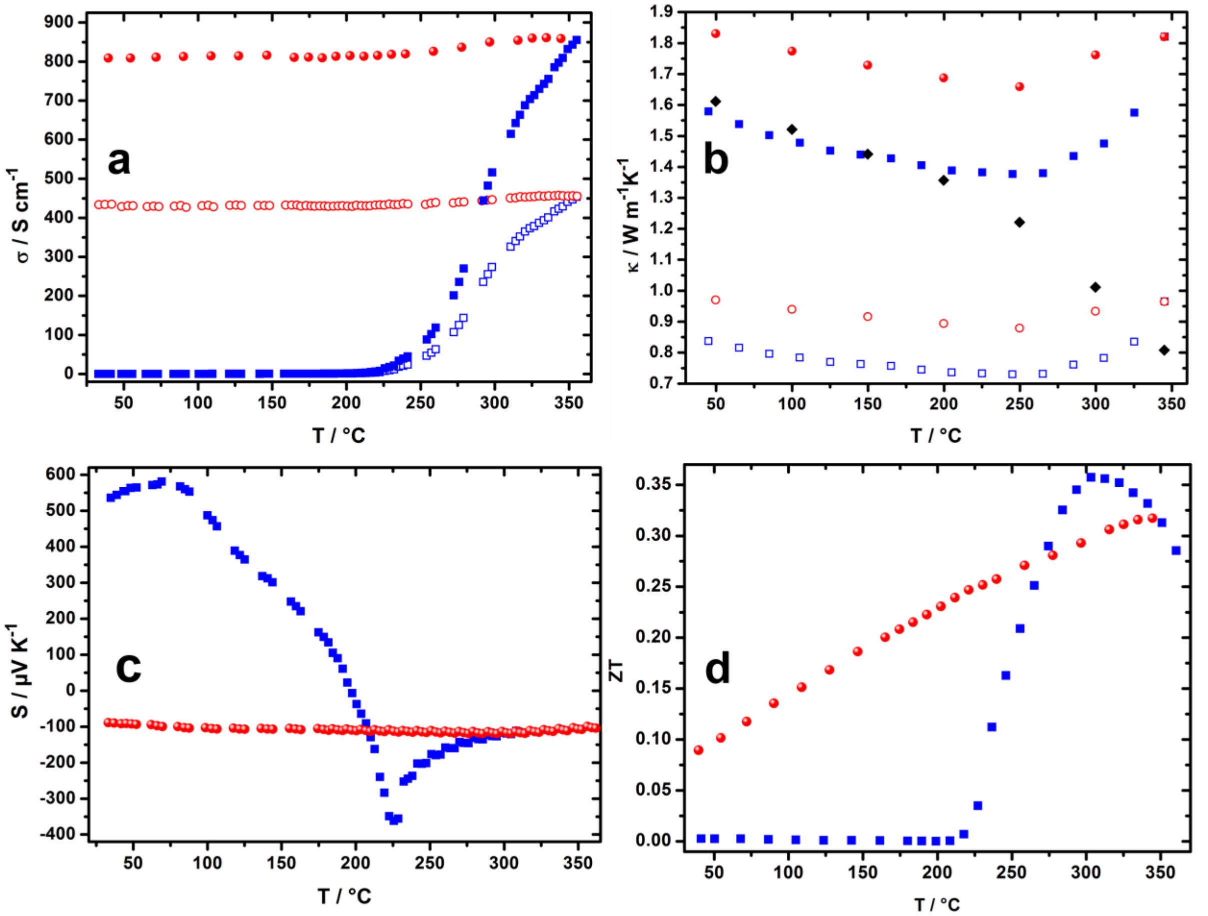

Figure E-7: Electric conductivity (**a**), thermal conductivity (**b**), thermopower (**c**) and thermoelectric figure of merit (**d**) of spark plasma sintered pellets of surface-oxidized PbTe-PbSe nanostars. All measurements have been carried out in two consecutive cycles. After the first measurement (**circles**), it was cooled to room temperature and the measurement repeated (**squares**). The raw measurements of σ and κ (**open symbols**) have been corrected for porosity (**full symbols**) as explained in the text. The lattice contribution to κ (**diamonds**) has been calculated from the second measurement as explained in the text.

The thermoelectric properties of sintered pellets of PbTe-PbSe nanostars are presented in **Figure** 7. Electric (σ) and thermal conductivity (κ) have been corrected for porosity as described for pure PbTe (P = 22 %, β = 2). Due to the large degree of porosity, these corrections were so significant that they are displayed together with the actually measured values for comparison. Thermopower (S) is known to be practically unaffected by porosity and was not corrected.[123] On using the measurements of σ, κ and S, ZT was calculated according to

$$ZT = \frac{\sigma S^2}{\kappa} T .$$

Since the corrections for porosity in σ and κ cancel in ZT, a correction to ZT is not necessary. Each measurement was performed in three cycles over the temperature range from 30 to 350 °C. The first two cycles are shown for each thermoelectric parameter. The third cycle was practically identical to the second cycle in all cases and is not shown.

In accordance with electric transport of pellets of sintered PbTe nanoparticles (**Fig. 5**), the pellets of sintered PbTe-PbSe nanostars show an equally low electric conductivity. With the elemental analysis in **Fig. 6g**, this is most likely due to surface oxidation, too. Any energy filtering effect from a small band edge offset between PbTe and PbSe would be invisible in **Fig. 7a** since the surface oxide barrier is by far the highest barrier. (See **Fig. S5** in the appendix.)

Although κ (**Fig. 7b**) appears to be low, the reduction is predominantly due to porosity which becomes apparent after applying a correction for porosity. With 1.6 $Wm^{-1}K^{-1}$, thermal conductivity at room temperature is twice as large as in the case of the nanostructured PbTe samples in **Fig. 5d**, which may be attributed to the larger particle diameter (75 nm *vs.* 30 nm). The remaining reduction in κ compared to bulk PbTe (2.2 $Wm^{-1}K^{-1}$) is due to combined effects of crystal boundary and ion impurity scattering.

Thermopower measurements (**Fig. 7c**) reveal a remarkable temperature dependence of the as-sintered PbTe-PbSe nanostars. At room temperature, S is practically identical to that of nanostructured surface oxidized PbTe (**Fig. 5b**). Presuming a surface oxide barrier of equal height, this result had to be expected. However, S decreases even more rapidly than for nanostructured PbTe, changes it sign to n-type at 200 °C, reaches a sharp turning point at 225 °C with a maximum of -360 μVK^{-1} and decreases to -100 μVK^{-1} above 300 °C. This should be viewed in the light of a sharp improvement in electric conductivity (**Fig. 7a**) beginning at 225 °C which terminates in an increase in σ by almost two orders of magnitude. This may be explained with two simultaneously operative processes:

(1) Thermally induced alloying of the two chalcogenide phases yields a single alloyed phase with degenerate semiconductor characteristics. Note that selenium is a good n-type dopant for PbTe. As the temperature rises, an increasing number of donor states are created close to the conduction band edge which is consecutively populated with carriers. This leads to a decrease in S since holes and electrons counteract each other and cancel their contribution to thermopower. At 200 °C the total S is zero but σ is still low since the amount of conduction band electrons needed to compensate those holes with sufficient energy to pass the oxide barrier between the valence bands is small. Between 200 and 225 °C, consecutive alloying lifts E_F close to the conduction band edge where the density of states is now quite large. This leads to a maximum in S and a beginning increase in σ. However, this decreases S since a significant number of mobile electrons on both sides of E_F is now available which cancel each other in their contribution to the total thermopower.

(2) Thermal annealing destroys the thin oxide layer on the surfaces of the material’s grains forming mere oxide islands within the conductive $PbTe_{1-x}Se_x$ matrix. This would drastically improve σ and decrease S since the potential barriers associated with the oxide and/or PbSe shell vanish simultaneously and no more energy filtering can take place. For the changes in microstructure due to thermal annealing see **Figure 8** below.

To test the material’s changed transport characteristics upon heating a second measurement has been performed over the entire temperature range after cooling down to room temperature. S and σ were almost independent of T and were reproducible on performing a third test run to verify performance stability in this temperature window. It can be concluded that the large temperature dependence of S and σ in the first measurement cycle is mainly a measure for the thermally induced solid state reaction which vanishes once the solid solution has been formed. Note that upon correcting σ for porosity, a room temperature value of over 800 Scm^{-1} is obtained which may be compared to 1200 Scm^{-1} of a bulk solid solution of $PbTe_{0.7}S_{0.3}$ published recently.[89]

κ is less affected by the alloying process and merely displays a moderate increase above 250 °C due to the increasing contribution by electron transport (κ_e). What appears to be a gain in κ when comparing the first and second measurement cycle is mostly the effect of permanently improved electric conductivity. This becomes apparent as the lattice contribution (κ_L) after alloying is estimated by applying the Wiedemann-Franz-law:

$$\kappa_L = \kappa - \kappa_e = \kappa - L\,\sigma\,T$$

with L = 2.0 x 10^{-8} V^2K^{-2} being the Lorentz constant. Note that particularly nanostructured materials can show large deviations of L from the value used here for heavily degenerate bulk semiconductors so this estimate should be handled with care.[124] However, it is intriguing to see that κ_L thus calculated from the data of the second measurement cycle matches the total κ of the first measurement cycle until the point where alloying adds a significant κ_e to the otherwise purely phononic total κ.

It may be concluded that, if any, the thermally induced alloying of PbTe-PbSe nanostars has a very small effect on κ_L. This is actually surprising as one would expect a large degree of impurity scattering and thus a decrease in κ_L.

For completeness the thermoelectric figure of merit (ZT, **Fig. 7d**) is displayed. Once electric conduction improves, ZT rises to up to 0.35 at 300 °C which is comparable to bulk $PbTe_{1-x}Se_x$. On repeating the measurement after alloying, ZT scales monotonously with T to ZT = 0.3 at 350°C.

In **Figure 8,** the crystallographic and structural changes in pellets of sintered surface oxidized PbTe-PbSe nanostars under the conditions applied during transport measurements are investigated. **Figure 8a** is an SEM image of the sample before the measurement. Individual nanostars appear to be well preserved and form a porous network. The SEM image in **Figure 8b** displays the fine structure of the sample after the first measurement cycle. Polyhedral particles of similar size have replaced the former nanostars. It is important to note that the unusually large thermopower of as-sintered surface oxidized PbTe-PbSe nanostars (**Fig. 7c**) is obviously not due to the small grain size but because of the potential barrier for intergrain transport provided by the oxidized surface. Mere grain boundary scattering by 50-100 nm grains of $PbTe_{1-x}Se_x$ is not sufficient to significantly increase S. What does increase S however is a barrier for charge carrier transport which could be due to two distinct effects: (I) An increase in the density of states by quantum confinement or (II) a depletion of the contribution of low-energy charge carriers to total thermopower. Both effects are known to increase S.[78,101] The exciton-Bohr-radii of PbTe and PbSe are 152 nm and 46 nm, respectively.[92,93] Thus, in the case of surface oxidized PbTe in this work, quantum confinement effects may be present whereas for surface oxidized PbTe-PbSe nanostars this is less probable. Since both materials show roughly the same thermopower, I speculate that quantum confinement does not play a significant role in either of the two materials. Instead, I believe that energy filtering by immobilizing low-energy holes due to a sink in the valence band edge is the operative mechanism.

It should be noted that most studies about thermopower enhancement by some scattering mechanism at grain boundaries have been carried out with nanostructured lead chalcogenides. Since the effects on S of grain boundary and potential barrier scattering are practically undistinguishable, the correct interpretation is somewhat academic in materials where both features are present. Due to the easily oxidized surfaces of lead chalcogenide nanostructures, this is the case for most materials studied so far. When extending this principle to other systems however, the findings in the present work have practical implications. I suggest to intentionally introduce suitable energy barriers for charge carrier transport rather than to merely rely on the effect of grain boundary scattering. The latter may be too weak to force significant enhancements in S.

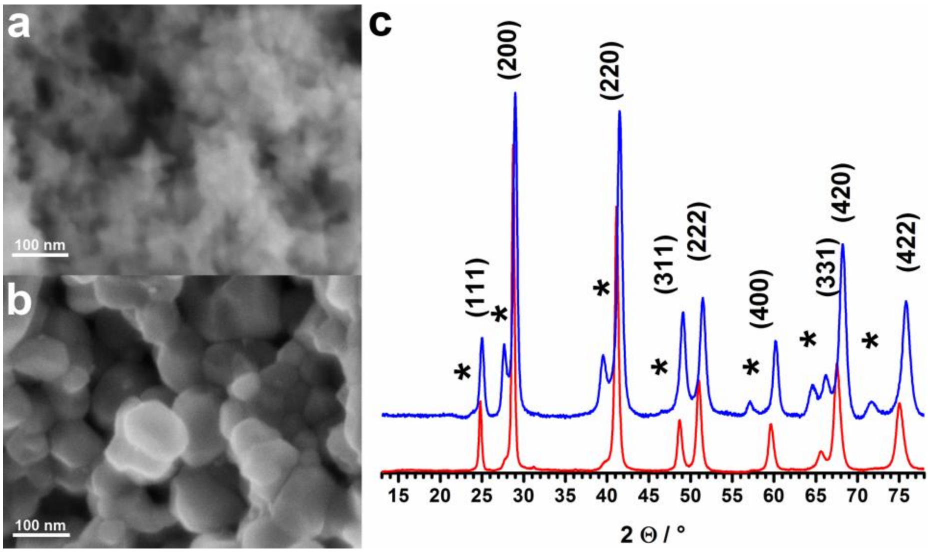

Figure E-8: SEM images of spark plasma sintered pellets of surface-oxidized PbTe-PbSe before **(a)** and after (**b**) the first measurement cycle**. (c)** XRPD of the pellet before (**top**) and after (**bottom**) the first measurement cycle. Indexing according to the rock salt structure. Reflections due to a pure PbTe phase are marked with an asterisk.

The XRPD patterns in **Figure 8c** investigate crystallographic changes during this process. For comparison, the XRPD pattern of thermally untreated surface oxidized PbTe-PbSe nanostars from **Figure 6i** is reproduced in the upper part. Indexing refers to twin reflections of the same lattice plane in PbTe and PbSe, respectively. PbTe reflections of the same index as their PbSe counterparts occur at smaller angles and are marked with an asterisk. In the lower part of **Fig. 8c**, the XRPD pattern of the same sample after transport measurements is displayed. Each pair of reflections has fused into one single reflection of similar intensity positioned at an intermediate angle. This supports the interpretation of transport measurements in terms of a thermally induced formation of a $PbTe_{1-x}Se_x$ solid solution. Upon more measurement cycles no significant changes in terms of structure and crystalline composition could be detected.

Based on the results of this work and the electronic structure displayed in **Fig. S5**, I propose the following core-shell material for future investigations: $PbTe_{1-x}Se_x$ with suitable n-type doping as the core material and pure PbSe as the shell. If we assume the position of the conduction band edge of the core to be between that of pure PbTe and PbSe, there would be a potential barrier to electron transport between 0 – 100 meV as one moves from the core to the shell based on the calculations of Wei and Zunger.[125] For hole transport, the situation at the band offset would be reversed so one may consider a shell made of pure PbTe. In both cases, any exposure to oxygen must be strictly avoided.

Conclusion

A nanostructured bulk material from monodisperse, octahedral PbTe nanoparticles with oxidized surfaces has been fabricated. This material shows an increased specific heat capacity as well as a decreased Debye temperature and lattice thermal conductivity as a result of the high surface to volume ratio. Oxidized surfaces on individual grains provide a barrier to hole transport. In effect, electric conductivity of this p-type semiconductor decreases by more than two orders of magnitude and room temperature thermopower is increased threefold. This is attributed to energy filtering by the oxide barrier rather than grain boundary scattering. A similar behavior is found for surface oxidized PbTe-PbSe core-shell nanostructures. By thermally induced alloying this material can be transformed from p-type to n-type on which electric transport improves greatly. The results of this work have practical implications for increasing thermopower by energy filtering in general and for designing lead chalcogenide based nanostructured thermoelectric materials in particular.

Methods

All manipulations were carried out under an inert atmosphere using standard Schlenck techniques if not stated otherwise.

(I) *Preparation of a 0.500 M solution of tellurium in TOP (Te@TOP)*

In a glovebox, tellurium (1.276 g, 10.00 mmol, 99.999 %, Chempur) and tetradecylphosphonic acid (102 mg, Alfa Aesar) were suspended in distilled TOP (20.0 mL, 90 %, Merck) under stirring. It was heated stepwise to 230 °C from room temperature by increasing the temperature by approximately 50 °C every thirty minutes. The final temperature was kept until a completely transparent, orange solution was obtained which turned to bright-yellow on cooling to room temperature. The solution was stored in the glovebox.

(II) *Synthesis of octahedral PbTe nanoparticles*

In a typical synthesis, lead acetate trihydrate (0.785 g, 2.07 mmol, 99 % Aldrich) was mixed with oleic acid (1.50 mL, 70 % Aldrich) and diphenylether (10 mL, 99 %, Fluka) and heated to 60 °C for 90 min under oil pump vacuum on which a transparent solution was obtained. (To ensure that acetic acid is absent in the reaction mixture at this point, it is essential to use a potent pump which can generate a vacuum of less than 0.1 mbar!) The flask was flooded with nitrogen, set to ambient pressure and it was heated to 170 °C on which trioctylphosphine (2.50 mL, 90 %, Aldrich) was added. Acetic acid (20 µL, 99 % Aldrich) was added, immediately followed by the quick injection of (**I**) (2.50 mL, 1.25 mmol) on which it was instantaneously cooled to 150 °C. (Note: For the synthesis of cubic PbTe nanoparticles, the addition of acetic acid has to be skipped.) The reaction was terminated by cooling to room temperature after 3.5 h.

(III) *Purification of PbTe nanoparticles for characterization*

A fraction of the brown-yellow solution obtained under **(II)** was mixed with ethanol (25 vol-%, analytical grade, Fluka) and centrifuged at 4500 rpm for 5 min. The light yellow supernatant was removed under nitrogen and the almost black precipitate suspended in a few drops of chloroform (analytical grade, Fluka) on which the washing cycle was repeated two more times. The purified PbTe nanoparticles should be stored in the absence of oxygen to prevent aging.

(**IV**) Ligand exchange (oleic acid → oleylamine)

The purified (**II**) was precipitated again by the addition of excess ethanol, the suspension centrifuged and the supernatant removed. The black precipitate was suspended in oleylamine (2 mL, 70 % Aldrich) and allowed to rest for 60 min. It was centrifuged, the supernatant removed and the black precipitate dissolved in chloroform. This procedure was repeated once with a resting time in fresh oleylamine of 10 min.

(V) *Preparation of a 1.000 M solution of selenium in TOP (Se@TOP)*

In a glovebox, selenium (1.579 g, 20.00 mmol, 99.999 %, Chempur) was suspended in distilled TOP (20.0 mL, 90 %, Merck) under stirring. It was heated to 200 °C until a completely transparent, colourless solution was obtained. The solution was stored in the glovebox.

(**VI**) *Synthesis of PbTe-PbSe nanostars*

Lead acetate trihydrate (0.785 g, 2.07 mmol, 99 % Aldrich) was mixed with oleic acid (1.50 mL, 70 % Aldrich) and diphenylether (10 mL, 99 %, Fluka). The solution prepared under (**IV**) of oleylamine-stabilized PbTe nanoparticles as obtained under (**I**) was added and it was heated to 60 °C for 90 min under oil pump to remove chloroform, acetic acid and H_2O. (To ensure that acetic acid is absent in the reaction mixture at this point, it is essential to use a potent pump which can generate a vacuum of less than 0.1 mbar!) The flask was flooded with nitrogen, set to ambient pressure and it was heated to 170 °C on which trioctylphosphine (3.0 mL, 90 %, Aldrich) was added, followed by acetic acid (20 µL, 99 % Aldrich). With a syringe pump, (**V**) (3.0 ml, 3.0 mmol) was slowly added to the dark-brown solution within 30 min (rate: 6.0 ml/h). After complete injection, the reaction temperature was lowered to

150 °C. The reaction was terminated by cooling to room temperature after 18 The PbTe-PbSe-nanostars were purified as described under (**III**).

(VII) *Ligand removal from PbTe- and PbTe-PbSe-nanostructures*

The purified **(II)** or **(VI)** was precipitated with ethanol, the supernatant removed after centrifugation and the black precipitate dried under vacuum. In a glovebox under nitrogen, the black solid was mixed with tetradecylphosphonic acid (20 mg, 98 % Merck) as well as chloroform (2 mL, analytical grade, Aldrich) and allowed to stir overnight on which a black suspension was formed. The supernatant was removed and it was washed three times with chloroform. The precipitate was suspended in a solution of NH_3 in methanol (2 mL, 7 mol L^{-1}, Aldrich). After stirring overnight, the supernatant was removed after centrifugation (4500 rpm, 5 min) and it was washed two times with fresh NH_3. Then, the precipitate was suspended in methanol (1 mL, analytical grade, Aldrich) and hexane (1 mL, analytical grade, Aldrich), followed by the addition of oxygen-free acetic acid (20 droplets). The hexane phase (the upper phase) was removed and fresh hexane added. This procedure was repeated until the hexane phase remained clear and colourless. All solvents were removed and the precipitate washed three times with methanol. On drying under vacuum overnight, a fine black powder was obtained. Typically, the starting amounts specified under **(II)** yield approximately 150 mg of PbTe nanoparticles and 380 mg of PbTe-PbSe nanostars for **(VI),** respectively.

(VIII) *Compaction of PbTe-nanoparticles and PbTe-PbSe-nanostars to pellets by spark plasma sintering*

Typically, 119 mg of **(VII)** kept under argon were loaded into a WC/Co die of 8.0 mm x 1.5 mm in area. The powder was pressed to a solid pellet of equal dimensions and approximately 1.5 mm in height by spark plasma sintering in a SPS-515 ET/M apparatus (Dr. Sinter®lab). For thermal conductivity measurements, 242 mg of **(VII)** were loaded into a disk-shape die of 6 mm in diameter to obtain a tablet of PbTe or PbTe-PbSe nanoparticles with 1.3 mm in height. On applying 340 MPa (for rectangular bars) or 530 MPa (for disks) pressure, the die containing the nanopowder was heated from 20 °C to 100 °C in 10.0 min with no hold time by applying a DC current between 0 – 165 A and immediately allowed to cool down to room temperature. The obtained PbTe or PbTe-PbSe nanoparticle pellets were mechanically robust and silver-metallic in appearance.

(HR-)TEM imaging was performed with a JEOL JEM 2200 FS (UHR) with CESCOR and CETCOR corrector at an acceleration voltage of 200 kV or a JEM-Jeol-1011 microscope at

100 kV with a CCD camera. SEM images were obtained on a LEO1550 scanning electron microscope with a spatial resolution of ~ 1 nm. XRPDs were recorded using a Philipps X`Pert-diffractometer with Bragg-Brentano-geometry on applying copper-K_α radiation (λ = 154.178 pm, U = 45 kV; I = 40 mA).

For measurements of the thermopower and resistivity a ZEM-3 apparatus (ULVAC-RIKO) was applied under a low-pressure helium atmosphere. The thermopower was determined by a static dc method where the resistivity was simultaneously measured by a four-terminal set-up.

The specific heat was measured by a relaxation technique in a Physical Property Measurement System by Quantum Design. A heat pulse of 2% of the bath temperature has been applied and repeated 3 times at each temperature.

Thermal diffusivity measurements were recorded with a Netzsch LFA-457 Microflash with a Pyroceram standard for calibration.

The appendix contains:

TEM images of cubic PbTe nanoparticles (**S1**). SPS temperature-time profiles and SEM images of resulting nanoparticle pellets (**S2**). Single particle selected area electron diffraction pattern of a PbTe-PbSe nanostar (**S3**). TEM images of PbSe nanoparticles (**S4**). Electronic structure of PbTe-PbSe-$Pb(O)_x$ core-shell-shell nanostars (**S5**).

Appendix to chapter E

Thermopower enhancement by energy filtering in lead chalcogenide core-shell nanostructures

Marcus Scheele[1,*], *Niels Oeschler*[2], *Igor Veremchuk*[2], *Sven-Ole Peters*[1], *Alexander Littig*[1], *Andreas Kornowski*[1], *Christian Klinke*[1], *and Horst Weller*[1]

[1]University of Hamburg, Institute of Physical Chemistry, Grindelallee 117, 20146 Hamburg, Germany

[2]Max Planck Institute of Chemical Physics of Solids, Noethnitzer Strasse 40, 01187 Dresden, Germany

Figure S1 should be compared to **Figure 1** to reveal the effect of acetic acid in controlling the shape of PbTe nanoparticles. In contrast to the particles in **Figure 1**, the particles shown below have been prepared under otherwise identical conditions but in the absence of acetic acid. Evidentially, acetic acid plays the key role in forcing the depletion of the {100} facets in favor of the {111} facets which eventually leads to the formation of octahedra. A suitable mechanism has been proposed by Houtepen et al. and is discussed in the main body of this work.[35] When acetic acid is absent, the thermodynamically more stable {100} facets persist and the crystals preserve their cubic shape.

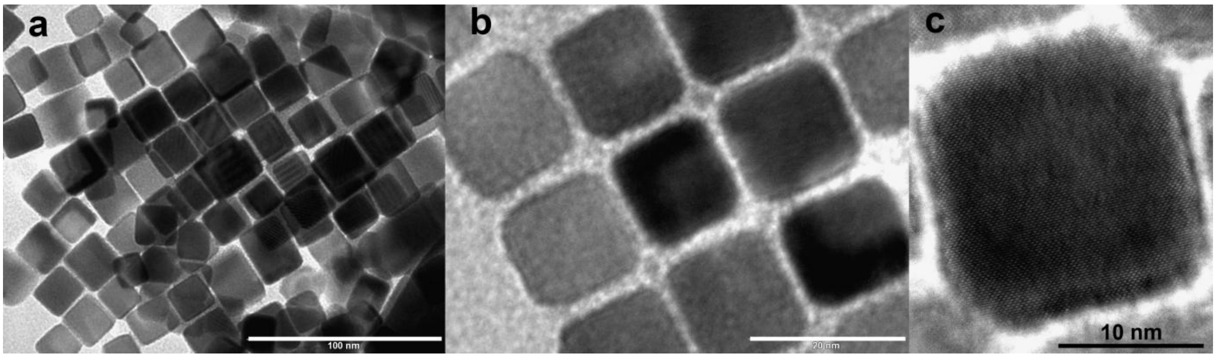

Figure E-S1: TEM images of cubic PbTe nanoparticles obtained according to **II** (see **Methods** section) if no acetic acid was added.

Figure S2 investigates the effect of different temperature-time profiles during spark plasma sintering experiments onto the morphology of the sintered nanoparticle pellets. Only when the samples are heated to 100 °C with no hold time (**Fig. S2 c**), the morphology of the individual nanoparticles can be preserved as depicted in **Figure 2** in the main body of the manuscript. As temperature and duration are increased, significant grain growth and irregular shapes are observed (**Fig. S2 a-b**). When interpreting temperature-time profiles of SPS experiments it is important to note that only the outside temperatures of the die can be measured. The actual temperature inside the sample is unknown and believed to be considerably higher.

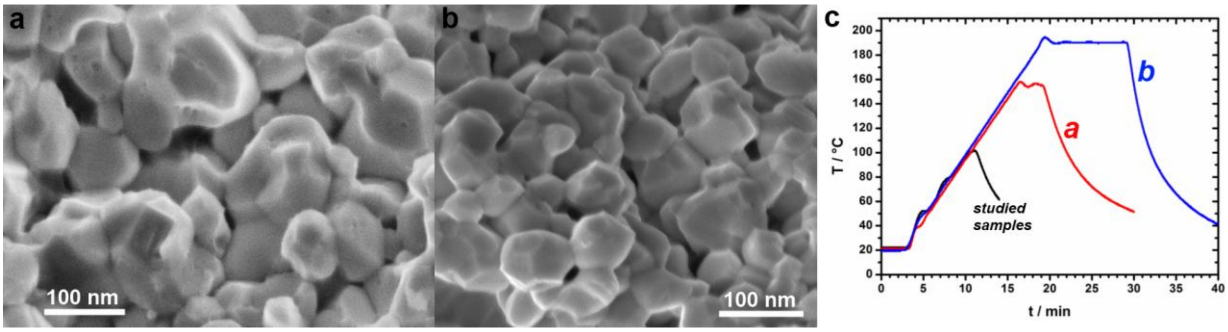

Figure E-S2: (a-b) SEM images of spark plasma sintered pellets of formerly octahedral PbTe nanoparticles obtained under the conditions specified in (**c**): The red profile yielded (**a**); the blue profile (**b**). The samples used for thermoelectric characterizations were obtained by the black profile. For an SEM image see **Figure 2**.

In **Figure S3**, the selected area electron diffraction pattern (**S3 b**) of an individual PbTe-PbSe nanostar (**S3 a**) is displayed. From the visible reflections, the direction of view is identified as the <111> direction which may be compared to **Figure 1f** in the main body of the manuscript. However, the crystal depicted below is obviously not phase pure as the (220) and (422) are seen to split up into two reflections each of slightly different lattice spacings. This should be compared to the XRPD pattern in **Figure 6** and the SAED pattern of pure PbTe nanoparticles in **Figure 1f**. The fact that the corresponding reflections of each phase are positioned in precisely the same crystallographic orientation is a strong hint that the growth of the second phase occurred epitaxially onto the primary phase.

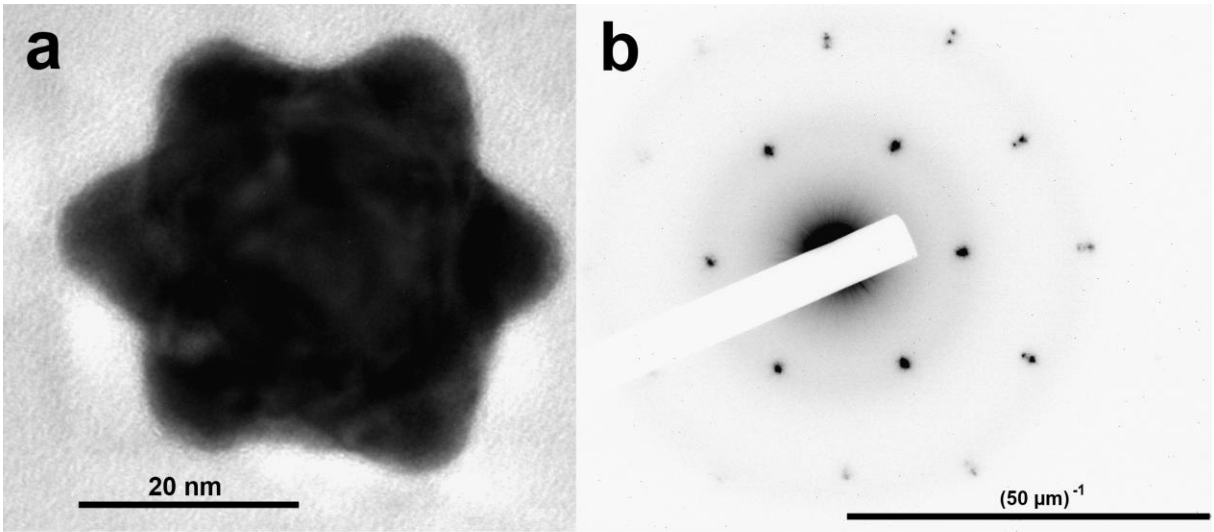

Figure E-S3: (a) TEM image of an individual PbTe-PbSe nanostar. (**b**) Selected area electron diffraction pattern of the individual PbTe-PbSe nanostar depicted in (**a**). Colors were inverted for clarity.

Figure S4 shows the crystal formation under the conditions specified in **VI** (see **Methods** in the main body of the manuscript) when PbTe nanocrystals are absent. It should be compared to the XRPD in **Fig. 6 l**. The conditions are obviously sufficient to nucleate PbSe nanoparticles, however with poor shape control. The structures appear to be agglomerates of many smaller particles which already resemble octahedral shapes but have not yet fully recrystallized. This is in accordance with investigations by Lu et al.[107]

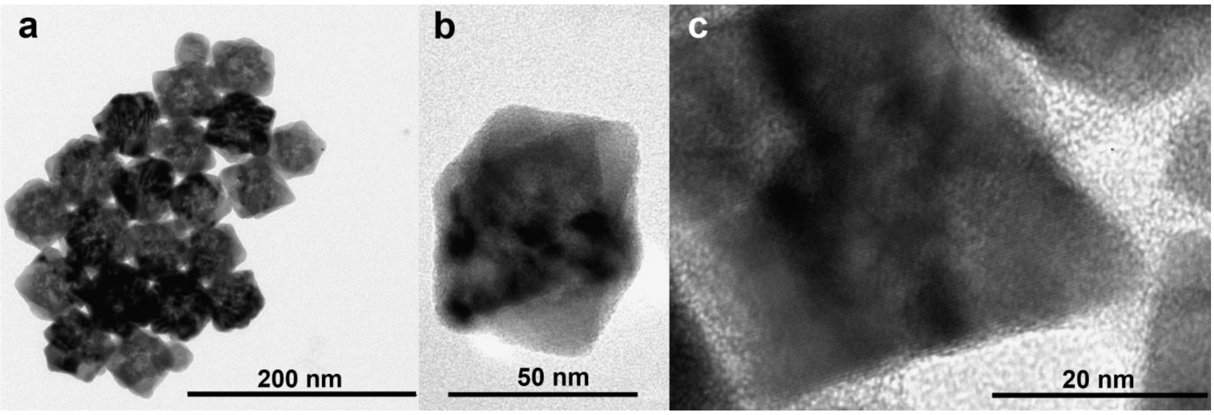

Figure E-S4: TEM images of PbSe nanoparticles obtained according to **VI (**see **Methods** section) in the absence of a solution of PbTe nanoparticles **(IV**).

On the band structure of PbTe-PbSe-Pb(O)x core-shell-shell nanostructures

PbTe and PbSe both crystallize in the rock salt structure with face-centered cubic arrangement. Their first Brillouin zones have eight equivalent L-points centered on each of the eight hexagonal facets of the Brillouin zones where the [111] axis intersect with the zone borders.[126] Below 450 K (700 K for PbSe), the conduction band minima (CBM) and valence band maxima (VBM) are located at the L-points giving eight degenerate electron and hole pockets, respectively. The energy gaps at the L-points are direct in both materials. For PbTe, it is 0.19 eV at 4.2 K and 0.31 eV at 300 K.[127] For PbSe, the values are 0.17 eV at 4.2 K and 0.27 eV at 300 K.[128] This illustrates the anomalous positive temperature coefficient of the band gap in PbTe and PbSe.[129] The direct band gap widens with increasing temperature leading to an unusual metallic like temperature dependence of electric transport. This is the combined result of lattice thermal expansions and the Debye-Waller effect. As the lattice expands with temperature, the kinetic energy is reduced due to the increased lattice constants. This lowers both, the CBM and VBM, in energy. However, one finds that the VBM is depressed at a faster rate than the CBM. This has been addressed to the unusual situation that in all PbX (X = S, Se or Te), the Pb 6s band is located below the valence band edge so that it is populated. In effect, there are strong repulsive forces between this 6s-band and bands of equal symmetry.[128] Since the band which carries the VBM at L is of the same symmetry as the Pb 6s band, it is promoted to higher energies by level repulsion. As the lattice is thermally expanded, the coupling weakens and the valence band moves down quickly in energy. This effect is less pronounced for the band carrying the CBM so the band gap widens.

Further, it has been shown that the conduction band in PbTe is composed to 83 % of Pb p character (72 % for PbSe).[129] Since the mean-squared displacements due to the Debye-Waller effect is seen to be much greater for Pb atoms than for Te atoms, the position of the CBM is strongly dependent on the Debye-Waller effect meaning that the CBM rises more quickly with temperature than the VBM.[130]

In combination, the CBM and VBM drift apart as temperature rises which explains the positive sign in the temperature coefficient of the band gap.

Above 450 K (700 K for PbSe), a second relative VBM at the Σ point is lifted in energy above the VBM at the L point, thus becoming the new principal VBM. Since the band carrying this new VBM is of different symmetry than the Pb 6s band, level repulsion is insignificant here and Egap is practically independent with temperature.

As a consequence of level repulsion the band edge ordering in PbX (X = S, Se or Te) is anomalous. When looking at the VBMs, one would expect the valence band edge of PbS to be the deepest since sulphur has the lowest p orbital energy of all three X. However, one finds exactly the opposite ordering with PbS having the highest and PbTe the lowest VBM. Since the PbS bond length is the shortest, level repulsion in PbS between the Pb 6s band and the valence band is the most pronounced which lifts the VBM above that of PbSe and PbTe.[128]

A slightly different argument applies when discussing the ordering of the CBMs. Intuitively, one would expect similar positions for all PbX since the conduction band has mainly Pb p character (up to 83 % for PbTe). Due to the presence of a band with equal symmetry slightly above the conduction band, there is some inherent level repulsion affecting the CBMs as well. One finds that the energy difference between these two bands is smallest for PbTe and largest for PbS. Consequently, the CBM in PbTe is the deepest.[128]

In effect, the band gaps of all three PbX are similar but there are considerable differences in the positions of the individual CBMs and VBMs. In the particular case of the offsets between PbTe and PbSe relevant for this work, both band edges of PbSe are positioned at higher energies than those for PbTe with a VBM offset of 0.12 eV and a CBM offset of 0.10 eV at 4.2 K.[128]

Lead oxides show large differences in their crystal properties and band structures as compared to the PbX compounds discussed above. To start with, there is a variety of compositions and crystalline phases with tetragonal and orthorhombic PbO being the most important members of the group.[130] The indirect band gap of the most stable phase at room temperature (tetragonal, "red" α-PbO) has been reported to 1.9 eV, where there is an additional direct band gap of 2.8 eV.[130,131,132] Above 760 K, PbO crystallizes in the orthorhombic ß-phase with a band gap of roughly 3.6 eV. The higher lead oxides have varying band gaps between 2.5 and 4.5 eV.

Little is known about the absolute energies of the band edges in these structures. For α-PbO, one finds a CBM at -4.0 eV and a VBM at -6.0 eV. At the point of the direct band gap, the VBM is supposed to be somewhat lower. For ß-PbO, there is a reported VBM at -6.4 eV and thus a CBM at roughly -2.8 eV. The absolute positions of the VBMs of the higher oxides vary between -3.8 and -5.9 eV.

These values should be compared to the band edges in PbTe and PbSe which have been derived by using PbS as a reference.[128,131] For PbSe, the CBM and VBM are positioned at -4.89 eV and -5.06 eV, respectively. For PbTe, the values are -4.99 eV and -5.18 eV, respectively. Thus on an absolute energy scale, the band edges of PbTe and PbSe lie within the band gap of most lead oxides so hole and electron transport should be greatly inhibited. In **Figure S5**, the relative positions of the band edges in PbTe-PbSe-Pb(O)x core-shell nanostars are illustrated. For a discussion of surface oxidized PbTe nanoparticles, the PbSe bands may be ignored. For comparison, the band edges of α- and β-PbO are displayed to illustrate the difference in electronic structure in between these two closely related compounds.

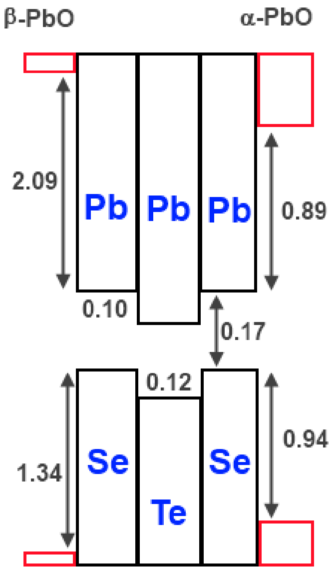

Figure E-S5: Relative band edge positions in PbTe-PbSe-Pb(O)x core-shell nanostars at 4.2 K as reported in literature.[128,131] All energies are in eV. For comparison, α- and β-PbO are displayed.

However, it must be emphasized that the electronic structure in **Figure S5** is derived from bulk crystals. As demonstrated by the XRPDs in **Figures 2** and **6**, the oxide phases at the surface of the PbTe or PbTe-PbSe nanostructures described in this work are either amorphous or so small that they cannot be detected by XRPD. In either case, the validity of the band edge positions known for bulk crystals is limited. Further, the figure does no account for the possible formations of chalcogenates although, amongst the discussed lead oxides, this is known to be an important by-product during lead chalcogenide oxidation.[133]

To conclude, it is likely that in the case of surface oxidized PbTe or PbTe-PbSe nanoparticles the band edges of PbX (X = Se or Te) are positioned in between the bandgap of the oxide layer but the exact positions remain unknown.

Acknowledgements

I would like to thank Prof. Dr. Horst Weller for the large degree of freedom allowed in the realization of this project. Without his financial support and open-minded attitude towards a previously unexplored subject, this work would not have been possible. The support in attending a variety of important international meetings as well as valuable guidance in the preparation of the manuscripts in this work is greatly appreciated.

I thank JProf. Dr. Christian Klinke for countless discussions and input on many aspects treated in this work. His advice on scientific writing has greatly improved my presentation skills. The Scanning Electron Microscopy images presented in this work have been acquired by him.

In continuation, I thank Dr. Niels Oeschler for establishing a truly fruitful collaboration without which none of the physical property measurements in this work would have been possible. This collaboration greatly extended my knowledge and skills in solid state physics.

I am indebted to the *Studienstiftung des deutschen Volkes* for six years of financial support throughout the course of my university career providing me with valuable independence and flexibility.

I thank Andreas Kornowski and Sylvia Bartholdi-Nawrath for advice on transmission electron microscopy imaging and the high-resolution TEM images in this work.

Katrin Meier and Dr. Igor Veremchuk are acknowledged for countless spark plasma sintering experiments and the development of the compaction procedure in this project.

It has been a pleasure to explore the limits of our X-ray diffraction system together with Almut Barck – not to mention all the nice conversations we had between experiments.

I was amazed by the knowledge of Frank Bürli who seems to have a solution for absolutely every imaginable electronic problem.

I would like to acknowledge Johannes Kimling, William Töllner and Prof. Dr. Kornelius Nielsch for help with differential scanning calorimetry and Laserflash experiments.

Klaus-Georg Reinsberg is thanked for the inductively coupled plasma optical emission spectroscopy experiments in **Chapter D**.

A very special thank you goes to my former trainees and students Nils Claassen, Elizabeth Ziemann, Saskia Scheel, Anna-Marlena Kreuziger, Alexander Littig, Sven-Ole Peters and Irina Fink whose pioneering experimental contributions formed the basis for this work.

Further, I thank Dr. Kathrin Hoppe for the very enjoyable time we had during the preparation of countless student seminaries.

Last but certainly not least, I would like to thank all my colleagues in the Weller group for three memorable years. All the best for your future guys!

Curriculum vitae

	Marcus Scheele
	Diploma in Chemistry
	*20. August 1981 in Duisburg
	Family status
	Unmarried, no children
	School
08/1992 - 06/2001	High school at the Albert-Schweitzer-Gymnasium in Hamburg, Germany
	Overseas visits during high school education
09/1998 - 06/1999	AS-Levels at the Colne College, Essex, England in Mathematics, Chemistry and Physics
	Social Service
09/2001 - 06/2002	Service for severely handicapped persons with *Hilfe im Haus* e.V. in Hamburg, Germany
	Job experience before University career
07/2002 - 09/2002	Work experience at the Institute of Chemistry of the Federal Research Centre for Forestry and Forest Products in Hamburg, Germany
	University
10/2002 - 03/2008	Diploma course in Chemistry, University of Hamburg
08/2004	Pre-diploma
09/2007	Diploma examination
10/2007 - 03/2008	Diploma thesis in the group of Prof. Horst Weller at the Institute of Physical Chemistry titled „*Synthesis of bismuth telluride nanoparticles*“
Since 05/2008	PhD course in Chemistry in the group of Prof. Horst Weller at the Institute of Physical Chemistry in Hamburg

Overseas visits during University career

09/2005	Language course in Spanish at the Salmínter Language School in Salamanca, Spain
10/2005 - 12/2005	Research visit at the Institute of Organometallic Chemistry with Prof. José Gimeno, Universidad Oviedo, Spain
04/2006 - 12/2006	Research visit at the Institute of Physical Chemistry with Prof. Paul Alivisatos, UC Berkeley, California, USA

Further education during University career

04/2003 - 01/2005	Two years of language courses in Spanish at the University of Hamburg
04/2007 - 01/2008	One year of language courses in Chinese (Mandarin) at the University of Hamburg
11/2009	Weekend seminar of the German Academic Foundation in “rethorics” for Ph.D. candidates in Bonn, Germany
02/2010	Weekend seminar of the Dr. Meyer Camberg Institute in „Presentation techniques“ in Munich, Germany

Attended conferences

07/2008	European Conference for thermoelectrics in Paris, France
08/2008	Workshop on Metal-Semiconductor-Hybride Nanostructures in Dresden, Germany
05/2009	Annual meeting of the Bunsen Society in Cologne, Germany
07/2009	International Conference for thermoelectrics in Freiburg, Germany
02/2010	Workshop on nanostructured thermoelectrics in Bad Honnef, Germany
04/2010	Spring meeting of the *Material Research Society* in San Francisco, CA, USA
07/2010	Gordon Conference on Solid State Chemistry in New London, NH, USA

	Awards
11/2004	e-fellows scholarship
12/2004	Award for the best pre-diploma of the semester in the department of Chemistry
03/2005	Full scholarship of the German Academic Foundation
10/2008	Ph.D. scholarship of the German Academic Foundation
07/2010	Award for outstanding teaching in the summer semester of 2010 by the Department of Chemistry Alumni of the University of Hamburg

Hamburg, 25.01.2011

Publications

Pascale Crochet; Mariano A. Fernández-Zúmel; Jose Gimeno; and Marcus Scheele, Efficient Redox Isomerization of Allylic Alcohols under Mild Conditions Catalyzed by Arene-Ruthenium(II) Complexes. *Organometallics* **2006**, *25*, 4846-4849.

Maxim V. Kovalenko; Marcus Scheele; and Dmitri V. Talapin, Colloidal Nanocrystals with Molecular Metal Chalcogenide Surface Ligands. *Science* **2009**, 324, 1417-1420.

Marcus Scheele; Niels Oeschler; Katrin Meier; Andreas Kornowski; Christian Klinke; and Horst Weller, Synthesis and Thermoelectric Characterization of Bi_2Te_3 Nanoparticles. *Adv. Funct. Mater.* **2009**, 19, 3476-83.

Marcus Scheele; Niels Oeschler; Katrin Meier; Andreas Kornowski; Christian Klinke; and Horst Weller, Colloidal Nanostructures as Building Blocks for Macroscopic Thermoelectric Materials with Electron-Crystal Phonon-Glass Properties. In *Thermoelectric Materials - Growth, Properties, Novel Characterization Methods, and Applications*; Tuller, H. L., Baniecki, J. D., Snyder, G. J., Malen, J. A., Eds.; Mater. Res. Soc. Symp. Proc. 1267, Warrendale, PA, **2010**, DD-08-12.

Maksym V. Kovalenko; Boris Spokoyny; Jong-Soo Lee; Marcus Scheele; Andrew Weber; Susanthri Perera; Daniel Landry; and Dmitri V. Talapin, Semiconductor Nanocrystals Functionalized with Antimony Telluride Zintl Ions for Nanostructured Thermoelectrics. *J. Am. Chem. Soc.* **2010**, 132, 6686–6695.

Marcus Scheele; Niels Oeschler; Igor Veremchuk; Klaus-Georg Reinsberg; Anna-Marlena Kreuziger; Andreas Kornowski; José Broekaert; Christian Klinke; and Horst Weller, ZT Enhancement in Solution-Grown $Sb_{(2-x)}Bi_xTe_3$ Nanoplatelets. *ACS Nano* **2010**, 4, 4283–4291.

Mariano A. Fernández-Zúmel; Beatriz Lastra-Barreira; Marcus Scheele; Josefina Díez; Pascale Crochet; and José Gimeno. Chiral phosphonite, phosphite and phosphoramidite η6-arene-ruthenium(II) complexes: application to the kinetic resolution of allylic alcohols. *Dalton Trans.*, **2010**, 39, 7780–7785.

Affirmation

Hiermit versichere ich an Eides statt, dass ich die vorliegende Arbeit selbst verfasst und alle verwendeten Hilfsmittel und Quellen als solche gekennzeichnet habe.
Diese Arbeit ist zuvor in gleicher oder ähnlicher Form keiner anderen Prüfungsbehörde zur Erlangung des Doktorgrades vorgelegt worden.
Ich bin erster und hauptverantwortlicher Autor der drei bereits erschienenen Publikationen aus Kapitel B, C und D. Mein Anteil an jeder der drei Veröffentlichungen in Bezug auf die experimentelle Arbeit und die Erstellung des Manuskripts lag jeweils bei 80 %.
Alle drei hier wiedergegebenen Manuskripte zeigen die von den Verlagen angenommenen und gedruckten Endversionen.

Hamburg, den 08.02.2011

Marcus Scheele

Hiermit wird bestätigt, dass Marcus Scheele erster und hauptverantwortlicher Autor der in dieser Arbeit in Kapitel B, C und D wiedergegebenen Veröffentlichungen ist. Sein Anteil am experimentellen und schriftlichen Gesamtaufwand betrug jeweils 80 %.

Hamburg, den 09.02.2011

Prof. Dr. Horst Weller

Risk and safety statements

Chemicals

Substance	Hazard symbol	R-phrases	S-phrases	Disposal
Bismuth(III) acetate	C, N	20/22-34-51/53	26-36/37/39-45-61	V
Chloroform	Xn	22-38-40-48/20/22	36/37	III
n-Hexane	Xn, N, F	11-38-48/20-51/53-62-65-67	9-16-29-33-36/37-61-62	IV
1-Dodecanethiol	Xi	36/37/38	26-28.1	IV
Lead(II) acetate trihydrate	T, N	61-33-48/22-50/53-62-	53-45-60-61	V
Oleylamine	C	34	26-45-36/37/39	IV
Tetradecyl-phosphonic acid	Xi	36/37/38	26/37	IV
Tellurium	T	25	22-28-45-36/37/39	V
Ethanol	F, Xi	11-36-67	7-16-24/25-26	IV
Trioctylphosphine	Xi	36/37/38	26-36	IV
Selenium	T	23/25-33-53	20/21-28-45-61	V
Ammonia	T, N	10-23-34-50	9-16-26-36/37/39-45-61	II
Methanol	F, T	11-23/24/25-39/23/24/25	7-16-36/37-45	IV
Acetic acid	C	10-35	23-26-45	I
Antimony(III) acetate	C, N	20/22-34-51/53	26-36/37/39-45-61	V
Hydrazine hydrate	T, N	45-20/21/22-34-43-51/53-50/53-23/24/25-10	53-45-60-61	II

Hazard symbols

C corrosive
E explosive
F$^+$ extremely flammable
F highly flammable
N dangerous to the environment
O oxidizing
T$^+$ very toxic

T toxic
Xi irritant
Xn harmful

Disposal keys

I container for aqueous acids

II container for aqueous bases

III container for halogenated organic solvents

IV container for non-halogenated organic solvents

V container for heavy-metal solids

Nature of special risks attributed to dangerous substances and preparations (R-phrases)

- R1: Explosive when dry
- R2: Risk of explosion by shock, friction, fire or other sources of ignition
- R3: Extreme risk of explosion by shock, friction, fire or other sources of ignition
- R4: Forms very sensitive explosive metallic compounds
- R5: Heating may cause an explosion
- R6: Explosive with or without contact with air
- R7: May cause fire
- R8: Contact with combustible material may cause fire
- R9: Explosive when mixed with combustible material
- R10: Flammable
- R11: Highly flammable
- R12: Extremely flammable
- R14: Reacts violently with water
- R15: Contact with water liberates extremely flammable gases
- R16: Explosive when mixed with oxidising substances
- R17: Spontaneously flammable in air
- R18: In use, may form flammable/explosive vapour-air mixture
- R19: May form explosive peroxides
- R20: Harmful by inhalation
- R21: Harmful in contact with skin
- R22: Harmful if swallowed
- R23: Toxic by inhalation
- R24: Toxic in contact with skin
- R25: Toxic if swallowed
- R26: Very toxic by inhalation
- R27: Very toxic in contact with skin
- R28: Very toxic if swallowed
- R29: Contact with water liberates toxic gas.
- R30: Can become highly flammable in use
- R31: Contact with acids liberates toxic gas
- R32: Contact with acids liberates very toxic gas
- R33: Danger of cumulative effects
- R34: Causes burns

- R35: Causes severe burns
- R36: Irritating to eyes
- R37: Irritating to respiratory system
- R38: Irritating to skin
- R39: Danger of very serious irreversible effects
- R40: Limited evidence of a carcinogenic effect
- R41: Risk of serious damage to eyes
- R42: May cause sensitisation by inhalation
- R43: May cause sensitisation by skin contact
- R44: Risk of explosion if heated under confinement
- R45: May cause cancer
- R46: May cause heritable genetic damage
- R48: Danger of serious damage to health by prolonged exposure
- R49: May cause cancer by inhalation
- R50: Very toxic to aquatic organisms
- R51: Toxic to aquatic organisms
- R52: Harmful to aquatic organisms
- R53: May cause long-term adverse effects in the aquatic environment
- R54: Toxic to flora
- R55: Toxic to fauna
- R56: Toxic to soil organisms
- R57: Toxic to bees
- R58: May cause long-term adverse effects in the environment
- R59: Dangerous for the ozone layer
- R60: May impair fertility
- R61: May cause harm to the unborn child
- R62: Possible risk of impaired fertility
- R63: Possible risk of harm to the unborn child
- R64: May cause harm to breast-fed babies
- R65: Harmful: may cause lung damage if swallowed
- R66: Repeated exposure may cause skin dryness or cracking
- R67: Vapours may cause drowsiness and dizziness
- R68: Possible risk of irreversible effects

Combination of R-phrases

- R14/15: Reacts violently with water, liberating extremely flammable gases
- R15/29: Contact with water liberates toxic, extremely flammable gases
- R20/21: Harmful by inhalation and in contact with skin
- R20/22: Harmful by inhalation and if swallowed
- R20/21/22: Harmful by inhalation, in contact with skin and if swallowed
- R21/22: Harmful in contact with skin and if swallowed
- R23/24: Toxic by inhalation and in contact with skin
- R23/25: Toxic by inhalation and if swallowed
- R23/24/25: Toxic by inhalation, in contact with skin and if swallowed
- R24/25: Toxic in contact with skin and if swallowed
- R26/27: Very toxic by inhalation and in contact with skin
- R26/28: Very toxic by inhalation and if swallowed
- R26/27/28: Very toxic by inhalation, in contact with skin and if swallowed
- R27/28: Very toxic in contact with skin and if swallowed

- R36/37: Irritating to eyes and respiratory system
- R36/38: Irritating to eyes and skin
- R36/37/38: Irritating to eyes, respiratory system and skin
- R37/38: Irritating to respiratory system and skin
- R39/23: Toxic: danger of very serious irreversible effects through inhalation
- R39/24: Toxic: danger of very serious irreversible effects in contact with skin
- R39/25: Toxic: danger of very serious irreversible effects if swallowed
- R39/23/24: Toxic: danger of very serious irreversible effects through inhalation and in contact with skin
- R39/23/25: Toxic: danger of very serious irreversible effects through inhalation and if swallowed
- R39/24/25: Toxic: danger of very serious irreversible effects in contact with skin and if swallowed
- R39/23/24/25: Toxic: danger of very serious irreversible effects through inhalation, in contact with skin and if swallowed
- R39/26: Very Toxic: danger of very serious irreversible effects through inhalation
- R39/27: Very Toxic: danger of very serious irreversible effects in contact with skin
- R39/28: Very Toxic: danger of very serious irreversible effects if swallowed
- R39/26/27: Very Toxic: danger of very serious irreversible effects through inhalation and in contact with skin
- R39/26/28: Very Toxic: danger of very serious irreversible effects through inhalation and if swallowed
- R39/27/28: Very Toxic: danger of very serious irreversible effects in contact with skin and if swallowed
- R39/26/27/28: Very Toxic: danger of very serious irreversible effects through inhalation, in contact with skin and if swallowed
- R42/43: May cause sensitization by inhalation and skin contact
- R48/20: Harmful: danger of serious damage to health by prolonged exposure through inhalation
- R48/21: Harmful: danger of serious damage to health by prolonged exposure in contact with skin
- R48/22: Harmful: danger of serious damage to health by prolonged exposure if swallowed
- R48/20/21: Harmful: danger of serious damage to health by prolonged exposure through inhalation and in contact with skin
- R48/20/22: Harmful: danger of serious damage to health by prolonged exposure through inhalation and if swallowed
- R48/21/22: Harmful: danger of serious damage to health by prolonged exposure in contact with skin and if swallowed
- R48/20/21/22: Harmful: danger of serious damage to health by prolonged exposure through inhalation, in contact with skin and if swallowed
- R48/23: Toxic: danger of serious damage to health by prolonged exposure through inhalation
- R48/24: Toxic: danger of serious damage to health by prolonged exposure in contact with skin
- R48/25: Toxic: danger of serious damage to health by prolonged exposure if swallowed
- R48/23/24: Toxic: danger of serious damage to health by prolonged exposure through inhalation and in contact with skin
- R48/23/25: Toxic: danger of serious damage to health by prolonged exposure through inhalation and if swallowed

- R48/24/25: Toxic: danger of serious damage to health by prolonged exposure in contact with skin and if swallowed
- R48/23/24/25: Toxic: danger of serious damage to health by prolonged exposure through inhalation, in contact with skin and if swallowed
- R50/53: Very toxic to aquatic organisms, may cause long-term adverse effects in the aquatic environment
- R51/53: Toxic to aquatic organisms, may cause long-term adverse effects in the aquatic environment
- R52/53: Harmful to aquatic organisms, may cause long-term adverse effects in the aquatic environment
- R68/20: Harmful: possible risk of irreversible effects through inhalation
- R68/21: Harmful: possible risk of irreversible effects in contact with skin
- R68/22: Harmful: possible risk of irreversible effects if swallowed
- R68/20/21: Harmful: possible risk of irreversible effects through inhalation and in contact with skin
- R68/20/22: Harmful: possible risk of irreversible effects through inhalation and if swallowed
- R68/21/22: Harmful: possible risk of irreversible effects in contact with skin and if swallowed
- R68/20/21/22: Harmful: possible risk of irreversible effects through inhalation, in contact with skin and if swallowed

Safety advice concerning dangerous substances and preparations (S-phrases)

- (S1): Keep locked up
- (S2): Keep out of the reach of children
- S3: Keep in a cool place
- S4: Keep away from living quarters
- S5: Keep contents under ... (*appropriate liquid to be specified by the manufacturer*)
- S6: Keep under ... (*inert gas to be specified by the manufacturer*)
- S7: Keep container tightly closed
- S8: Keep container dry
- S9: Keep container in a well-ventilated place
- S10: Keep contents wet
- S11: Avoid contact with air
- S12: Do not keep the container sealed
- S13: Keep away from food, drink and animal foodstuffs
- S14: Keep away from ... (*incompatible materials to be indicated by the manufacturer*)
- S15: Keep away from heat
- S16: Keep away from sources of ignition - No smoking
- S17: Keep away from combustible material
- S18: Handle and open container with care
- S20: When using do not eat or drink
- S21: When using do not smoke
- S22: Do not breathe dust
- S23: Do not breathe gas/fumes/vapour/spray (*appropriate wording to be specified by the manufacturer*)
- S24: Avoid contact with skin
- S25: Avoid contact with eyes

- S26: In case of contact with eyes, rinse immediately with plenty of water and seek medical advice
- S27: Take off immediately all contaminated clothing
- S28: After contact with skin, wash immediately with plenty of ... (*to be specified by the manufacturer*)
- S29: Do not empty into drains
- S30: Never add water to this product
- S33: Take precautionary measures against static discharges
- S35: This material and its container must be disposed of in a safe way
- S36: Wear suitable protective clothing
- S37: Wear suitable gloves
- S38: In case of insufficient ventilation wear suitable respiratory equipment
- S39: Wear eye/face protection
- S40: To clean the floor and all objects contaminated by this material use ... (*to be specified by the manufacturer*)
- S41: In case of fire and/or explosion do not breathe fumes
- S42: During fumigation/spraying wear suitable respiratory equipment (*appropriate wording to be specified by the manufacturer*)
- S43: In case of fire use ... (*indicate in the space the precise type of fire-fighting equipment. If water increases the risk add -* ***Never use water***)
- S45: In case of accident or if you feel unwell seek medical advice immediately (show the label where possible)
- S46: If swallowed, seek medical advice immediately and show this container or label
- S47: Keep at temperature not exceeding ... °C (*to be specified by the manufacturer*)
- S48: Keep wet with ... (*appropriate material to be specified by the manufacturer*)
- S49: Keep only in the original container
- S50: Do not mix with ... (*to be specified by the manufacturer*)
- S51: Use only in well-ventilated areas
- S52: Not recommended for interior use on large surface areas
- S53: Avoid exposure - obtain special instructions before use
- S56: Dispose of this material and its container at hazardous or special waste collection point
- S57: Use appropriate containment to avoid environmental contamination
- S59: Refer to manufacturer/supplier for information on recovery/recycling
- S60: This material and its container must be disposed of as hazardous waste
- S61: Avoid release to the environment. Refer to special instructions/safety data sheet
- S62: If swallowed, do not induce vomiting: seek medical advice immediately and show this container or label
- S63: In case of accident by inhalation: remove casualty to fresh air and keep at rest
- S64: If swallowed, rinse mouth with water (only if the person is conscious)

Combination of S-phrases

- (S1/2): Keep locked up and out of the reach of children
- S3/7: Keep container tightly closed in a cool place
- S3/7/9: Keep container tightly closed in a cool, well-ventilated place
- S3/9/14: Keep in a cool, well-ventilated place away from ... (*incompatible materials to be indicated by the manufacturer*)
- S3/9/14/49: Keep only in the original container in a cool, well-ventilated place away from ... (*incompatible materials to be indicated by the manufacturer*)

- S3/9/49: Keep only in the original container in a cool, well-ventilated place
- S3/14 Keep in a cool place away from ... (*incompatible materials to be indicated by the manufacturer*)
- S7/8: Keep container tightly closed and dry
- S7/9: Keep container tightly closed and in a well-ventilated place
- S7/47: Keep container tightly closed and at temperature not exceeding ... °C (*to be specified by the manufacturer*)
- S8/10: Keep container wet, but keep the contents dry
- S20/21: When using do not eat, drink or smoke
- S24/25: Avoid any inhalation, contact with skin and eyes. Wear suitable protective clothing and gloves
- S27/28: After contact with skin, take off immediately all contaminated clothing, and wash immediately with plenty of ... (*to be specified by the manufacturer*)
- S29/35: Do not empty into drains; dispose of this material and its container in a safe way
- S29/56: Do not empty into drains, dispose of this material and its container at hazardous or special waste collection point
- S36/37: Wear suitable protective clothing and gloves
- S36/37/39: Wear suitable protective clothing, gloves and eye/face protection
- S36/39: Wear suitable protective clothing and eye/face protection
- S37/39: Wear suitable gloves and eye/face protection
- S47/49: Keep only in the original container at temperature not exceeding ... °C (*to be specified by the manufacturer*)

References

---

[1] Lundstrom, M., *Fundamentals of Carrier Transport*, 2nd Ed., Cambridge University Press **2009**, p.165.

[2] Nolas, G.S.; Sharp, J.; Goldsmid, H. J., *Thermoelectrics- Basic Principles and new materials developments*; Springer Press **2001**; p. 42.

[3] Callaway, J., *Phys. Rev.* **1959**, 113, 1046-1051.

[4] Asen-Palmer, M.; Bartkowski, K.; Gmelin, E.; Cardona, M.; Zhernov, A., P.; Inyushkin, A. V.; Taldenkov, A.; Ozhogin, V. I..; Itoh, K.; Haller, E., *Phys. Rev. B.* **1997**, 56, 9431-9447.

[5] Steigmeier, E. F.; Abeles, B., *Phys. Rev.* **1964**, 136, A1149-A1155.

[6] Tamura, S., *Phys. Rev. B.* **1983**, 27, 858-866.

[7] Klemens, P. G., *Proc. R. Soc. London Ser. A* **1951**, 208, 108.

[8] Herring, C., *Phys. Rev.* **1954,** 95, 954-965.

[9] Klemens, P. G., *Proc. Phys. Soc. London Ser. A* **1955**, 68, 1113-1128.

[10] Morelli, D.; Heremans, J.; Slack, G., *Phys. Rev. B.* **2002**, 66, 1-9.

[11] Peierls, R. E., *Ann. Phys.* **1929**, 3, 1055.

[12] Lee, S. J.; Shin, N. H.; Kot, J. J.; Parkt, M. J.; and Kümmel, R., *Semicond. Sci. Technol.* **1992**, 7, 1072-1079.

[13] Hicks, L. D.; Dresselhaus, M. S., *Phys. Rev. B.* **1993**, 47, 12727-12731.

[14] Hicks, L. D.; Dresselhaus, M. S., *Phys. Rev. B.* **1993**, 47, 16631-16634.

[15] Casimir, H. B. G., *Physica* **1938**, 5, 495-500.

[16] Moore, A. L.; Saha, S. K.; Prasher, R. S.; Shi, L., *Appl. Phys. Lett*. **2008**, *93*, 083112-3.

[17] Zhu, Y. F.; Lian, J. S.; Jiang, Q. *J. Phys. Chem. C*. **2009**, *113*, 16896-16900.

---

[18] Poudel, B.; Hao, Q.; Ma, Y.; Lan, Y.; Minnich, A.; Yu, B.; Yan, X.; Wang, D.; Muto, A.; Vashaee, D.; Chen, X.; Liu, J.; Dresselhaus, M. S.; Chen, G.; Ren, Z., *Science* **2008,** *320,* 634-638.

[19] Minnich, A. J.; Dresselhaus, M. S.; Ren, Z. F.; Chen, G., *Energy Environ. Sci*. **2009**, *2,* 466-479.

[20] Heremans, J.; Thrush, C.; Morelli, D., *Phys. Rev. B*. **2004**, *70,* 115334-5.

[21] Mahan, G. D.; Sofo, J. O., *Proc. Nat. Acad. Sci*. **1996**, *93,* 7436-9.

[22] Martin, J.; Wang, L.; Chen, L.; Nolas, G. *Phys. Rev. B*. **2009**, *79*, 115311-5.

[23] Seto, J. Y. W., *J. Appl. Phys.* **1975**, 46, 5247-5254.

[24] Ravich, Yu. I.; Efimova, B. A.; Tamarchenko, V. I., *Phys. Stat. Sol. (B)* **1971**, 43, 453-469.

[25] Vasilevskiy, D.; Turenne, S.; Masut, R. A.; Andre, C., *J. Electronic Mater*. **2009**, *38,* 1061-1067.

[26] Sootsman, J. R.; Kong, H.; Uher, C.; D’Angelo, J. J.; Wu, C.-I.; Hogan, T. P.; Caillat, T.; Kanatzidis, M. G., *Angew. Chem. Int. Ed*. **2008**, 47, 8618-22.

[27] Wang, R. Y.; Feser, J. P.; Lee, J.-S.; Talapin, D. V.; Segalman, R.; Majumdar, A., *Nano lett*. **2008**, *8*, 2283-8.

[28] Popescu, A.; Woods, L. M.; Martin, J.; Nolas, G. S., *Phys. Rev. B*. **2009**, 79, 205302-7 .

[29] Vashaee, D.; Shakouri, A., *Phys. Rev. Lett*. **2004**, 92, 106103-4.

[30] Chasmar, R. P.; Stratton, R., *J. Electron. Control.* **1959**, 7, 52-72.

[31] Slack, G. A. and Tsoukala, V. G., *J. Appl. Phys.* **1994**, 76, 1665-1671.

[32] LaMer, V. K.; Dinegar, R. H., *J. Am. Chem. Soc.* **1950**, 72, 4847-4854.

[33] Dirmyer, M. R.; Martin, J.; Nolas, G. S.; Sen, A.; Badding, J. V., *Small* **2009**, 5, 933-937.

[34] Zhang, J.; Kumbhar, A.; He, J.; Das, N. C.; Yang, K.; Wang, J.-Q.; Wang, H.; Stokes, K. L.; and Fang, J., *J. Am. Chem. Soc.* **2008**, 130, 15203–15209.

---

[35] Houtepen, A. J.; Koole, R.; Vanmaekelbergh, D.; Meeldijk, J.; Hickey, S. G. *J. Am. Chem. Soc*. **2006**, *128*, 6792-3.

[36] Cho, K.-S.; Talapin, D. V.; Gaschler, W.; and Murray, C. B., *J. Am. Chem. Soc.* **2005**, 127, 7140-7147.

[37] Yashina, L. V.; Zyubina, T. S.; Pu, R.; Zyubin, A. S.; Shtanov, V. I.; Tikhonov, E. V. *J. Phys. Chem. C*. **2008**, 19995-20006.

[38] M. H. Ettenberg, W. A. Jesser, and F. D. Rosi, in *Proc. 15th Int. Conf. on Thermoelectrics* (ed. T. Caillat), IEEE, Piscataway, NJ, **1996,** 52-56

[39] L. D. Hicks, T. C. Harman, X. Sun, M. S. Dresselhaus, *Phys. Rev. B* **1996**, *53* (16), 10493

[40] A. Kitun, A. Balandin, J. L. Liu, and K. L. Wang, *J. Appl. Phys*. **2002**, *88* (2), 696

[41] M. S. Dresselhaus, Y.-M. Lin, S. B. Cronin, M. R. Black, O. Rabin, and G. Dresselhaus, *Nonlithographic and Lithographic Methods for Nanofabrication: Symposium Proceedings* , (ed. S. Smith), Technomic Publishing Co., Inc., Lancaster, PA **2001**

[42] R. Venkatasubramanian, E. Siiwvola, T. Colpitts and B. O’Quinn, *Nature* **2001**, *413***,** 597

[43] T. C. Harman, P. J. Taylor, M. P. Walsh, B. E. LaForge, *Science* **297**, 2229 (2002)

[44] N. Gothard, X. Ji, J. He, and T. M. Tritt, *J. Appl. Phys.* **2008**, *103,* 054314

[45] M. Tokita, *J. Soc. Powder Techn. Jpn*. **1993**, *30,* 790

[46] W. Lu, Y. Ding, Y. Chen, Z. L. Wang, and J. Fang, *J. Am. Chem. Soc*. **2005**, *127,* 10112

[47] A. Purkayastha, S. Kim, D. D. Gandhi, P. G. Ganesan, T. Borca-Tasciuc, and G. Ramanath, *Adv. Mater.* **2006**, *18*, 2958

[48] A. Purkayastha, Q. Yan, M. S. Raghuveer, D. D. Gandhi, H. Li, Z. W. Liu, R. V. Ramanujan, T. Borca-Tasciuc, and G. Ramanath, *Adv. Mater***. 2008**, *20,* 2679

[49] J. W. G. Bos, H. W. Zandbergen, M.-H. Lee, N. P. Ong, and R. J. Cava, *Phys. Rev. B* **2007**, *75*, 195203

[50] M. V. Kovalenko, M. Scheele, D. V. Talapin, *Science* **2009**, 324, 1417

[51] A. Glatz, I. S. Beloborodov, *Phys. Rev. B* **2009**, *79*, 041404(R)

---

[52] D. C. K. MacDonald, E. Mooser, W. B. Pearson, I. M. Templeton, and S. B. Woods, *Philos. Mag*. **1959**, *4* (40), 433

[53] F. Wang, R. Tang, Y. Heng, P. Gibbons, and W. Buhro, *Chem Mater*. **2008**, 20, 3656

[54] M. S. Nikolić, M. Krack, V. Aleksandrovic, A. Kornowski, S. Förster, H. Weller, *Angew. Chem.*, 118, 6727 (**2006**)

[55] Wang, W. Z.; Poudel, B.; Wang, D. Z.; Ren, Z. F., *Adv. Mater.* **2005**, 17, 2110.

[56] LaMer, V. K.; Dinegar, R. H., *J. Am. Chem. Soc.* **1950**, 72, 4847.

[57] Talapin, D. V.; Lee, J.-S.; Kovalenko, M. V.; and Shevchenko, E. V., *Chem. Rev.* **2010**, 110, 389.

[58] Huang, B. L.; Kaviany, M., *Phys Rev. B* **2008**, 77, 125209.

[59] *Landholt-Bornstein*. O. Madelung, M. Schulz and H. Wiess. Berlin, Springer-Verlag. 17f: various (**1983**).

[60] Goldsmid, H. J.; Douglas, R. W., *Brit. J. Appl. Phys*. **1954,** 5, 386-390.

[61] Xie, W.; Tang, X.; Yan, Y.; Zhang, Q.; and Tritt, T. M., *J. Appl. Phys*. **2009**, 105, 113713-8.

[62] Lan, Y.; Poudel, B.; Ma, Y.; Wang, D.; Dresselhaus, M. S;. Chen, G.; and Ren, Z., *Nano lett.* **2009**, 9, 1419-22.

[63] Zhao, Y.; Burda, C., *ACS Appl. Mater. Inter.* **2009**, 1, 1259-63.

[64] **Chapter B**: Scheele, M.; Oeschler, N.; Meier, K.; Kornowski, A.; Klinke, C.; and Weller, H., *Adv. Funct. Mater.* **2009**, 19, 3476-83.

[65] Zebarjadi, M.; Esfarjani, K.; Shakouri, A.; Bahk, J.-H.; Bian, Z.; Zeng, G.; Bowers, J.; Lu, H.; Zide, J.; and Gossard, A., *Appl. Phys. Lett*. **2009**, 94, 202105-3.

[66] Zhang, H; Liu, C.-X.; Qi, X.-L.; Dai, X.; Fang, Z.; and Zhang, S.-C., *Nat. Phys.* **2009**, 5, 438-442.

[67] Chiritescu, C.; Mortensen, C.; Cahill, D. G.; Johnson, D.; and Zschack, P., *J. Appl. Phys.* **2009**, 106, 073503-5.

---

[68] Teweldebrhan, D; Goyal, V; and Balandin, A. A., *Nano Lett.* **2010**, 10, 1209-1218.

[69] Kong, D.; Dang, W.; Cha, J., J.; Li, H.; Meister, S.; Peng, H.; Liu, Z.; and Cui, Y., *Nano Lett.* **2010**, 10, 2245-2250.

[70] Wang, W.; Poudel, B.; Yang, J.; Wang, D. Z.; and Ren, Z. F., *J. Am. Chem. Soc.* **2005**, 127, 13792-93.

[71] Rupp, J; Birringer, R., *Phys. Rev. B* **1987**, 36, 7888-7890.

[72] Shrivastava, K. N., *Nano lett.* **2002**, 2, 21-24.

[73] Fleurial, J. P.; Gailliard, L.; Triboulet, R.; Scherrer, H.; and Scherrer, S., *J. Phys. Chem. Solids* ***1988***, 49, 1237-47.

[74] Ma, Y.; Hao, Q.; Poudel, B.; Lan, Y.; Yu, B.; Wang, D.; Chen, G.; and Ren, Z., *Nano lett.* **2008**, 8, 2580-84.

[75] Gesele, G.; Linsmeier, J.; Drach, V.; Fricke, J.; and Arens-Fischer, R., *J. Physics D* **1997**, 30, 2911-16.

[76] Sumirat, I.; Ando, Y.; and Shimamura, S., *J. Porous Mater.* **2006**, 13, 439-443.

[77] Kamins, T. I., *J. Appl. Phys.* **1971**, 42, 4357-65.

[78] Cao, Y. Q.; Zhao, X. B.; Zhu, T. J.; Zhang, X. B.; and Tu, J. P., *Appl. Phys. Lett.* **2008**, 92, 143106-3.

[79] Yu, F.; Zhang, J.; Yu, D.; He, J.; Liu, Z.; Xu, B.; and Tian, Y., *J. Appl. Phys.* **2009**, 105, 094303-5.

[80] Zhao, L.-D.; Zhang, B.-P.; Liu, W.-S.; and Li, J.-F., *J. Appl. Phys.* **2009**, 105, 023704-6.

[81] Dughaish, Z. H., *Physica B* **2002**, 322, 205–223.

[82] Snyder, G. J.; and Toberer, E. S., *Nat. Mater.* **2008**, 7, 105-113.

[83] Lan, Y.; Minnich, A. J.; Chen, G.; and Ren, Z., *Adv. Funct. Mater.* **2009**, 19, 1-20.

[84] Cao, Y. Q.; Zhu, T. J.; and Zhao, X. B., *J. Phys. D: Appl. Phys.* **2009**, 42, 015406

---

[85] Ikeda, T.; Collins, L. A.; Ravi, V. A.; Gascoin, F. S.; Haile, S. M.; and Snyder, G. S., *Chem. Mater.* **2007**, 19, 763-767

[86] Hsu, K. F.; Loo, S.; Guo, F.; Chen, W.; Dyck, J. S.; Uher, C.; Hogan, T.; Polychroniadis, E. K.; and Kanatzidis, M. G., *Science* **2004**, 303, 818-821.

[87] Sootsman, J. R.; Pcionek, R. J.; Kong, H. J.; Uher, C.; Kanatzidis, M. G., *Chem. Mater.* **2006**, 18, 4993–4995.

[88] Androulakis, J.; Lin, C. H.; Kong, H. J.; Uher, C.; Wu, C.; Hogan, T.; Cook, B. C. ; Caillat, T.; Paraskevopoulos, K. M., *J. Am. Chem. Soc.* **2007**, 192, 9780.

[89] He, J.; Girard, S. N.; Kanatzidis, M. G.; and Dravid, V. P., *Adv. Funct. Mater.* **2010**, 20, 764-772.

[90] Kanatzidis, M. G., *Chem. Mater***.** **2010**, 22, 648–659.

[91] Heremans, J. P.; Jovovic, V.; Toberer, E. S.; Saramat, A.; Kurosaki, K.; Charoenphakdee, A.; Yamanaka, S.; and Snyder, G. J., *Science* **2008**, 321, 554.

[92] Wise, F. W., *Acc. Chem. Res.* **2000**, 33, 773.

[93] Murphy, J. E.; Beard, M. C.; Norman, A. G.; Ahrenkiel, S. P.; Johnson, J. C.; Yu, P.; Mićić, O. I.; Ellingson, R. J.; and Nozik, A. J., *J. Am. Chem. Soc.* **2006**, 128, 3241-3247.

[94] Lu, W.; Fang, J.; Stokes, K. L.; and Lin, J., *J. Am. Chem. Soc.* **2004**, 126, 11798-11799.

[95] Urban, J. J.; Talapin, D. V.; Shevchenko, E. V.; and Murray, C. B., *J. Am. Chem. Soc.* **2006**, 128, 3248-3255.

[96] Wang, D.; Song, C.; Fu, X.; and Hu, Z., *J. Dispersion Sci. Technol.* **2006**, 28, 1197-1200.

[97] Zhang, G.; Lu, X.; Wang, W.; and Li, X., *Chem. Mater.* **2007**, 19, 5207-5209.

[98] Mokari, T.; Zhang, M.; and Yang, P., *J. Am. Chem. Soc.* **2007**, 129, 9864-9865.

[99] Talapin, D. V.; and Murray, C. B., *Science* **2005**, 310, 86-89.

[100] **Chapter D:** Scheele, M.; Oeschler, N.; Veremchuk, I.; Reinsberg, K.-G.; Kreuziger, A.-M.; Kornowski, A.; Broekaert, J.; Klinke, C.; and Weller, H., *ACS Nano* **2010**, 4, 4283-4291.

---

[101] Kim, S.; Fisher, B.; Eisler, H.-J.; and Bawendi, M., *J. Am. Chem. Soc.* **2003**, 125, 11466-11467.

[102] Milliron, D. J.; Hughes, S. M.; Cui, Y.; Manna, L.; Li, J.; Wang, L.-W.; and Alivisatos, A. P., *Nature* **2004**, 430, 190-195.

[103] Brumer, M.; Kigel, A.; Amirav, L.; Sashchiuk, A.; Solomesch, O.; Tessler, N.; and Lifshitz, E., *Adv. Funct. Mater.* **2005**, 15, 1111-1116.

[104] Talapin, D. V.; Yu, H.; Shevchenko, E. V.; Lobo, A.; and Murray, C. B., *J. Phys. Chem. C* **2007**, 111, 14049-14054.

[105] Zhang, J.; Kumbhar, A.; He, J.; Das, N. C.; Yang, K.; Wang, J.-Q.; Wang, H.; Stokes, K. L.; and Fang, J., *J. Am. Chem. Soc.* **2008**, 130, 15203–15209.

[106] Jun, Y.-W.; Lee, J.-H.; Choi, J.-S.; and Cheon, J., *J. Phys. Chem. B* **2005**, *109*, 14795-14806.

[107] Lu, W.; Fang, J.; Ding, Y.; Wang, Z. L. *J. Phys. Chem. B*. **2005**, *109*, 19219-22.

[108] Martin, J.; Nolas, G. S.; Zhang, W.; Chen, L. *Appl. Phys. Lett*. **2007**, *90*, 222112.

[109] Goldstein, A. N.; Echer, C. M.; Alivisatos, A. P. *Science*. **1992**, *256*, 1425-1427.

[110] Rupp, J.; Birringer, R. *Phys. Rev. B* **1987**, 36, 7888-7890.

[111] Zhang, H.; Banfield, J. F. *J. Mater. Chem.*. **1998**, *8*, 2073-2076.

[112] Bai, H. Y.; Luo, J. L.; Jin, D.; Sun, J. R. *J. Appl. Phys.* **1996**, *79*, 361-364.

[113] **Chapter C:** Scheele, M.; Oeschler, N.; Meier, K.; Kornowski, A.; Klinke, C.; and Weller, H. In *Thermoelectric Materials - Growth, Properties, Novel Characterization Methods, and Applications*; Tuller, H. L., Baniecki, J. D., Snyder, G. J., Malen, J. A., Eds.; Mater. Res. Soc. Symp. Proc. 1267, Warrendale, PA, 2010, DD-08-12.

[114] Hou, M.; Azzaoui, M. E.; Pattyn, H.; Verheyden, J.; Koops, G.; Zhang, G. *Phys. Rev. B* **2000**, *62*, 5117.

[115] Hong, L. B.; Ahn, C. C.; Fultz, B. *J. Mater. Res.* **1995**, *10*, 2408.

---

[116] Matsushita, Y.; Wianecki, P.; Sommer, A.; Geballe, T.; Fisher, I. *Phys. Rev. B*. **2006**, *74*, 1-6.

[117] Zyubina, T. S.; Neudachina, V. S.; Yashina, L. V.; Shtanov, V. I. *Surf. Sci*. **2005**, *574*, 52-64.

[118] Yashina, L. V.; Zyubina, T. S.; Pu, R.; Zyubin, A. S.; Shtanov, V. I.; Tikhonov, E. V. *J. Phys. Chem. C*. **2008**, 19995-20006.

[119] Crocker, A. J.; Rogers, L. M. *Br. J. Appl. Phys*. **1967**, *18*, 563-573.

[120] Adachi, J.; Kurosaki, K.; Uno, M.; Yamanaka, S. *J. Alloys Comp*. **2007**, *432*, 7-10.

[121] Vashaee, D.; Shakouri, A., *Phys. Rev. Lett.* **2004**, 92, 106103-4.

[122] Noda, Y.; Masumoto, K.; Ohba, S.; Saito, Y.; Toriumi, K.; Iwata, Y.; Shibuya, I.; *Acta Crystallogr. Sec. C.* **1987**, 43, 1443-1445.

[123] Yang, L.; Wu, J. S.; and Zhang, L. T., *J. Alloys Comp.* **2004**, 364, 83-88.

[124] Kumar, G.S.; Prasad, G.; Pohl, R. O.; *J. Mater. Sci.* **1993**, 28, 4261-4272.

[125] Wei, S.-H.; Zunger, A. *Phys. Rev. B.* **1997**, 55, 13605-13610.

[126] Dalven, R., *Infrared Phys.* **1969**, 9, 141-184.

[127] Zemel, J. N.; Jensen, J. D.; Schoolar, R. B., *Phys. Rev.* **1965**, 140, A330-A343.

[128] Wei, S.-H.; Zunger, A., *Phys. Rev. B.* **1997**, 55, 13605-13610.

[129] Schlueter, M.; Martinez, G.; Cohen, M. L., *Phys. Rev. B* **1975**, 12, 650-658.

[130] Evarestov, R. A.; Veryazov, V. A., *Phys. Stat. Sol. (b)* **1991**, 165, 401-410.

[131] Xu, Y.; Schoonen, M. A. A., *American Mineralogist*, **2000**, 85, 543 – 556.

[132] Keezer, R. C.; Bowman, D. L.; Becker, J. H., *J. Appl. Phys.* **1968**, 39, 2062-2066.

[133] Sykora, M.; Koposov, A. Y.; McGuire, J. A.; Schulze, R. K.; Tretiak, O.; Pietryga, J. M.; Klimov, V. I., *ACS Nano* **2010**, 4, 2021-2034.